UNIVERSITAT POLITÈCNICA DE CATALUNYA
BARCELONATECH

Departamento de Teoría de la Señal y Comunicaciones

UNIVERSITAT POLITECNICA DE CATALUNYA

DEPARTAMENT DE TEORIA DEL SENYAL I COMUNICACIONS

Analysis of Thin-Film Solidly Mounted Resonators for Applications in Harsh Environments

PH. D DISSERTATION

Author: Eduardo Lugo Hernández

Thesis Advisor (s):

Prof. Jordi Mateu Mateu

Dr. Teona Mirea

Barcelona, June 2023

Leaves from the vine,

Falling so slow,

Like fragile, tiny shells,

Drifting in the foam.

Little soldier boy,

Come marching home.

Brave soldier boy,

Comes marching home.

By. Aaron Ehasz

Acta de Examen

List of Terms

ADS	Advanced Design System
AlN	Aluminum Nitride
APM	Acoustic Plate Mode
Au	Gold
AW	Acoustic Wave
BAW	Bulk Acoustic Wave
BeCu	Beryllium Copper
BVD	Butterworth-Van Dyke
CNT	Carbon Nano Tubes
CO_2	Carbon Dioxide
COM	Communication Port
CPU	Central Processing Unit
DUTs	Devices Under Test
EA	Electroacoustic
FBAR	Free-Standing Film Bulk Acoustic Resonators
FOMs	Figures of Merit
GSG	Ground Signal Ground
HV	High Vacuum
IC	Integration Circuits
IDT	Interdigital Transducer
Ir	Iridium
K_{eff}^2	Effective Piezoelectric Coupling Coefficient
KLM	Krimtholz, Leedom and Matthaei

Kt2	Electromechanical Coupling Coefficient
LGS	Langasite
LN2	Liquid Nitrogen
LOD	Limit of Detection
mBVD	Modified Butterworth-Van Dyke
Mo	Molybdenum
QCM	Quartz Crystal Microbalance
Q_p	Parallel Quality Factor
Q_s	Series Quality Factor
RTD	Resistance Temperature Detector
SAW	Surface Acoustic Waves
Si	Silicon
SiO_2	Silicon Oxide
SMA	Sub-Miniature Version A
SMR	Solidly Mounted Resonator
SOLT	Short Open Load Through
TFC	Temperature Coefficient of Frequency
Ti	Titanium
UHV	Ultra High Vacuum
USB	Universal Serial Bus
VNA	Vector Network Analyzer
ZnO	Zinc Oxide

Abstract

The sensing industry is constantly growing due to its demand in fields that require critical and essential information (data environment) for human safeness and quality of life. In recent years, designers, researchers and engineers have paid especial attention in at least three important characteristics in order to obtain reliable devices. These characteristics are: costs reduction, miniaturization for electronic integration compatibility (IC) and sensitivity. A promising technology that has the capacity to meet these requirements is the electroacoustic one. This technology is primary based on the propagation of surface acoustic waves (SAWs) and bulk acoustic waves (BAWs) in a piezoelectric material. For the last years, these devices have been studied and tested in different sensing applications such as gas detectors (gravimetric sensors), temperature monitoring and thin film growth. They have been tested in different fields such as automotive industry, food preservation and thin film deposition, and they have proved excellent performance. Moreover, these applications are special because the collected data occurs in harsh environments. Therefore, the required technology must possess special characteristics to meet these requirements under such environmental conditions. One more time, electroacoustic devices have showed good performance on this type of environments and conditions. BAW devices are an excellent solution to overcome the requirements needed due to their high resolution, straightforward fabrication process, high sensitivity, low costs, low size and compatibility with the IC technology. Specifically, the Solidly Mounted Resonator (SMR) configuration based on AlN is one of the best options since it has been widely studied. This configuration is well-known for its applications in Radio Frequency communication systems. Furthermore, it has demonstrated excellent performance and high quality factors in various sensing applications, even at high temperatures up to 1000°C. Additionally, it has exhibited spurious-free resonances. This characteristic is especially important in sensing applications as the presence of spurious modes can distort the sensor behavior and modify the results i.e., in mass detectors these spurious modes might affect the series frequency resonance, which is directly related with the change of the detected mass. Although this technology has been tested and showed excellent performance at high temperatures, there is a lack of studies in applications at very low or cryogenic temperatures.

In this research work, we present results based on specific designs and simulations, considering the aforementioned requirements, such as temperature and pressure variations, as well as spurious-free resonances. This thesis introduces two significant novelties: the investigation conducted at low temperatures, which remains an essential area of research, on the other side, we include the examination of geometry and topology as potential contributors to the presence of spurious resonances. Additionally, we experimentally validate our models by means

of data extracted from fabricated SMRs, which are based on the c-axis oriented AlN piezoelectric material. In order to carry out our simulations, we have paid careful attention to the well-known one-dimensional Mason's model and Butterworth-Van Dyke (BVD), which are based on the physical properties of materials and equivalent electrical circuit, respectively. We have modified and updated these models to analyze the presence of a new resonator coupled with the main resonance frequency (2.5 GHz). In addition, we have put an enormous attention in the quality factor (Q), frequency resonances and effective electromechanical coupling factor (k_{eff}^2) behavior as a function of temperature. We carried out simulations and compared them with measurements from -160 °C up to 422°C.

List of Figures

List of Tables

Contents

Introduction

Thin Film Bulk Acoustic Wave Resonators (FBARs) are widely used in the telecommunication industry, particularly in Radio Frequency (RF) filters in mobile phones [1]–[4]. This technology has been chosen because of its high performance, small size, low costs and compatibility with the standard Integrated Circuits (IC) technology [5], [6]. During the last decades, BAWs based on thin films have also been studied as gravimetric sensors in chemical and biological applications [7]–[12] substituting quartz crystal microbalances (QCMs). Their ability to detect very small masses (pg and even in fg ranges), places them as promising candidates in monitoring thin films thicknesses, for example; Platinum, Tungsten, Aluminum Oxide and others [13]. This technology has been also used in the environmental industry and medical fields. BAWs are electroacoustic devices based on a thin piezoelectric material, typically Aluminum Nitride (AlN) and Zinc Oxide (ZnO), sandwiched between two electrodes, whose operating frequency lays in the GHz range [14],[15].

In this thesis, we have studied the Solidly Mounted Resonator (SMR) configuration based on BAW-AlN technology. SMRs should have high quality factors (Q) and spurious free resonances. This last requirement is crucial as the presence of spurious resonances can distort their behavior in sensing applications. Previous works have shown that size and shape strongly influence the parallel Q factor [16], [17]. Other studies revealed that the conductivity of the electrodes materials can lead to high ohmic losses and the presence of a spurious mode at series resonance [18]. However, this last effect has been less studied and only considered in Finite Element Modelling (FEM), which consumes long computation time. We found crucial the accurate simulation of this effect with the most typical and practical models i.e., Mason's model [19] and the Butterworth Van Dyke's (BVD) [20], [21] in order to obtain good cost efficient tools in terms of computational requirements. Moreover, we have to take into account temperature as an important input in the resonator models since the series resonance frequency and quality factor are highly sensible to temperature changes. Henceforth, affecting performance of devices based on SMRs such as gravimetric sensors at harsh environments. Developing accurate models help us predict the behavior and design sensing devices with high accuracy and excellent sensibility.

Geometry, configuration, temperature and even the position of the probes used to measure the devices under test (DUTs) (probing spot) are aspects that significantly affect their performance hence sensor's response is affected too. To overcome these drawbacks we have modified Mason's and BVD models and analyzed the influence of these inputs on several designed SMRs. The new updated models have been verified with experimental data based on fabricated AlN-based SMRs with SiO_2/Mo acoustic reflectors operating at 2.5 GHz.

0.1 Objectives of the Thesis

We have mentioned that important output parameters in gravimetric sensors based on BAW-SMRs such as the series resonance frequency (f_s) and quality factor (Q) are affected by the geometry, characterization procedure and temperature. Generally, these effects have been studied by means of the FEM models and at high temperatures. However, exists a lack of studies at cryogenic temperatures using the most practical tools such as BVD and Mason models. Furthermore, few research works have taken into account the procedure of characterization process in their models. In this thesis, we have updated the BVD and Mason models in order to take into account a wide range of temperatures, including the cryogenic ones. Also, we have considered the geometry and characterization process in our designs. Henceforth, we have made an important contribution in the design of SMRs for gravimetric sensors in applications at harsh environments. To this end, the general objective of this thesis is described next. Then, the general objective, will be dived in specific objectives, which are individual aims that we have to carry out sequentially in order to complete the whole general objective.

0.1.1 General Objective

Design, modeling, fabrication and characterization of AlN-SMRs taking into account size (effective area of the resonator), geometry, configuration and temperature (-160 to 422 °C). These resonators must be able to operate at 2.5 GHz. The design of these resonators will be carry out by means of modifying our previous one-dimensional BVD and Mason models and other developed tools available in the research group [74],[78]. Subsequently, resonators will be fabricated and characterized in order to prove the fitting with our modified models. The characterization process will be performed in a specialized vacuum chamber adapted to measure our resonators at extreme temperatures. Finally, an adjustment will be performed in order to improve the performance of the SMRs. The optimization step will be carried out using the scattering parameters (S parameters) of our fabricated resonators as an input in our models.

0.1.2 Particular Objectives

- Extend the existing tools and models for electroacoustic resonators based on BAW technology. These extensions must consider the interrelation between thermal, acoustic and electrical domains. The updated models have to be capable to predict the degradation and detuning of the quality factor and also must be sensible to changes in the resonance frequency.
- Models must consider next designing parameters configuration (BAW-SMR), geometrical parameters (area and shape) and probing spot. Additionally, our models have to

consider the temperature changes since we want to know how extreme temperatures affect the series resonance frequency of the resonators.

- Fabricated several AlN-SMRs with different geometries, sizes, thicknesses and including different materials of the electrodes and acoustic reflector. The fabricated devices will be used to prove the accuracy of our models.
- Establish a good characterization methodology in order to obtain the S parameters. The resonators are going to be measured in a special cryogenic-vacuum chamber, which is a semi homemade system. In this setup, we are able to extract the S parameters from resonators in a wide range of temperatures (-160 up to 130°C). Additionally, we can access another system configuration, where it is possible to extract the S parameters from room temperature up to 422°C.
- Obtain the S parameters from more than one resonator, which means that geometry and size are different. Furthermore, temperature must be changed and divided in equal parts since we want to know how the changes in these designing parameters affect the series resonance frequency and quality factor. Finally, we can perform an optimization and tunning in order to better fit our models. Optimization is possible since S parameters can be used as an input in our one-dimensional models.

0.2 Proposed Methodology

This research project comprises a set of particular objectives, each requiring the implementation of a series of tasks in order to achieve them. In this section, we describe these tasks, meticulously dividing the entire project into a logical and sequential steps. This division of tasks forms our research protocol or methodology, which serves as the guiding framework in order to achieve our general objective.

Task 1. Modeling, designing and fabrication of AlN-SMRs. By means of the available bibliography, tools, models and fabrication methods in the research group. Choose the correct parameters such as thicknesses, size and materials to design our SMRs resonators at an operating frequency of 2.5 GHz.

Task 1.1. Update our available one-dimensional models for BAW-SMRs

We will modify existing models to design our resonators. These models are the one dimensional ones (BVD and Mason). This modification must include the configuration, size of the active area and probing spot.

Extend the models in order to consider the temperature changes as an input. Therefore, we will be able to simulate the temperature changes in a wide range (-160 to 422°C). By doing so, we can observe the most important outputs dependent on the temperature. The important outputs to consider will be the series resonance frequency and the quality factor.

Task 1.2. Design of SMRs for particular applications.

Design of AlN-SMRs able to operate at extreme temperatures (cryogenic and high ones) in order to simulate different applications in different fields such as automotive and space ones. Specify the concrete applications and specifications for our designed resonators. Additionally, we have to consider the next parameters as designing parameters: changes in mass, size of the active area and set-up measurement, since bibliography suggests that it may affect the resonance frequency, hence the whole performance of our devices.

Task 2. Fabrication of devices based on AlN and electrical characterization of our designed resonators at extreme temperatures from -160°C up to 422°C.

Task 2.1. SMR characterization

Define good procedures for the characterization process of the electric response of our SMRs and extract the acoustic parameters in order to define their performance.

Obtain the principal outputs of the resonators in terms of temperature such as series and parallel resonance frequencies, effective piezoelectric coupling coefficient and quality factor. All the mentioned outputs will be computed by means of the scattering parameters.

Task 3. Compare experimental with simulated data and perform an adjustment.

The adjustment will be mainly performed by using the S parameters obtained from our DUTs. The scattering parameters will be used as an input in our modified one-dimensional models and if the model is able to improve we will fit our results tunning the main designing parameters.

Task 4. Report the results of our research project in scientific articles, conferences, posters and symposiums. Finally, we will be able to write down the thesis.

0.3. Contents of the Thesis by Chapter

Chapter 1

In this chapter, we explain how piezoelectricity works and how acoustic waves propagate into a piezoelectric material. We have included the two main types of acoustic modes, which are:

surface and bulk acoustic waves. Subsequently, we introduce electroacoustic devices based on these propagation modes. We additionally describe the most common piezoelectric materials used in such devices, including langasite (LGS) and AlN. The section also describes the characteristics of each configuration and introduces the first attempts for sensors based on BAW-Thin film technology. In the following sections, we introduce the important parameters used to measure the performance in electroacoustic sensors, such as selectivity, resolution, stability, sensitivity, and limit of detection. Afterwards, in the last two sections we briefly review the application fields for both configurations of piezoelectric sensors as gravimetric ones, with particular attention to extreme temperatures. Finally, a comparison is made between SAWs and BAWs characteristics at extreme temperatures to determine which technology is best suited for our investigation project.

Chapter 2

In this chapter we introduce the fundamental theory of acoustical waves and their propagation in piezoelectric and non-piezoelectric materials by means of the one-dimensional acoustical equation of motion. This equation describes how different mechanical fields are related between each other and how waves propagate by means of the particle displacement concept. Once we have derived the one-dimensional equation of motion, we the introduce one of the most used analytical tool, which is the Mason's model (based on the one-dimensional solution) that was introduced by W.P. Mason in the 1930s. This model requires an analysis of how the acoustical equation of motion behaves in different materials in order to obtain the constitutive equations that relate all field magnitudes in the piezoelectric and even for non-piezoelectric materials. Hence, we have a precise model because we are able to add the whole structure films of the resonators with their respective material properties. These tools give us an excellent model for SMRs. On the other hand, as the electroacoustic resonators are also electric devices we have introduced the Butterworth-Van Dyke model, which is a straightforward tool that uses lumped elements. We have analyzed the fundamental theory of both models since we have made use of them in order to model and design our electroacoustic devices.

Chapter 3

We start describing the fabrication process and configuration of our SMRs based on AlN and how their performance is affected by the size of the active area, geometry and probing spot. Then we discuss our proposed modified models that take into account the designing parameters mentioned above. We have observed a new-coupled resonance that affects mainly the series resonance frequency and its quality factor. This new resonance is strongly related to the series resistance due to Ohmic losses in the electrodes. Finally, we have taken this effect into account in our models since the series resonance frequency is an important input parameter in gravimetric sensing applications.

Chapter 4

In this chapter, we provide a comprehensive overview of a semi-automatic probe station measurements system, which is needed to characterize our SMRs, highlighting its operation and capabilities. This system enables the measurement of Devices Under Test (DUTs) at extreme temperatures (-170 to 200°C) and low pressures (10^{-8} Torr). We have emphasized the importance of each module of the system. The whole setup is controlled by means of a Central Processing Unit (CPU). We highlight the inclusion of a temperature control section, which enhances our understanding of temperature changes within the DUTs and improves the accuracy and reliability of our modeling. On the other hand, we outline our methodology used to extract the scattering parameters (S-parameters) at different temperatures. This methodology is subdivided into critical sub-methods in order to facilitate the measurement process. We take into account the significance of the specialized equipment used for cryogenic temperatures such as RF |Z| probe tips.

Chapter 5

Then in chapter 5, we explain the three different studies by means of simulations. These simulations are carried out by our updated models. We perform this device analysis since we want to observe how the series and parallel resonance frequencies (f_s and f_p,), quality factor (Q), effective piezoelectric coupling coefficient and temperature coefficient of frequency (TFC) are affected. The three experiments are divided in three sections, 5.1, 5.2 and 5.3, respectively. These experiments are defined as the effective area and probing spot effects, high temperature and very low temperature analysis, respectively. In addition, we have fabricated three different configurations of SMRs in order to prove the accuracy of our models with respect to designs. For the first experiment, we vary the size of the effective area and the probing spot place in order to monitor the main resonance frequency and also the quality factor. Then in the second and third experiments, we can see how temperature variations affect the output performance of the resonators. These analyses are made since sensors based on SMRs at extreme temperatures are of special interest, especially the gravimetric sensors for high temperatures in harsh environments. We perform a complete analysis in a wide range of temperature from -120°C up to 422°C. Finally, we present results for simulations and extracted data in order to see the correlation between each other.

Chapter 6

In the last chapter we summarize the obtained results, which are a direct consequence of the proposed objectives in this Thesis. We have proved that our updated models have excellent accuracy compared to the fabricated resonators. Thus, we are capable of using our designs in order to make experiments in sensing applications, especially at harsh environments. We have modelled SMRs from -120°C to 422°C, which is a wide gap of temperatures. Henceforth, we

have a wide range of possible applications where we could develop sensing devices. For instance, either gravimetric sensors in the automotive industry at high temperatures or sensors for food preservation at very low temperatures. On the other hand, we have established a methodology to characterize our devices at cryogenic temperatures in our semiautomatic probe tips measurements setup. This Method assure us repeatability since in radio frequency devices characterization is an important drawback to take into account.

Chapter 1

Theoretical Background, SAW and BAW Piezoelectric Devices

In this chapter, we introduce to the reader the theory behind the piezoelectricity phenomena and the propagation of the acoustic waves throughout a piezoelectric material. Starting from this background theory, we have made a summary of the typical classification of piezoelectric devices based on their propagation mode of the acoustic waves. The chapter is divided in different sections. In sections 1.1 and 1.2 we explain how piezoelectricity and how the acoustic waves are generated (Surface Acoustic and Bulk Acoustic Waves) in piezoelectric materials. However, if readers want to investigate more deeply about these topics they can consult references given in these sections. Then in section 1.3 and its subsections, we introduce devices based on SAW and BAW propagation modes. In this section, we also introduce the most common piezoelectric materials used in both technologies such as LGS and AlN for SAW and BAW-FBAR-SMR resonators, respectively. Additionally, we describe the main characteristics of each configuration such as frequency operation, fabrication process and transducer configuration. Afterwards, since our research work is aimed at gravimetric sensor fabrication for harsh environments, starting from subsection 1.3.3 onwards, we introduce the firsts attempts of sensors based on BAW-Thin film technology.

Specifically, in section 1.4, we introduce some of the most important parameters used to measure performance in electroacoustic sensors such as selectivity, resolution, stability, sensitivity and limit of detection. These parameters rely on more designing parameters such as fabrication materials, temperature changes and quality of the piezoelectric. Since all parameters are related, an adjustment process design may be required. Then, in section 1.5 and 1.6 we made a brief review of the application fields for both configurations of piezoelectric devices (SAW and BAW) as gravimetric sensors, putting special attention to applications at extreme temperatures (i.e., -160°C up to 1000°C). Both devices have proven good performances at high temperatures, although at very low ones there is a lack of investigation, especially in modelling. Finally, in section 1.6, we have compared SAWs and BAWs characteristics at extreme temperatures in order to see the advantages of each technologies and choose one that fits with our investigation project requirements.

1.1. Piezoelectric Effects

Piezoelectric materials are capable of converting mechanical energy into electrical energy (direct effect) and vice versa (inverse effect), hence these materials have been used for detection and excitation of acoustic waves. The first effect occurs when the atomic organization of the material is stressed, then this stress causes a mechanical deformation that induces an Electrical Displacement (D), which results in an Electric Field (E) and finally, a Voltage difference across the piezoelectric takes place. In (1.1) we describe this phenomenon mathematically. Then, we have the second effect, which is the inverse effect, when we apply an Electric Field that induces a deformation of the piezoelectric material described by (1.2). We can see both effects in Figure 1.1. a) and b), respectively [22], [23].

$$D_i = d_{ij} T_j \tag{1.1}$$

$$S_j = +d_{ij} E_j \tag{1.2}$$

Where the subscript *i* represents the direction of E and *j* means the mechanical direction.

Both phenomena are related by the piezoelectric coefficient d_{ij}. This variable depends on the direction of the mechanical and electric fields, and both can be positive or negative. The piezoelectric charge constant or piezoelectric coefficient, d_{ij}, is the polarization generated per unit of mechanical stress (T) applied to a piezoelectric material or, alternatively, is the mechanical strain (S) experienced by a piezoelectric material per unit of electric field applied (E). The first subscript indicates the direction of polarization generated in the material when the electric field is zero or, alternatively, is the direction of the applied field strength. The second subscript indicates the direction of the applied stress (T) or the induced strain, respectively. The strain induced in a piezoelectric material by an applied electric field is the product of the electric field value and *d,* which is an important indicator of a material's suitability for strain-dependent. On the other hand, both effects can be applied in different devices such as oscillators, balances and resonators. The most known and studied piezoelectric materials are quartz, $LiNbO_3$ and $LiTaO_3$, as bulk single crystals, $Pb(Zr, Ti)O_3$ (PZT), ZnO or AlN, as thin films [24].

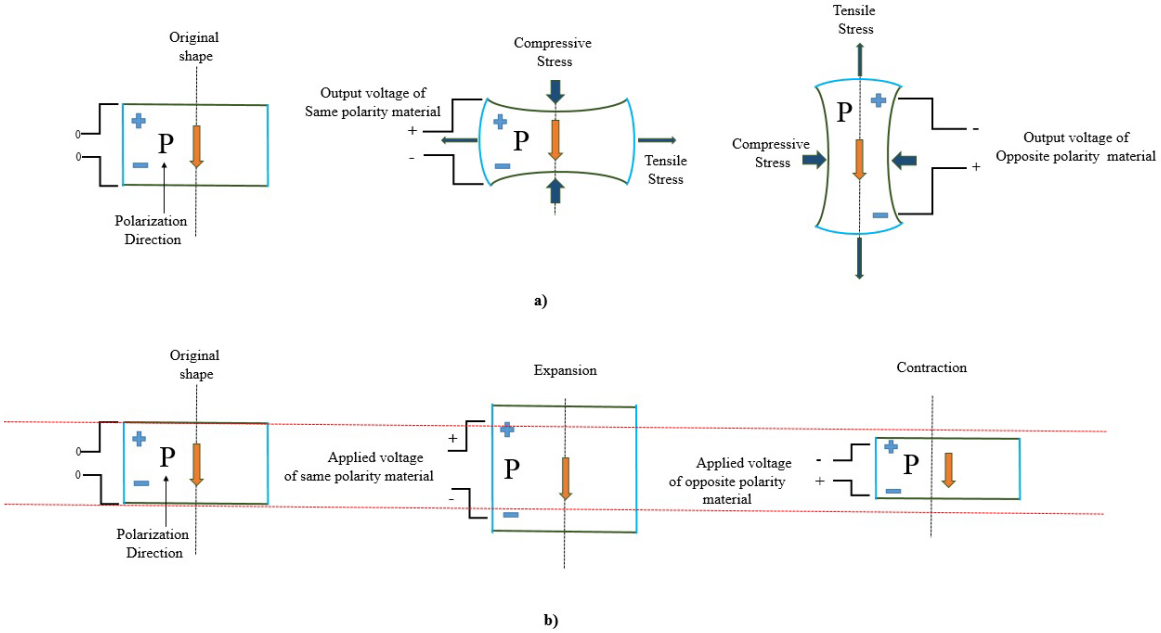

Figure 1.1. Piezoelectric effects, a) Direct piezoelectric and b) inverse piezoelectric effects [22].

1.2. Physics Behind acoustic waves

1.2.1. Bulk acoustic waves

Bulk Acoustic Waves are elastic waves that can propagate through solids and they are categorized mainly in two modes, depending on how they are generated and propagated. The first mode is the longitudinal form (compressional), in which particle displacement is parallel to its propagation direction (See Figure 1.2b). The second one is the transverse form (shear wave), in which particles displacement is perpendicular to the propagation direction (see Figure 1.2a). In order to better understand these concepts, Figure 1.3 shows the particle displacement (polarization) associated with transverse and longitudinal waves, a) and b) respectively. Here lambda (λ) is the wavelength.

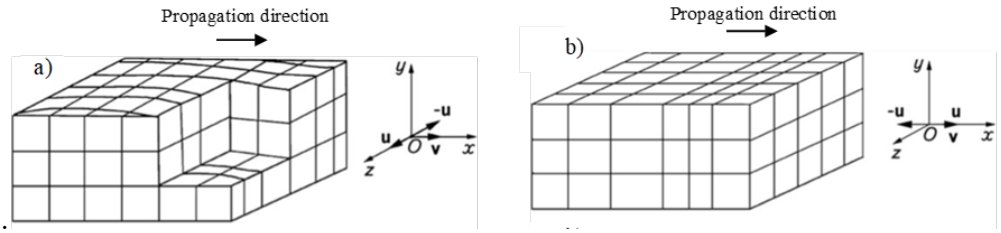

Figure 1. 2. a) BAW-Transverse wave and b) BAW-Longitudinal wave. The particle displacement is perpendicular and parallel to the propagation direction, respectively [25].

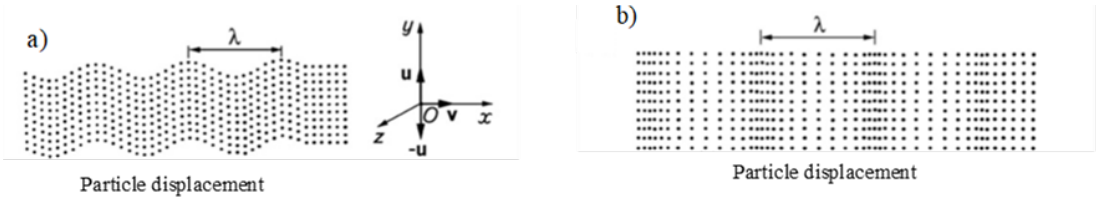

Figure 1. 3. Particle displacement associated with a) transverse and b) longitudinal waves [25].

The propagation of these waves is not the same for each case because it depends on their phase velocity, which is different in each case even if the media of propagation is an isotropic media. The phase velocity (V) for an isotropic material depends on the stiffness constant (C_{ij}) and the mass density (ρ). If we consider the simplest case that corresponds to an isotropic media, we will have only three cases of the stiffness constant since this variable is more complex and extensive. These three cases are: first when we apply stress on the Z direction and its strain occurs only in this axis (C_{11}) (longitudinal wave); the second when we apply stress in the same direction (Z) and the strain occurs in the X and Y direction (C_{12}) (Shear wave); in the third case we have the constant C_{44} describing the relationship between perpendicular (shear, X and Y-direction) stress and strain. Taking into account the statements above, we can define the longitudinal and transverse phase velocities as follows.

$$V_l = \sqrt{\frac{C_{11}}{\rho}} \tag{1.3}$$

$$V_t = \sqrt{\frac{C_{44}}{\rho}} \tag{1.4}$$

Where C_{11} and C_{44} are the stiffness constant for the longitudinal and transverse waves, respectively, and rho (ρ) is the mass density.

In addition, it is important to mention that for the longitudinal wave the volume of the material changes with propagation whereas for the shear mode it does not.

1.2.2. Attenuation Mechanisms of Bulk Acoustic Waves.

As the waves propagate in a media the attenuation occurs in different forms. Some of these mechanisms are explained below.

1. Scattering loss due to inhomogeneity: it is mostly temperature independent and is dependent upon the material preparation. This mechanism is dominant for most polycrystalline materials.

2. Scattering loss of coherent waves due to thermal lattice vibration: it exists even in ideal perfect crystals and increases with temperature.

3. Energy transportation by thermal diffusion to neutralize temperature variation caused by the volume change: since shear waves do not associate volume change with propagation, this mechanism occurs only in longitudinal waves.

It is important to mention that these attenuation mechanisms are significant when the wavelength is comparable to the scatters. Then, materials with high velocities are a better option to reduce losses in elastic waves propagation.

1.3. Surface and Bulk Acoustic Wave Devices

Electroacoustic devices based on the propagation modes of the acoustic waves (SAWs, BAWs and Acoustic Plate Mode) are the main studied structures in electroacoustic devices. As mentioned above, these devices receive their names accordingly to the type of their acoustic waves and propagation modes in a piezoelectric material. In SAW devices, the waves propagate along the surface of the piezoelectric material, which is orthogonal to its displacement. On the other hand, in BAW devices, the acoustic waves propagate through the volume, or through the bulk of the piezoelectric material, which is parallel to the displacement [23]. Finally, Acoustic plate mode (APM) devices [26]–[29], are based on waves that travel between membranes or plates and their thicknesses are comparable to their wavelength λ. These devices can be considered as BAW and SAW devices since the waves are confined between the plates in multiple reflections through the entire volumes of the device and although most of the waves are generated using the principle of SAWs.

1.3.1. Electro Acoustic Devices based on SAWs

Resonators based on SAWs have been studied since the 1970s. They have been initially used as elements to stabilize oscillators. By these years, these devices were capable to operate at higher frequencies than BAWs devices; however, their oscillator stability was not so high. On the other hand, in the 80s these devices were studied for applications such as mobile telephones band pass filters, delay lines, resonators, oscillators and matched filters due to their low insertion losses. These devices are in a widely range of RF practical systems, such as communications systems radar and also are in consumer applications, such as mobile phones and television [30]. SAW devices are composed of a piezoelectric film and a sequence of metal electrodes (strips) placed on the surface of the piezoelectric with an interleaved alternating pattern, known as Interdigital Transducer (IDT). Figure 1.4 shows the basic SAW device using two transducers, one of them for generation and one for reception of the acoustic waves. There are two main configurations of these devices, which are two port delay lines or one or two-port resonators (see Figure 1.5a and b, respectively).

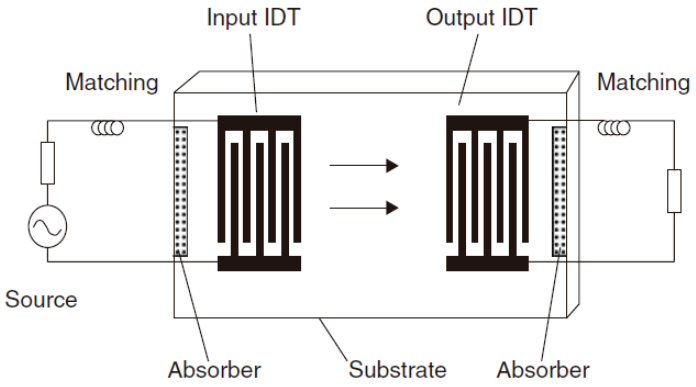

Figure 1. 4. Scheme of a basic surface acoustic device [30].

The typical operating frequencies of these devices goes from several MHz range up to some GHz. The electrode width is determined by the fabrication technology and is typically a quarter of the center-frequency wavelength. The minimum width for commercial devices is approximately 0.5μm, limiting the achievable frequency up to 1.5 GHz for a typical velocity of 3000 m/s, but this can be extended up to 5 GHz by means of special fabrication techniques. When the operating frequency is near to some MHz the size of the resonators become an inconvenient since new technologies are focused on miniaturization.

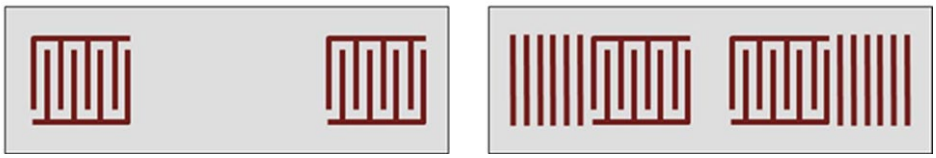

(a) (b)

Figure 1. 5. SAW resonator configurations (a) delay line (b) resonator (two-port) [31].

1.3.2. Electro Acoustic Devices Based on BAWs

The basic configuration of these devices is a composition of two electrodes with a piezoelectric film in between. Typical piezoelectric materials are quartz, Aluminum Nitride (AlN), Zinc Oxide (ZnO), or Lithium Niobate. To operate them an alternate signal is applied to the electrodes and bulk acoustic waves can be generated and propagate through the entire volume of the piezoelectric film. As explained above, there are two basic forms of propagation of these waves: the transversal (shear) and the longitudinal (compressional) forms. The frequency of operation of these resonators is directly related with the thickness of the piezoelectric material given by (1.5).

$$\omega_n = (n+1)\cdot\frac{\pi}{2}\cdot\frac{v}{d}; \qquad n = 0,1,2,... \tag{1.5}$$

Where v is the acoustic velocity of propagation and d is the thickness of the piezoelectric.

The first BAW resonators were used to implement Quartz Crystal Microbalances (QCM), which used AT-cut quartz crystal as a piezoelectric material. However, these devices have a problem related to their frequency of operation, which is typically limited below few hundreds of MHz (main mode) [32], [33]. This problem is directly connected with the physical limitations of the crystal thickness. A typical QCM is shown in Figure 1.6. In the next subsection, we are going to talk about sensors based on these devices.

1.3.2.1. Quartz Crystal Microbalances

In 1959, Günter Sauerbrey published the results of his investigation with quartz crystals. These results concluded with the creation of the first acoustic transducer for gravimetric sensing called QCM [34]. QCMs are capable to measure small masses such as nano and even pico-grams (10^{-9} and 10^{-12}, respectively) [35], [36]. Finally, quartz microbalances can also operate in liquid and gaseous environments [37]–[39].

QCMs are fabricated using a quartz-piezoelectric film with typical thicknesses from 10 up to 200 μm. These films are sandwiched by two metallic electrodes allowing the device to operate at few MHz [40]–[42]. QCMs are referred to as thickness shear mode resonators since they consist of a thin AT-cut quartz material having symmetrically patterned circular electrodes on both sides (see Figure 1.6). That means a shear deformation occurs when a voltage is applied making them highly sensitive to any surface perturbations [43]. Also, due to this nature of propagation (shear mode), they are a good option for liquid environments without much damping losses.

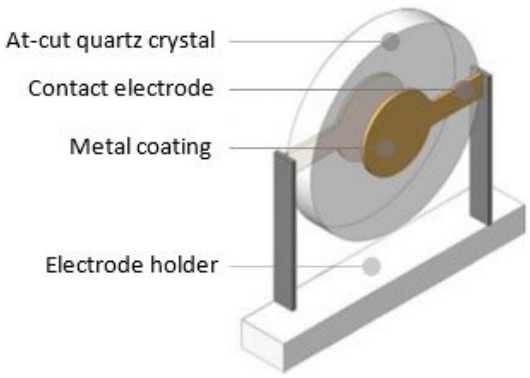

Figure 1. 6. Basic schematic of QCM sensor consisting of a piezoelectric AT-cut quartz crystal coated with two metallic electrodes, one on each side [44].

1.3.2.2. Thin Film Resonators, FBAR and SMR Configurations

Recent applications of electroacoustic devices require new characteristics such as high frequency of operation, typically several GHz, miniaturization, low power consumption and monolithic integration circuits (IC). The use of a bulk single crystalline piezoelectric such as quartz cannot accomplish these requirements since this technology would require the thinning of their thicknesses. Although a technique to carry out this requirement exists nowadays (plate thinning), there is not industrialized on a large scale yet. On the other hand, SAW devices have an important problem, which is the electro-migration phenomena of the submicron strips due to the high temperatures reached at medium and high operation powers [45], [46]. Further, in this technology velocities of the acoustic waves in the substrates are low (3000 m/s). Film bulk acoustic devices (FBAR) were possible thanks to the novel fabrication techniques in the microelectronic industry. The sputtering technique and lithography with high-resolution patterns, made possible a new technology based on BAWs-Thin films [47]–[49]. Thin film resonators were presented by Lakin and Wang in the early eighties [50] and also by Grudkowski and Nakamura [51], [52]. The first devices were fabricated by means of ZnO, However, nowadays ZnO is not the best option due to its inherent problems such as increased losses in the GHz operating range, chemical instabilities, and low performance.

BAWs based on thin films are fabricated with a thin piezoelectric layer (<3 μm) sandwiched by two metallic electrodes, which are usually ten times thinner than the piezoelectric thickness. Depending on the acoustic wave isolation inside the piezoelectric layer, there exist two main structures, which are called free-standing film bulk acoustic resonators FBAR (see Figure 1.7a) and Solidly Mounted Resonators (SMRs) in Figure 1.7b. SMRs isolate the acoustic waves inside the piezoelectric material by placing it onto an acoustic reflector, while suspended FBARs use an electrode-air interface.

Thin Films resonators have been extensively researched; hence they have become a widely used configuration in various fields such as wireless communications, automotive industry as gas detectors, medical and food industry. In particular, they have been used in wireless communication systems, such as smart phones, tablets and high-quality factor filters, where they are used to separate different frequency bands. On the other hand, thin film resonators have been modelled, designed, fabricated and tested at extreme conditions such as low pressures and extreme temperatures and they have shown good performance. In sections 1.5 and 1.6, we are going to describe such applications. Additionally, in sub-sections 1.3.2.3 and 1.3.2.4 we are going to introduce and describe two important components of SMRs, which are: the acoustic reflector and the piezoelectric material (C-axis oriented AlN).

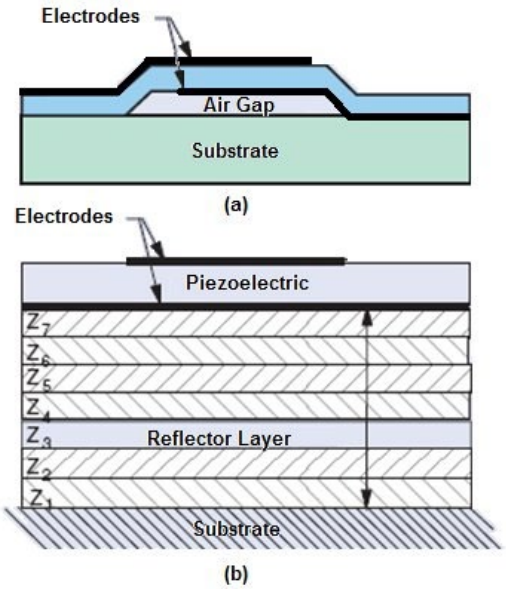

Figure 1. 7. Cross section of basic BAWs based on thin films configurations, FBAR (a) and SMR (b) [53].

1.3.2.3 Acoustic Reflector in SMRs

The acoustic reflector consists in one stack of alternating high and low acoustic impedance layers of a quarter wavelength of thickness (λ/4). Sometimes this structure is called Bragg reflector due to its similarity to the optical Bragg mirrors, however, in the case of acoustic Bragg reflectors the impedance substitutes the refractive index. The acoustic reflector is sandwiched by the substrate and the bottom electrode in BAW-Thin Films resonators. The acoustic mirror reflects the acoustic waves back into the piezoelectric material, which increases the energy stored in the resonator per cycle of vibration. Normally, acoustic resonators are fabricated in the quarter-wavelength configuration, which means that each film of the reflector has a thickness of a quarter of the wavelength of the main mode of resonance (frequency operation). The acoustic wave is reflected back into the piezoelectric material with a phase shift of 180 degrees, which results in constructive interference and increased energy stored in the resonator.

1.3.2.4 C-axis Oriented Aluminum Nitride Piezoelectric Films.

C-axis aluminum nitride is a versatile and popular piezoelectric material that is used in a wide range of electronic devices, particularly SAWs and BAWs. This is due to its excellent electroacoustic properties as well as its high thermal conductivity, which is around 280 W/mK, and low thermal expansion coefficient (α) 4.15 10^{-6} 1/K. In SAWs, c-axis AlN is used both as the substrate and the piezoelectric material. The high piezoelectric coefficient 3.4 pm/V (d) allows the efficient conversion between electrical energy to mechanical one and vice versa, making it an

excellent material for SAW applications. Additionally, the high longitudinal acoustic wave velocity (~11,300 m/s) and low acoustic losses make it suitable for high frequency SAW resonators. On the other hand, in BAW devices, c-axis AlN is typically used as the piezoelectric material due to its high effective piezoelectric coupling coefficient (~6.5) and its high mechanical quality factor (1500 up to 2000). In the case of its thermal properties, such as high thermal conductivity and low coefficient of thermal expansion, it makes it suitable for high temperature applications. C-axis AlN thermal conductivity is significantly higher than other commonly used piezoelectric materials such Zinc Oxide and Lithium Niobate, which have 60 W/mK and 35 W/mK respectively. This high thermal conductivity of AlN also helps to dissipate the heat generated during device operation and maintain stable its performance at high temperatures. In addition, the low thermal expansion coefficient of c-axis AlN also reduces the risk of thermal stress that could induce failure in the device operation, particularly those operating in high temperatures. Further, c-axis AlN thin films have been deposited onto different substrates [54] in a wide process window of techniques showing its versatility and making it an excellent option to grow thin film electroacoustic devices. Summarizing, the combination of its excellent acoustic, electrical, and thermal properties make c-axis AlN an excellent material for a wide range of electronic applications, particularly in high temperature environments, which is necessary in this research project since our resonators have to operate at extreme temperatures. The material properties of AlN were taken from several sources, which can be consulted for further research in [55]–[60].

1.3.3. Sensors Based on Thin Film Resonators

Thin film devices can be designed to operate at higher frequencies than QCMs, typically in the range of a few hundred of MHz up to few GHz (10^6 to 10^9). Sensors based on thin films technology have reported better sensitivity in gravimetric applications. This means they can register small quantities of mass such as pico and even femto-grams (10^{-12} to 10^{-15}). The sensitivity in SMR sensors can be affected by different factors such as thickness and quality of the piezoelectric film, the resonant frequency, and even the measurement setup. There are more parameters that will define a good performance such as quality factor, temperature stability and fabrication process. The quality factor is typically in the range of a few hundred to a few thousand (10^2 up to 10^3), which indicates good energy storage and low energy dissipation. On the other hand, the temperature stability shown is suitable for these configuration of sensors. Henceforth, their temperature stability makes them a good option for use at extreme temperatures. Finally, thin film sensors can be integrated with electronic systems (IC) due to their small sizes and simple operation principle and also they can be fabricated using standard microfabrication techniques, which allows for high-volume and low-cost production.

FBAR sensors have shown potential for use in various applications: gravimetric sensors such gas detectors, bio-sensing (organic molecule detectors), and wireless communications. Figure 1.8, we can see an FBAR sensor designed to detect formaldehyde chemical substance, which is an indoor air contaminant. This sensor is capable to operate up to 4.5 GHz. Its sensitive coating (single-wall carbon nanotubes) is capable of detecting ultra-small mass changes induced by the absorption of formaldehyde molecules [61]. In section 1.4 and its subsections, we are introducing the most important parameters of sensing devices such as sensitivity, selectivity, surface coating and resolution since they are important in the design process of sensors based on the thin film technology.

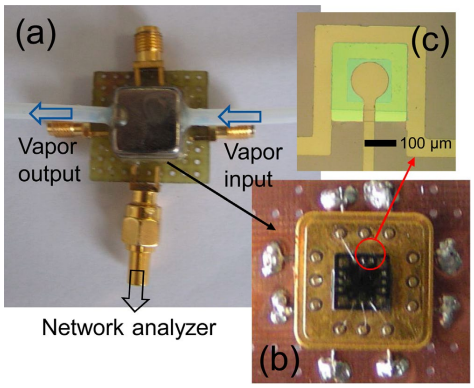

Figure 1. 8.(a) Image of a packaged BAW-Thin film sensor designed for sensing of formaldehyde, (b) device integrated with PCB, (c) magnified image of sensor element[61].

1.4. Performance Parameters of Electroacoustic Sensors

Generally, all kind of sensors have to accomplish certain requirements, or the widely-called figures of merit (FOM), to be considered as good devices with high performance. The most common ones are: sensitivity, selectivity, limit of detection (*LOD*), stability, speed of response and resolution. Nevertheless, those variables are not enough for the case of the electroacoustic sensors to define their performance. Therefore, we have to take into account a couple more variables such as the quality factor and the effective piezoelectric coupling coefficient (k_{eff}^2). The quality factor Q, which quantifies losses of the resonator, can be defined as the ratio between the stored energy in the oscillating resonator and the energy dissipated per cycle by damping processes. k_{eff}^2 indicates how efficiently the electrical energy is transformed into mechanical energy, but considering the complete device configuration.

1.4.1. Sensitivity

The sensitivity quantifies how sensors respond (magnitude of the response) to changes of the input value, which is the target compound that could be mass, temperature, pressure or viscosity. For FBAR-SMRs the sensitivity can be defined as follows: the ratio of the change in resonance frequency of the resonator ($\Delta f/f_0$) to the change in the physical magnitude being measured ($\Delta compound$). We can compute the sensitivity by means of (1.6).

$$Sensitivity = \frac{\Delta f / f_0}{\Delta compound} \tag{1.6}$$

1.4.1.1. Important Considerations in Sensitivity

The most important parameters that certainly can affect the sensitivity of the thin film sensor are: resonance frequency, temperature stability, quality factor and the mass loading effect. First, the sensitivity is directly proportional to its resonance frequency (see equation 1.6). At higher resonance frequencies we can achieve higher sensitivities. The quality factor is defined as the ratio of its resonance frequency to its bandwidth. Higher quality factors correspond to higher sensitivities. A definition of the quality factor of the resonators will be described in the Butterwoth –Van Dyke section. The sensitivity can also be affected by changes in temperature. Therefore, resonators with high temperature stability are desirable for applications that involve temperature variations.

Equation (1.6) assumes that resonators will be operated in the linear zone, and that the change in resonance frequency is directly proportional to the change in the target compound being measured. In practice, the sensitivity can be affected by non-linearities and other factors, such as noise and drift. Therefore, careful calibration and characterization of the sensor is necessary to ensure accurate and reliable measurements. Overall, a combination of high resonance frequency, high quality factor, low mass loading, high effective piezoelectric coupling coefficient, and high temperature stability is desirable for achieving high sensitivity.

1.4.1.2. Mass Loading Effect

The mass loading effect in BAW-Thin film resonators refers to the change in resonance frequency due to the addition of mass to its surface such as passivation layers, coating material and temperature compensation layers. When a mass is added to the surface, then the total mass of the resonator changes the distribution of the acoustic energy, resulting in a change in the resonance frequency. In some materials the sensitivity of a BAW sensor is inversely proportional to the mass loading effect.

1.4.1.3. Piezoelectric Coupling Coefficient

The piezoelectric coupling coefficient is a measure of the efficiency with which mechanical energy is converted into electrical energy and viceversa. In section 2.3.4 we define the effective piezoelectric coupling coefficient, which is necessary to understand how the mechanical energy is converted into electrical one in resonators and how this important parameter tell us if our designs are well done.

1.4.2. Selectivity

The selectivity in a sensor is the ability to detect only the target material. Sensors must avoid other compounds or species minimizing the interference in the sample. Some important parameters influencing the selectivity in FBAR sensors are the following:

1. Coating material
2. Receptor specificity
3. Signal processing

1.4.2.1. Coating Material

The coating material on the surface of the sensors is crucial for selectivity. This coating material must be designed to selectively choose the target compound while minimizing non-specific binding to other compounds in the sample. It should also be stable and not interfere with the mechanical properties of the resonator, one example of this coating material used in FBAR-SMR sensors are carbon nanotubes (CNT), which are design to trap specific compounds.

1.4.2.2. Receptor Specificity

The receptor material used on the surface sensor should exhibit high specificity for the target compound. As such, it must be designed to recognize only the specific target compound with high affinity and selectivity. Additionally, the coating material should not react with other compounds or non-specific targets present in the media.

1.4.2.3. Signal Processing

Advanced signal processing techniques can be used to improve the selectivity. For instance, spectral analysis of the sensor output can help to distinguish the signals from the target and interfering species, enabling the rejection of interfering signals.

1.4.3. Resolution

This parameter indicates the minimum value detectable of the target compound in the functionalized surface (i.e., mass increments or decrements) and has to be distinguished from other parameters such as noise and other species through the frequency shift (Δf). In general, a combination of low noise level, high sensitivity, wide dynamic range, good stability, and linearity is desirable for reaching high resolution.

The dynamic range is the span of values of the physical parameter (target compound) that can be measured with sufficient accuracy and precision. A wide dynamic range is necessary to achieve high resolution values.

1.4.4. Stability

Stability is a crucial parameter in sensors since it determines the ability to maintain consistent and reliable measurements over the time. Stability can be influenced by environmental factors such as temperature, humidity, and pressure, as well as aging effects and mechanical stress. Ensuring stability involves designing resonators with robust materials such as AlN, considering the environmental and operational conditions, and performing regular calibration and testing.

1.4.5. Limit of Detection

The limit of detection (LOD) indicates the minimum amount or concentration of a target compound that can be detected with a reasonable level of accuracy and precision. The LOD is an important performance parameter for sensors because it determines the sensitivity and the lower limit of detection for a particular application. LOD depends on various factors, such as quality factor of the resonator or resonant frequency. The range of LOD in FBAR-SMRs go from parts per billion (ppb) up to parts per trillion (ppt). For example, thin film sensors have been reported to detect gas concentrations in the ppb range for various gases such as methane, hydrogen, and carbon monoxide. The LOD may also be affected by interfering species, temperature, pressure, and humidity, among other factors. Therefore, careful calibration and validation are essential to accurately determine the LOD for a particular application.

1.4.6. Frequencies of Operation

Although FBAR-SMR and QCM sensors have the same working mechanism, their frequencies of operation (resonance frequency) are different. FBARs and SMRs normally work from several MHz up to 10 GHz [62]. There are two factors that drive high resonance frequencies in such devices, which are thickness and nature of piezoelectric material. First, the thicknesses used are

in the range of sub-µm up to few µm, leading to a small mass quantity of the piezoelectric material that yields high resonance frequency, which yields high sensitivity. In addition to sensitivity, the frequency of operation also affects other important parameters such as resolution and stability. Higher resonant frequencies lead to higher resolutions in BAWs based on thin films technology.

1.5. Performance of Sensors in Different Environments

There is a wide classification of sensors. Such classification depends on what type of data the sensors are collecting (input). This classification is mainly composed of three big fields: biological, chemical and physical ones. For the biological one, we can find sensors that could detect proteins, viruses, bacteria and more biological agents. In the case of the chemical industry, we can find devices sensing variables such as vapor gases (i.e. CO_2 and O_2), molecules in liquid solutions and several chemical species or compounds. Finally, for the physical field, there are sensors capable to collect data from inputs like mass, temperature, pressure and density. The whole collection of inputs or target compounds are collected and measured in a different media, which can be a liquid and gaseous environment. In Figure 1.9, we see an example of a biological sensor based on an electroacoustic device. As mentioned, there are different media where sensors could be utilized; unfortunately not all of these environments are friendly with the sensor devices, specifically for those sensors that their performance is affected by the environment, i.e., a corrosive media could affect the physical properties of the sensor's materials such as density, permittivity and Young's module, changing their performance and reliability. In this research project, we have focused our efforts on designing SMRs capable to operate at extreme temperatures (-160°C up to 422) in harsh environments. These devices have to be able to detect those changes in the inputs, such as temperature changes, and maintain the response reliable.

In Section 1.6, we will present the state of the art for the two main technologies regularly used to develop electroacoustic sensors in harsh environments: SAWs and BAWs, these last based on thin-film configuration. Based on their advantages and drawbacks, we will be able to choose the most suitable technology and configuration to design and develop our resonators.

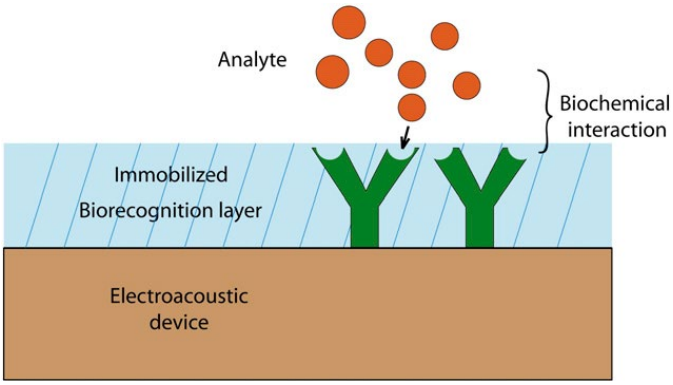

Figure 1. 9. Schematic of a surface sensitive electro-acoustic biosensor, having an immobilized biological recognition layer as the selective sensing layer [63].

1.6. Sensors Based on SAW and BAW at extreme temperatures

As outlined in section 1.5, sensors can be affected by different conditions in the media such as, temperature, pressure and other physical inputs. Most of the research works related to design electroacoustic sensors have been focused at high temperature environments and they have showed good performance. On the other hand, investigations at very low temperatures (i.e., aerospace technologies) and theoretical models are still missing. The investigation of sensors based on SAWs and SMRs at extreme temperatures have been carried out by many research groups and have proven that these technologies are capable to operate in a wide range of temperatures from -200 °C up to 1100°C [58], [64]–[72]. However, parameters such sensitivity and stability can be affected by temperature changes, and the temperature range over which they can provide accurate measurements may be more limited because of materials, design and their configuration. Typically, SAW sensors developed to operate at high temperatures have been based on langasite (LGS). This piezoelectric material is one of the most stable ones at such temperatures without compromising its performance. Additionally, in recent investigations, several research groups have fabricated sensors at high temperatures by means of AlN piezoelectric on sapphire substrates showing improvements in the range of temperature and frequency operations. SAW technology uses IDTs to transform acoustic energy to electrical one. Piezoelectric and IDT material have to be chosen carefully to ensure good performance at such temperatures. In the case of SMRs, the last investigations at extreme temperatures have focused their efforts on AlN due to its intrinsic properties such as excellent stability at high temperatures without losing its piezoelectric property. AlN is also capable of operating with high power signals due the thermal stability.

1.6.1. SMR Configuration in Sensors at Extreme Temperature Applications

SAW devices are a well-studied technology and have a straightforward fabrication process since they need only a few photolithographic steps. SAW sensors can be integrated with other electronic components on a single chip (based on Silicon technology), which can reduce the overall size and complexity of the system. Additionally, there are a great tool for wireless interrogation mainly in the configuration of delay lines. On the other hand, one serious drawback at high temperatures in SAW devices occurs in the IDTs. When they are exposed for long periods of time to such temperatures, a phenomena called destructive agglomeration occurs. This effect refers to the fact that the surface of the resonator becomes altered, even damaged, leading to a degradation of its performance. This occur when temperature exceeds a certain threshold and the material properties, such as thermal expansion coefficient and the mechanical properties, can change, leading to thermal stresses and strains that can cause deformation, cracking, or even melting of the surface. This can also lead to the formation of unwanted metal particles or agglomerates on the surface, which can affect the resonance frequency, the sensitivity and stability. One way to mitigate this effect is to use materials with low thermal expansion coefficients and high thermal conductivity such as AlN. This can help to minimize the stresses and strains that arise from thermal cycling and prevent damage to the device. Although SAW devices have been tested at higher temperatures than FBAR-SMRs, the destructive agglomeration effect in thin film resonators can be overcome by making the electrodes thicker at expenses of making thinner the piezoelectric in order to keep the resonance frequency stable. Therefore, SMRs, can handle high power and high operating frequencies, which is translated to size reduction, low cost production and their electrodes allow more flexibility in terms of thickness and materials. Therefore, SMRs may be a more suitable technology for applications that require several GHz of their frequency operation (resonance frequency). This configuration is also capable to operate at extreme conditions such as cryogenic temperatures.

1.7. Summary

In this chapter we have provided an overview of piezoelectricity, including the nature of acoustic waves in such piezoelectric materials. Then, we have described the most common electroacoustic devices and their main two configurations (SAW and BAW resonators), as well as the most common piezoelectric materials used in both technologies. Secondly, we have made a brief review of sensors based on these technologies, especially those based on BAW-Thin Films. Afterwards, we introduce the most important parameters that measure a good performance in

electroacoustic sensors such as sensitivity, resolution and selectivity. Then a review of the application fields for both configurations of piezoelectric sensors is explained and we have focused on gravimetric sensors at extreme temperatures. Finally, we pounded SAWs and BAWs characteristics at extreme conditions to identify the advantages and drawbacks of both technologies in order to determine the best configuration and material options for our aims in this research project.

Chapter 2

One-Dimensional and Electrical Models Derivation for Thin Film Bulk Acoustic Wave Resonators

The objective of this chapter is to conduct to the reader a comprehensive analysis of the mathematical and physics principles governing the propagation of acoustic waves in non-piezoelectric materials. By extending this analysis to include piezoelectric materials, we can better understand the behavior of devices composed of both material. This analysis serves as a beginning for introducing the one-dimensional and electrical models: BVD and Mason models, respectively. By utilizing these models, we can effectively design and adjust measurements from electro-acoustical devices using both non-piezoelectric and piezoelectric materials.

This chapter introduces the fundamental theory of the acoustical wave's propagation in non-piezoelectric and piezoelectric materials. In the case of piezoelectric films, we consider infinite lateral dimensions, which means that only waves propagating in the thickness direction are considered. The solution of this problem will be carry out from the one-dimensional point of view. Henceforth, we will obtained the general solution of the one-dimensional acoustical/mechanical equation of motion. Afterwards, in sub-sections 2.1.1 and 2.1.2, we will obtain the solution for a non-piezoelectric and piezoelectric materials. With these solutions, we will be able to understand how an acoustical wave propagates in both types of materials.

Afterwards, in sections 2.2 and 2.3, we introduce the fundamental theory of the most used one-dimensional tools for electroacoustic devices. First, the Mason's model, which was introduced by W.P. Mason in the 1930s [73]. On the other side, as the electroacoustic resonators are also electric devices, we will also use the Butterworth-Van Dyke (BVD) model, which is a straightforward tool that has been used since the 1920s. BVD considers an equivalent electric circuit based on lumped elements. We have included both models in this chapter since we consider them excellent tools for the designing and modelling of electroacoustic devices based on the thin film technology. In the Mason's model case, we have analyzed how the acoustical equation of motion behaves in a piezoelectric slab in order to obtain the constitutive equations that relate the acoustical and electrical fields, although the thermal field also can be included [74]. Furthermore, we have derived the equivalent circuit based on the T-transmission line model, which is capable of

modelling the whole resonator structure, (coating material, piezoelectric, electrodes, acoustic reflector and substrate). By means of both models, we are capable of modelling SMRs for application in harsh environments. These resonators typically are composed of thin piezoelectric film sandwiched by two metallic electrodes onto an acoustic reflector. Then, we show that the BVD model is a straightforward tool that is going to help us to compute the equivalent electric circuit in order to observe the behavior of designed resonators. Finally, we strongly recommend to the reader consulting the bibliography listed in [75]-[79] for a more comprehensive explanation and deductions of the theory mentioned in this chapter.

2.1. The Equation of Motion, the One-dimensional Analysis

Isaac Newton derived one the most important set of equations in the seventh century, this set of equations are called the Newton's Laws of Motion, which define how different forces act upon a physical body. To define the acoustical equation of motion we must focus on the second law defined by (2.1). This equation defines that when a force is applied to a rigid body, this suffers an acceleration which is proportional to the mass of the body. This assumption must be considered true for rigid bodies.

$$dF = m \cdot a \tag{2.1}$$

On the other hand, when we take into account the elasticity (a physical property of bodies) their behavior will be different since the internal forces affect the internal atomic structures causing stress (T) and strain (S). One important consideration of these two forces is that the stress does not cause strain and vice versa. However, stress and strain are conditioned upon each other's existence. This statement means that the presence of stress indicates that strain must exist and vice versa. According to equation (2.2), T measures the stress caused in the internal structure by external forces divided by the cross-sectional area over which these forces act. In Figure 2.1, we can observe a hypothetical isotropic volume that helps us to understand the stress concept. Here T_1 and T_2 are both components of T and both have a position respect to the vector of the area ($\vec{A}$), which tell us its orientation and is perpendicular to the surface area. The case when T is longitudinal occurs when its component (T_2) is parallel to the vector ($\vec{A}$). On the other side, for the shear component (T_1), its direction must be transversal to ($\vec{A}$). Normally, T comes in pairs but in opposite directions ($-T_1$ and T_1), but is important to know that they are not always equal. For example, in the isotropic volume considered in Figure 2.1, there is a stress T_1 and leads an opposite traction stress $-T_1$.

$$dF = dA \cdot T \tag{2.2}$$

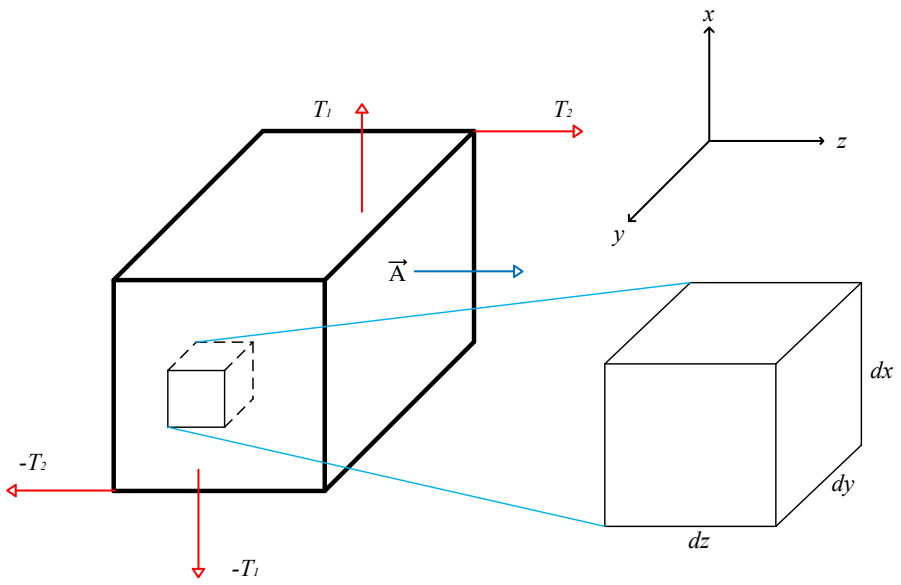

Figure 2. 1. Orientation of traction forces (T_1 and T_2) and the area orientation vector of the transverse area ($\vec{A}$) of an isotropic volume. The close up view, corresponds to an infinitesimal part of the rigid isotropic volume.

Furthermore, A is defined as the cross-sectional area of the rigid body. Each component of T generates a mode of propagation of a mechanical wave, so we will derive this equation taking into account some considerations and Figure 2.1. First of all, we have to recall the Newton's second law and analyze it deeply. We take a small slab volume of the rigid body, which is defined as dx, dx and dz, so the cross-sectional area is defined as follows

$$A = dx \cdot dy \tag{2.3}$$

Then we assume that T_1 and $-T_1$ are not equal, this results in a force in the small volume which can be written as

$$dF = \left|-T_1 - T_1\right| \cdot dA = \frac{\partial T}{\partial z} \cdot dz \cdot dA \tag{2.4}$$

Now rewriting the Newton's second law

$$\frac{\partial T}{\partial z} \cdot dz \cdot dA = \rho \cdot A \cdot \Delta z \frac{\partial^2 u}{\partial t} \tag{2.5}$$

Resulting in

$$\frac{\partial T}{\partial z} = \rho \cdot \frac{\partial^2 u}{\partial t} \tag{2.6}$$

Where ρ is the mass density of the volume slab, which is measured in kg/m^3, and u is the particle displacement. The particle velocity (v) is the first time derivative of the particle displacement:

$$v = \frac{\partial u}{\partial t} \tag{2.7}$$

Once defined the particle and velocity and particle displacement, we can understand what is happening inside the body. Its internal particles suffer a mechanical displacement because of T and this displacement per unit of length is called Strain (S) and is defined as follows:

$$S = \frac{\partial u}{\partial z} \tag{2.8}$$

Now that we have the definition of strain (S) we can relate it with T by means of Hooke's law, which was derived in 1660 [80]. This law defines the linear relation between T and S as:

$$T = c \cdot S \tag{2.9}$$

Where c is the elastic constant of the medium. By means of the constitutive equations derived above (2.4)-(2.9), we can derive the one-dimensional mechanical or acoustical wave equation following a systematic procedure shown in [75]. First, we apply the time derivative to (2.8) and (2.9) and rearranging them we obtain:

$$\frac{\partial v}{\partial t} = \frac{1}{c}\frac{\partial T}{\partial t} \tag{2.10}$$

Now we apply the spatial derivative to (2.5) and the time derivate to (2.10) and equaling the cross derivatives we finally obtain the one-dimensional mechanical wave equation as follows:

$$\frac{1}{\rho}\frac{\partial^2 T}{\partial z^2} = \frac{1}{c}\frac{\partial^2 T}{\partial t^2} \tag{2.11}$$

From (2.11) we can compute the phase velocity of the mechanical wave as follows

$$v_a = \sqrt{\frac{c}{\rho}} \tag{2.12}$$

2.1.1. Derivation of the Solution of the Equation of Motion in a Non-Piezoelectric Slab.

In this section we are going to obtain the solution of the one-dimensional mechanical wave equation of motion for a non-piezoelectric medium. Then by means of this solution we will

understand how an acoustical wave propagates through it. First, we have to define our medium. This medium will be an isotropic slab, which is lossless and free charge medium. We define this slab with a thickness $d_p = z_2 - z_1$ and infinite lateral dimension (See Figure 2.2.). It is known that in all type of waves propagating in a medium are classified in two types called the incident and the reflected waves. These waves are solution of equation (2.11). Therefore, the mechanical wave can be written in its phasor form as follows.

$$u(z) = A^{+}e^{-jkz} + A^{-}e^{+jkz} \tag{2.13}$$

Where A^{+} and A^{-} are the amplitudes for the incident and the reflected waves respectively, then k is the wave number, which is defined in (2.14).

$$k = \frac{\omega}{v_a} \tag{2.14}$$

Where ω is the angular frequency. Then, if we want to obtain the particle velocity in both limits (z_1 and z_2) we have to compute the first derivate of (2.13) with respect to t

$$\begin{aligned} v_1 &= j\omega(A^{+}e^{-jkz_1} + A^{-}e^{+jkz_1}) \\ v_2 &= j\omega(A^{+}e^{-jkz_2} + A^{-}e^{+jkz_2}) \end{aligned} \tag{2.15}$$

Then, combining the two equations of (2.15) and making some trigonometric derivations, the incident and reflective waves can be written as follows.

$$\begin{aligned} j\omega A^{+} &= \frac{(v_1 e^{jkz_2} - v_2 e^{jkz_1})}{2j\sin(kd_p)} \\ j\omega A^{-} &= \frac{(v_2 e^{-jkz_1} - v_1 e^{-jkz_2})}{2j\sin(kd_p)} \end{aligned} \tag{2.16}$$

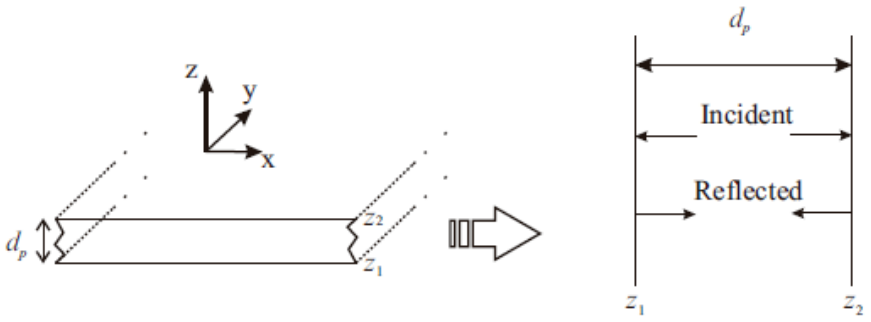

Figure 2. 2. Schematic view for the non-piezoelectric media where an acoustical wave is propagates through it [81].

So far, we have derived the particle displacement and velocities of propagation equations for a non-piezoelectric slab. With this information we are able to compute the acoustic impedance of the mechanical wave, which is defined as $Z=-T/v_p$ where T and v_p are 180° out of phase. Now, by considering the one-dimensional analysis we can derive F as in (2.17).

$$Z = \frac{-T}{v_p} = \sqrt{pc} = pv_p = \frac{ck}{\omega}$$
$$F = \frac{Ackv_p}{\omega} \tag{2.17}$$

Therefore, Hooke's law can be redefined as a function of the applied forces:

$$T = c\frac{\partial u}{\partial z} \rightarrow F = Ac\frac{\partial u}{\partial z}$$
$$F = jAck(A^{+}e^{-jkz} - A^{-}e^{jkz}) \tag{2.18}$$

Finally, we can relate the applied force F, particle velocity v_p and the acoustical impedance Z to obtain the solution of the one-dimensional mechanical wave in a non-piezoelectric slab.

$$F_1 = \frac{Z}{j\sin(kd_p)}(v_1 - v_2) + jZ\tan(\frac{kd_p}{2})v_1$$
$$F_2 = \frac{Z}{j\sin(kd_p)}(v_1 - v_2) + jZ\tan(\frac{kd_p}{2})v_2 \tag{2.19}$$

Now, we can outline (2.19) through a circuit representation (see Figure 2.3.). This model is related with the classical distributed T-impedance equivalent networks for a transmission line [82]. Hence, we can relate the applied force with an electrical voltage (V) and the particle velocity with a current intensity (I) through the circuit.

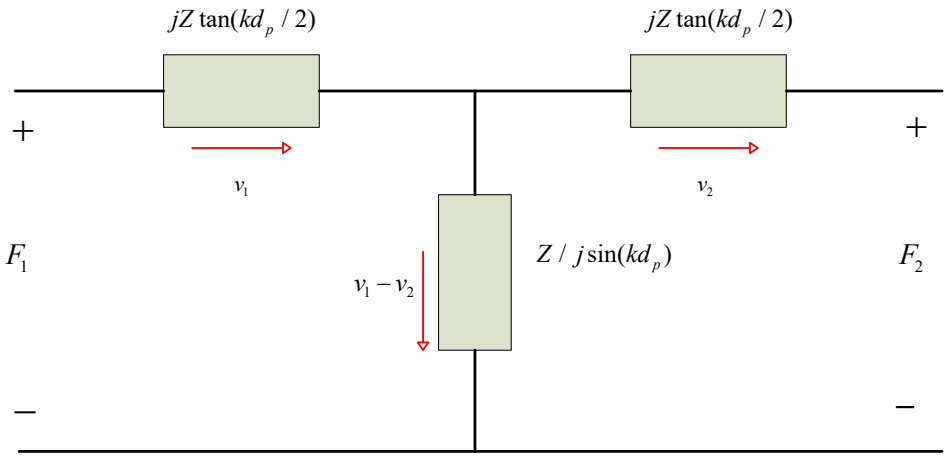

Figure 2. 3. T impedance equivalent circuit for an acoustical transmission line (non-piezoelectric media).

2.1.2. Derivation of the Solution of the Equation of Motion in a Piezoelectric Slab.

In this section, we will obtain the solution of the one-dimensional mechanical wave in a piezoelectric slab. Then we are going to derive the constitutive equations that relate the mechanical and electrical planes due to the piezoelectric effect. Since we will work with a piezoelectric slab, it is essential to make some considerations between the electrical and mechanical planes. First, by analyzing the transverse electromagnetic waves (TEM). The radiation impedance of a TEM wave can be obtained by computing the ratio between the transverse electrical and magnetic fields ($Z=E/H$). On the other hand, for the mechanical case, we have defined the acoustic impedance of the medium as the ratio of T and v_p. After deriving, the acoustic impedance can be rewritten as in (2.20), see [75]. Then, taking into account these considerations, the analogies between the mechanical and electric planes are summarized in Table 2.1 by means of the one-dimensional mechanical wave equation of motion and the traditional Maxwell equations in their differential form.

$$Z = j\frac{c\omega\vec{u}}{\vec{v}(v_p)} \tag{2.20}$$

Table 2. 1. Mechanical and electrical plane analogies [75].

One dimensional mechanical equations	**Maxwell equations**
Fundamental physical laws	
$\frac{\partial T}{\partial z} = \rho\frac{\partial v}{\partial t}$	$\nabla x\vec{E} = -\frac{\partial \vec{B}}{\partial t}$
$S = \frac{\partial u}{\partial z}$	$\nabla x\vec{H} = \frac{\partial D}{\partial t} + \vec{J}$
Constitutive equations	
$T = cS$	$\vec{D} = \varepsilon\vec{E}$
$v = \frac{\partial u}{\partial t}$	$\vec{B} = \mu\vec{H}$

Once we have defined these relationships, we recall the definition of piezoelectricity in order to understand how an acoustic wave propagates through a piezoelectric slab medium. This effect relates the mechanical and electrical plane in a crystal or piezoelectric material, hence we have to introduce the polarization vector, which is proportional to the electric field as follows:

$$\vec{P} = \varepsilon_0 \mathbf{K} \vec{E} \tag{2.21}$$

Where ε_0 is the electric permittivity in the free space and **K** is the electric susceptibility matrix (we write it in bold capital letters to avoid confusion with the wave number.). Using (2.21) and the electric displacement vector *D* definition in table 2.1, we can rewrite *D* as

$$\vec{D} = \varepsilon_0 \vec{E} + \vec{P} = \varepsilon_0 \vec{E} + \varepsilon_0 \mathbf{K} \vec{E} \tag{2.22}$$

$$\vec{D}_i = \varepsilon_{ij} \vec{E}_j, \qquad i = 1...3,\ j = 1...3 \tag{2.23}$$

Where

$$\varepsilon_{ij} = \varepsilon_0 (1 + \mathbf{K_{ij}}) \tag{2.24}$$

If the material is an isotropic medium the ε_{ij} matrix can be considered scalar, $\varepsilon_{ij} = \varepsilon_r \varepsilon_0$, where ε_r is the relative permittivity constant. In the free space $\varepsilon_r = 1$ and **K=0.** Since we are analyzing a piezoelectric material, the vector polarization not only occurs in the presence of an external electric field but also by a strain or stress due to the crystal deformation that causes charge separation. Then the vector polarization can be rewritten relating the stress and piezoelectric strain matrix as follows.

$$P_i = d_{ij} T_J, \quad i = 1...3, \quad J = 1...6 \tag{2.25}$$

Where *J* denotes two different dimensions in the space.

We have seen above that the strain or stress can cause an electric field, this effect is called the inverse piezoelectric effect and involves mechanical (*T* and *S*) and electrical variables (*E*, *D* and *P*). This effect can be represented by the ratio of *S* and *E* (*S*/*E*), which is related by means of the transposal piezoelectric strain matrix

$$S_J = d'_{iJ} E_i \tag{2.26}$$

Finally, the constitutive equations that relate the mechanical and electrical fields are in (2.27). The complete procedure to derive them can be found in [75]. As we can observe in equations (2.27) and (2.28), both effects of the piezoelectricity can be expressed in terms of the stress piezoelectric matrix **e**.

$$T = -\mathbf{e} : E + c^E : S \tag{2.27}$$

$$D = \varepsilon^S : E + \mathbf{e} : S \tag{2.28}$$

Where the superscripts *E* and *S* indicate that the mechanical and electrical properties have been computed at electrical field and strain constant values. The operator "**:**" indicates the matrix product. The phase velocity for a piezoelectric slab is written in equation (2.29).

$$v'_a = \sqrt{\frac{c'^E_{33}}{\rho}} = \sqrt{\frac{c^E_{33} + \frac{e^2_{33}}{\varepsilon_{r33}}}{\rho}} \tag{2.29}$$

Additionally, we can write down the energy-conversion efficiency of the piezoelectric slab, which expresses how good the electrical energy is transformed into a mechanical one and vice versa, by means of the piezoelectric coupling factor k^2 in (2.30). We can see in this equation that the conversion is only affected by the physical parameters of the material.

$$k^2 = \frac{e^2}{c^E \varepsilon^S}, \tag{2.30}$$

Finally, thermal effects can be considered in the constitutive equations, by means of the electro-thermo-mechanical model based on the Electric Gibbs function, which takes into account the thermal phenomena in the piezoelectric material [74], [78], [83]. These constitutive equations, depicted in the Heckmann diagram (see Figure 2.4.), are defined in equation (2.31).

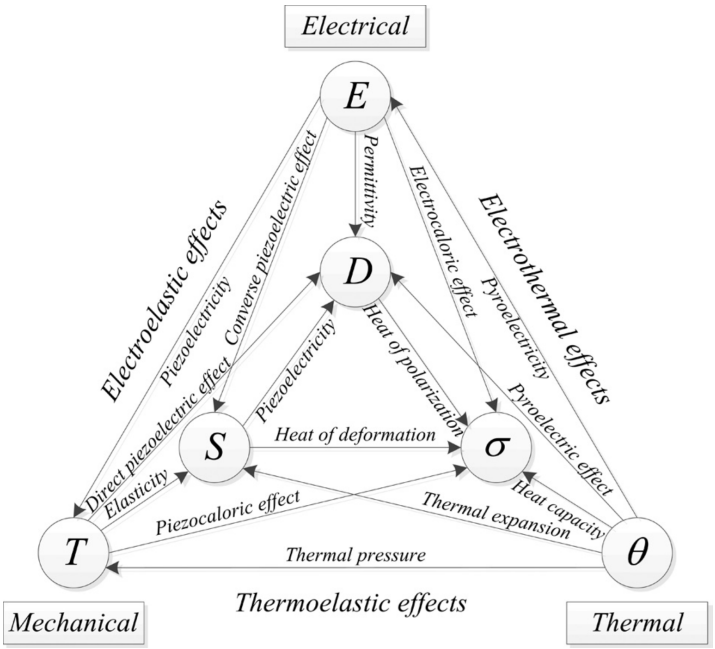

Figure 2. 4. Heckmann diagram showing the relations between the electrical, thermal and mechanical domains in a crystal [74]. Where T, S, E, D, θ, and σ are stress, strain, electric field, electric displacement, temperature, and entropy, respectively.

$$T = -e^{\theta} : E + c^{E\theta} : S - \tau^{E}\theta$$

$$D = \varepsilon^{S\theta} : E + e^{\theta} : S + \rho^{S}\theta \tag{2.31}$$

$$\sigma = \tau^{E} S + \rho^{S} E + r^{ES}\theta$$

Where τ^{E}, ρ^{S} and r^{ES} are thermal pressure, pyro electricity and heat capacity, respectively. They represent are the thermal parameters added to the constitutive equations. Once we have the tools and understood how an acoustic wave propagates across a piezoelectric medium, we can introduce the Mason's model, which is based on an acoustical transmission.

2.2. The most known one-dimensional models for Thin Film Resonators

We have presented the fundamental theory and concepts for the one-dimensional analysis for non-piezoelectric and piezoelectric materials. We have defined the constitutive equations and their equivalent circuits based on transmission lines. Hence, we are able to introduce the most common one-dimensional models used for modelling electroacoustic resonators. These models are defined as the mathematical representations of the behavior of sound waves in a piezoelectric and non-piezoelectric slab. The one-dimensional models typically assume that the lateral dimensions of the piezoelectric slab are much larger than their thickness, which allows them to simplify their constitutive equations because of the analysis is carried out only in the direction of the propagation wave (thickness direction). The two most common one-dimensional models are based on lumped-element and the transmission line analysis. These are the Butterworth Van Dyke and Mason models, respectively.

2.2.1. Mason's Model

One of the most used one-dimensional model in SMRs is the Mason's model. This tool is based on the distributed transmission line representation. Mason's model is capable of modelling the whole resonator structure including electrodes, acoustic reflector even the substrate. The model is represented as a series of connected sections in cascade, each of which has a specific material properties such as density, characteristic impedance and Young's Modulus. The behavior of the whole resonator is then described using a set of electro-acoustic equations (constitutive equations) along the transmission line. In the next sub-sections we are going to explain the physics

and math behind this one-dimensional model. On the other hand, if the reader wants to know more about these derivations we highly recommend these works [23], [73].

First, we have to make an assumption, which considers a thin film, large piezoelectric plate limited by two planes located at z_1 and z_2 (see Figure 2.5.). In this scenario, the acoustic wave propagates through the piezoelectric slab, which is excited by means of an electric field in the thickness direction. Since inside a piezoelectric material there is no free charge density ρ_e, the electric displacement vector $\vec{D}$ remains constant in the thickness direction, leading to

$$\nabla \cdot \vec{D} = \rho_e = 0 \tag{2.32}$$

Once we have considered this, our objective is to characterize the piezoelectric circuit in terms of voltage V and current I, since the piezoelectric is a dielectric material too. On the other hand, we could think that by applying an external electric field E, which causes an electron flow, the current that travels through a piezoelectric is purely a displacement current. However, this is not entirely truth as it will be discussed below. The displacement current is defined as

$$J = \frac{\partial D}{\partial t} = j\omega D \quad \Rightarrow I = j\omega DA \tag{2.33}$$

Where J is the displacement current density. As we need the voltage V, the electric field must be integrated along the piezoelectric slab thickness (z_1 up to z_2). First, to obtain the relation of the electric field in a piezoelectric material we must use the constitutive relation for the electric plane, then we have:

$$D = eS + \varepsilon^S E \tag{2.34}$$

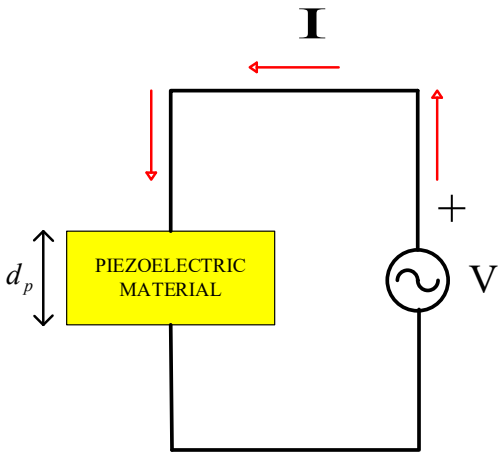

Figure 2. 5. Thin film piezoelectric slab limited by z1 and z2. The excitation is in the thickness direction.

Then, reordering (2.34) we can obtain the electric field as follows in (2.35), where the first term is the external electric field, and the second term is the internal electric field generated by the acoustical wave due to the piezoelectric effect.

$$E = \frac{1}{\varepsilon^S} D - \frac{e}{\varepsilon^S} S = \frac{1}{\varepsilon^S} D - \frac{e}{\varepsilon^S} \frac{\partial u}{\partial z} \tag{2.35}$$

Hence, we can compute the Voltage relation over the piezoelectric slab solving the integral of the electric field over z_1 and z_2 as.

$$V = \int_{z_1}^{z_2} E(z) dz = \frac{d_p D}{\varepsilon^S} - \frac{e}{\varepsilon^S} (u(z_1) - u(z_2)) \tag{2.36}$$

Where d_p=z_2-z_1 is the thickness of the piezoelectric plate, the particle velocity can be defined in equation (2.37). Additionally, D can be derived from (2.33) and voltage can be rewritten as in equation (2.38)

$$v = \frac{\partial u}{\partial t} = j\omega \tag{2.37}$$

Then voltage becomes

$$V = \frac{d_p}{\varepsilon^S} \frac{I}{j\omega A} + \frac{h}{j\omega} (v_1 - v_2), \qquad h = \frac{e}{\varepsilon^S} \tag{2.38}$$

Finally, we can obtain the total current in the piezoelectric material, which is defined below. As for the electric field, the current is given by two terms where the first one is the displacement current through a capacitance and the second term is the current generated by the conversion between the mechanical and electrical energy due to the piezoelectric effect (direct piezoelectric effect). Hence, this explains why the current in a piezoelectric material is not just a displacement current.

$$I = j\omega C_0 V + h C_0 (v_1 - v_2) \tag{2.39}$$

Then, the static capacitance C_0 between the electrodes of the piezoelectric slab is given by:

$$C_0 = \frac{\varepsilon^S A}{d_p} \tag{2.40}$$

Now, we can relate the applied force F, particle velocity v_p, acoustical impedance Z and the current term due to the piezoelectric effect so we have next relations for F_1 and F_2

$$F_1 = \frac{Z}{j\sin(kd_p)}(v_1 - v_2) + jZ\tan\left(\frac{kd_p}{2}\right)v_1 + \frac{h}{j\omega}I$$
$$F_2 = \frac{Z}{j\sin(kd_p)}(v_1 - v_2) + jZ\tan\left(\frac{kd_p}{2}\right)v_2 + \frac{h}{j\omega}I \tag{2.41}$$

We have derived the relations between the acoustical and electrical planes in (2.41). Therefore, we can derive an equivalent circuit based on the T transmission line model [82]. Figure 2.6 shows the Mason's model equivalent circuit, which consider the acoustical-electrical planes. This model consists of two acoustical ports where there clearly exist two forces (F_1 and F_2) which are applied. On the other hand, this model also has one electrical port, which is derived by means of V and I. Furthermore, there is a transformer element that indicates the conversion between mechanical to electrical energy and viceversa. The hC_0 ratio of the transformer can be derived using Kirchhoff's voltage law in both loops in the circuit. One more thing to notice in the electric port of the piezoelectric slab is the ($\boldsymbol{-C_0}$) capacitance. This is due to current travelling away from the node (V and I definition in the circuit) to the transformer, so, the voltage drop in the capacitor must be negative.

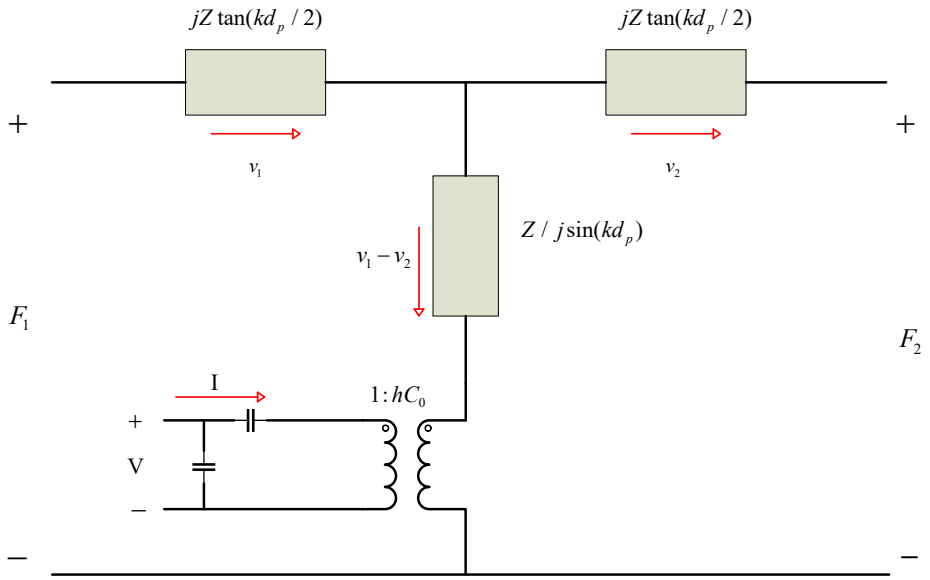

Figure 2. 6. Equivalent Mason Model for a piezoelectric slab represented by the T-impedance transmission line network.

Now we can obtain the electrical input impedance with arbitrary loads in the mechanical ports (see Figure 2.7.). Where Z_H is the top mechanical impedance and Z_L corresponds to the bottom mechanical impedance. Then, we can obtain both impedances based on Fig. 2.7 and equation (2.41), and then we have:

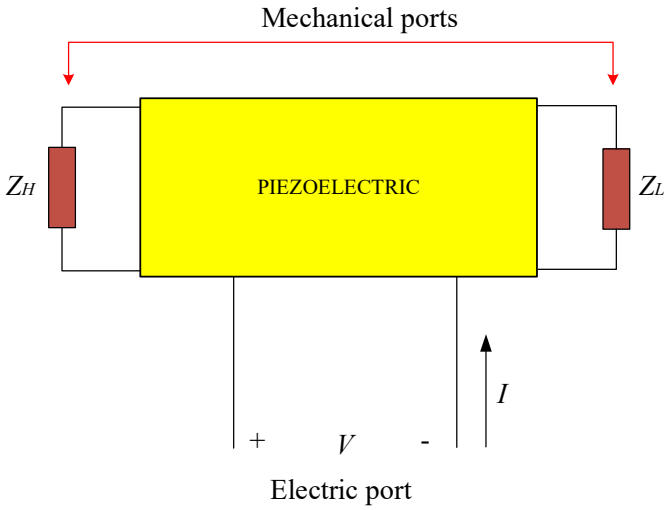

Figure 2. 7. Piezoelectric material with two arbitrary load impedances (ZH and ZL) in the mechanical ports.

$$-Z_H v_1 = Z_p\left(\frac{v_1}{j\tan(kd_p)} - \frac{v_2}{j\sin(kd_p)}\right) + \frac{h}{j\omega} I$$

$$-Z_L v_2 = Z_p\left(\frac{v_1}{j\sin(kd_p)} - \frac{v_2}{j\tan(kd_p)}\right) + \frac{h}{j\omega} I \tag{2.42}$$

Where Z_P is the piezoelectric impedance, then deriving this equation to obtain the *V/I* relation

$$\frac{v_1}{I} = \left(\frac{h}{\omega}\right)\left(\frac{Z_p(\cos(kd_p)-1) + jZ_L\sin(kd_p)}{(Z^2{}_P Z_H Z_L)\sin^2(kd_p) - j(Z_H+Z_L)Z_p\sin(kd_p)\cos(kd_p)}\right)\sin(kd_p)$$

$$\frac{v_2}{I} = \left(\frac{h}{\omega}\right)\left(\frac{-Z_p(\cos(kd_p)-1) - jZ_L\sin(kd_p)}{(Z^2{}_P Z_H Z_L)\sin^2(kd_p) - j(Z_H+Z_L)Z_p\sin(kd_p)\cos(kd_p)}\right)\sin(kd_p) \tag{2.43}$$

If we remember, *V/I* can be written as follows

$$\frac{V}{I} = \frac{h}{j\omega}\left(\frac{v_1}{I} - \frac{v_2}{I}\right) + \frac{1}{j\omega C_0} \tag{2.44}$$

Finally, we can obtain the electrical impedance for the piezoelectric slab with arbitrary loads, where the piezoelectric is excited in its thickness direction. Further, the piezoelectric impedance normalizes both arbitrary impedances.

$$Z = \frac{1}{j\omega C_0}\left(1 - \frac{k_t^2}{kd_p}\frac{\tan(\phi)}{\phi}\frac{\left(\frac{Z_H + Z_L}{Z_p}\right)\cos^2(\phi) + j\sin(2\phi)}{\left(\frac{Z_H + Z_L}{Z_p}\right)\cos(2\phi) + j\left((1 + \frac{Z_H Z_L}{Z^2_p})\right)\sin(2\phi)}\right) \tag{2.45}$$

Where $\phi = kd_p/2$, and k_t is called the electromechanical coupling constant, which is a figure of merit for the piezoelectric material and is defined as follows

$$k_t^2 = \frac{e^2}{Z_p \varepsilon_0 \varepsilon_r v_p} \tag{2.46}$$

Summarizing, equation (2.45) is an important expression for resonators based on BAW-Thin film technology with special attention in SMRs, aim of this thesis. This equation can relate the electrical behavior of the piezoelectric material with any impedance load attached to the mechanical ports of the piezoelectric model (see Figure 2.8a). Hence, we can consider a scenario where several impedance loads are mechanically coupled with the piezoelectric material (see Figure 2.8b), so, it is possible to compute Z_H and Z_L and then carry out the electrical analysis to obtain the electrical impedance and the electromechanical coupling constant. As we mentioned before, we can derive the electro-mechanical equations for SMRs with different layers, (i.e., bottom and top electrodes, acoustical reflector and the substrate) considering the material properties of each material.

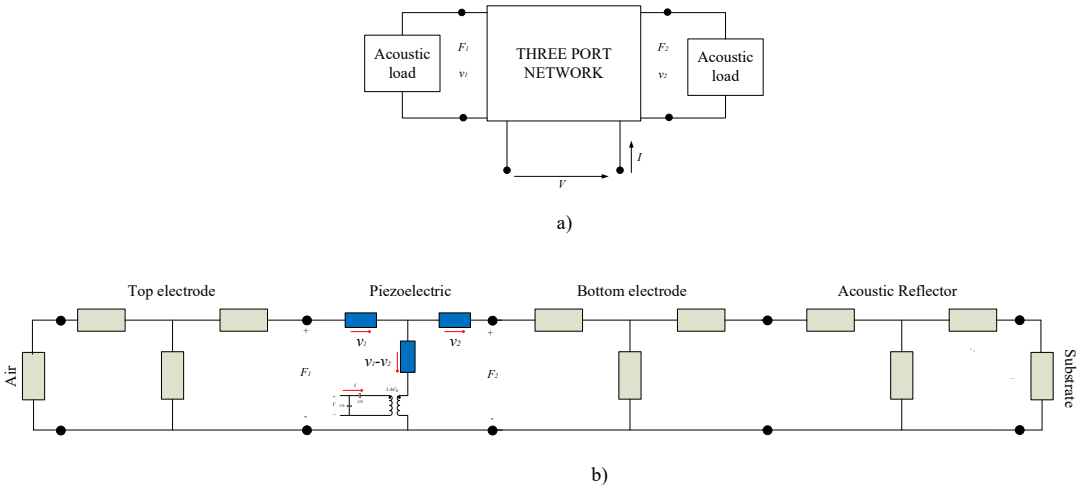

Figure 2. 8. a) Three port Mason's model representation for a piezoelectric material with two mechanical loads attached. Where one represents the top air impedance load (left) and the second one corresponds to the substrate load impedance (right) and finally the third one is the electrical port (below). Additionally, b) represents a SMR configuration by means of Mason's model transmission line T network (the top impedance load corresponds to air and the bottom one is related to the substrate).

2.3. Butterworth Van Dyke Model

The Butterworth Van Dyke model (BVD) is an electrical model introduced by Butterwoth and K.S. Van Dyke in 1914 and 1925, respectively. This circuit models the effects of the mechanical resonance by means of the electrical impedance *Z*. The model is based on lumped elements (capacitors, inductors and resistors) and is principally composed by a capacitance C_0 called static capacitance, which is connected in parallel with an acoustic or motional arm, L_1 and C_1. Additionally, in parallel to this branch there are more acoustic arms representing the higher harmonics (L_{n-1} and C_{n-1}), as we can see in Figure 2.9 a). However, for the practical case in electroacoustic resonators, we use only the first motional arm, which represents the first resonance. Henceforth, the higher order harmonics can be neglected, and the circuit becomes only C_0 and one acoustic arm (see Figure 2.9 b). On the other hand, as we have noticed in Figure 2.9 a) and b), the model does not have any resistive elements, hence it cannot take into account any losses in the system. This means that the response is ideal (the efficiency of the transformed energy is 100 %), which is not a realistic scenario. To solve this, a more accurate model is taken into account, which is called the modified Butterworth Van Dyke's model (*mBVD*), see (Figure 2.9 c), which was introduced in [84]. Where R_x represents losses due to metallic electrodes, L_x can be due to the measurement configuration or electrode layout, R_0 is due to the material losses of the piezoelectric (i.e., dielectric ones) and R_1 is associated to the acoustic-mechanical losses.

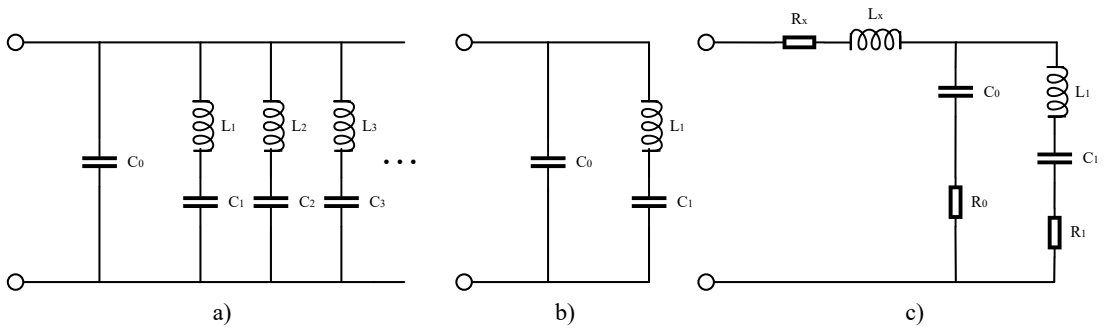

Figure 2. 9. a) Basic BVD model considering the higher harmonics where each motional branch represents a harmonic resonance, b) BVD main resonance circuit model, c) mBVD taking into account losses.

2.3.1. Electrical Impedance

We can derive the electrical input impedance of the equivalent circuit in terms of its angular frequency (ω). For both cases, Figures 2.9 b) and c), the first one corresponds to the ideal case without losses, so this one is straightforward to derive by means of classical circuit theory. Both

cases are expressed in terms of their real and complex values, that is, resistance (R) and reactance terms (X_L and X_C) respectively. Then the input electrical impedance without losses is:

$$Z(\omega) = \frac{j(\omega L_1 - 1/\omega C_1)}{1 - \omega^2 C_0 L_1 + C_0 / C_1} \tag{2.47}$$

Then we can derive the electrical impedance taking into account the losses due to different mechanisms as we have explained. Using equation (2.47) and adding losses we obtain (2.48).

$$Z(\omega) = j\omega L_x + R_x + \left[\frac{1}{R_0 + 1/j\omega C_0} + \frac{1}{R_1 + j(\omega L_1 - 1/\omega C_1)} \right]^{-1} \tag{2.48}$$

With (2.48) we are able to compute the electrical input impedance of the resonators in terms of the frequency, leading us to observe the resonance frequencies.

2.3.2. Series and Parallel Resonances

In Figure 2.10, we can see the electrical response of the BVD model. This behavior corresponds to the electrical input impedance and also the phase for a typical electroacoustic resonator. The minimum and maximum values of the electrical impedance occur at the series and parallel resonances f_s and f_p respectively. These frequencies are also called resonance f_r and anti-resonance f_a frequencies. At series resonance, the impedance becomes purely resistive because the reactance of the motional arm becomes almost zero (short circuit), then only R_x and R_1 limit the current through the motional arm. Hence, the value of the impedance at series resonance is minimum and the resonance can be computed by means of (2.49).

$$f_s = \frac{1}{2\pi\sqrt{L_1 C_1}} \tag{2.49}$$

In the case of the parallel resonance (anti-resonance frequency), the motional arm can be considered an open circuit, which means the impedance at this frequency tends to infinite. Hence the condition of zero reactance leads to the next equation showed in (2.50).

$$f_p = \frac{1}{2\pi}\sqrt{\frac{C_1 + C_0}{L_1 C_1 C_0}} \tag{2.50}$$

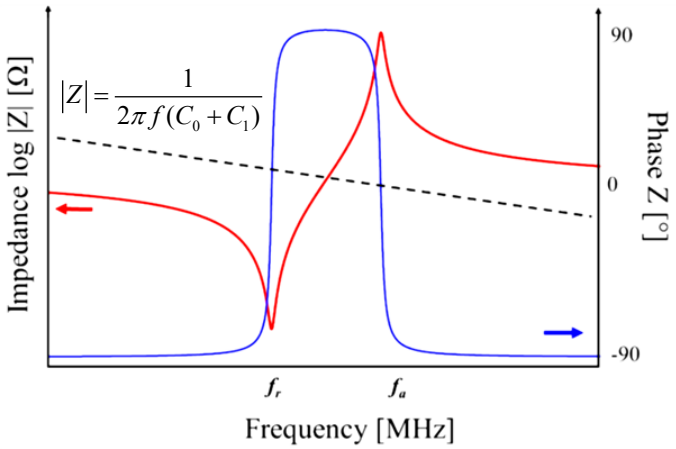

Figure 2. 10. Electrical behavior of a typical electroacoustic resonator, where the red curve is the impedance in Z [dB Ohms] and the blue one corresponds to its phase [°]. The response is in the frequency domain [9].

The response of the electroacoustic resonator shown in Figure 2.10, corresponds to the magnitude of the electrical input impedance in dBΩ and its phase in degrees, red and blue, respectively. The minimum value of Z is for f_s and the maximum corresponds to f_p. In both cases, the phase of the impedance suffers a shift of 180° from -90° to 90° and vice versa (see blue curve). Additionally, far from the resonance frequencies the behavior of the resonator tends to a simple capacitor. Once we computed the electrical impedance we should analyze how efficient is the electrical energy transformed into a mechanical and vice versa, and how efficiently this energy is stored. There are two parameters that are able to compute these quantities. These parameters are the piezoelectric coupling coefficient (kt^2) and Quality factor (Q).

2.3.3. Quality Factor

There is an ideal hypothetical scenario where a resonator would oscillate infinitely without damping mechanisms that interfere with its movement, even if the applied force at the beginning were removed. That means there is no loss of energy in this ideal scenario. However, this is not possible in the real world since there are different damping mechanisms that contribute to energy losses. There is a parameter that can measure the quantity of lost energy, which is called quality factor (Q). It is defined as the ratio of the stored energy in the piezoelectric of the resonator to the energy dissipated per cycle due to damping mechanisms. The formal definition of Q can be expressed as follows:

$$Q = 2\pi\left(\frac{stored\ energy}{dissipated\ energy\ per\ cycle}\right) = 2\pi\left(\frac{stored\ energy}{power\ loss}\right) \qquad (2.51)$$

Q can also be computed using the steepness of the phase curve at resonance and antiresonance frequencies (f_s and f_p) (see equation 2.52). There is a recent method presented in [85]. This new formulation provides reliable Q values over the full range of frequencies response. The first method is based on the measured impedance and admittance values and the second one is based on the S parameters.

$$Q_{s,p} = \frac{f_{s,p}}{2}\left(\frac{d\phi(Z)}{df}\right)_{f_{s,p}} \tag{2.52}$$

$$Q\ (\omega)\ =\ \frac{\omega\ \frac{d\phi_L}{d\omega}\ mag(S(1,1)_L)}{[1-(mag(S(1,1)_L))^2]} \tag{2.53}$$

Additionally, there is another way to compute Q for both resonances, which is an approximation derived from the modified mBVD model. Both approximations are represented in equation 2.54.

$$\begin{aligned} Q_s &\approx \left(\frac{\omega_s L_1}{R_x + R_1}\right)_{\omega=\omega_s} \\ Q_p &\approx \left(\frac{\omega_p L_1}{R_0 + R_1}\right)_{\omega=\omega_p} \end{aligned} \tag{2.54}$$

These last expressions are useful since they consider the losses mechanisms from the mBVD equivalent circuit model, hence we can compute a quick approximation of Q. Furthermore, these equations allow us to explain how the loss mechanisms affect the stored energy process since they include now R_x, R_0 and R_1 and also L_x. In the first case (Q_s), the quality factor is controlled by the series resistance (R_x) introduced by the top and bottom electrodes. Meanwhile the Q_p factor is influenced only by the internal losses (R_0). Those effects are due to the fact that at resonance (series resonance) the impedance of the motional arm is reduced to R_1, making the total current to be maximum and flowing through the motional arm. At this point the influence of R_x is the maximum. Meanwhile, at parallel resonance the motional arm becomes almost an open circuit because of its high impedance, making the current reach its minimum value and flowing only through C_0. At this point R_0 gains a more pronounced effect and the influence of R_x is minimum [23].

2.3.4. Piezoelectric Coupling Coefficient

The effective piezoelectric coupling coefficient measures how electrical energy is transformed into the mechanical one and vice versa. The electromechanical coupling coefficient measures this conversion of energy in the whole resonator structure. On the other hand, $keff^2$ can be computed in terms of f_s and f_p, specifically their relative frequency separation, as we can see in equation (2.55). This expression is the most accepted since is used for piezoelectric devices and was proposed by the IEEE standard of piezoelectricity [86].

$$keff^2 = \frac{\pi}{2}\frac{f_s}{f_p}\frac{1}{\tan\left(\frac{\pi}{2}\frac{f_s}{f_p}\right)} \tag{2.55}$$

2.4. Summary

We have presented the one-dimensional analysis and solution of the acoustical equation of motion using the second Newton's and Hook's laws, respectively in order solve the acoustical propagation in a piezoelectric and non-piezoelectric materials since electroacoustic resonators are composed principally of two of them (piezoelectric and electrodes). Next, we have introduced the two most known one-dimensional models used to the designing of electroacoustic devices such as SAWs and BAWs. Both models are going to use in this thesis to design our SMRs, although both there are going to be modified and adapted according to our necessities. Additionally, we have introduced two parameters that can measured the efficiency for the transformed energy (i.e., mechanical to electrical) and also how much of this energy is stored in the resonator, these parameters are the electromechanical coupling coefficient and quality factor, respectively.

Chapter 3

SMRs Based on AlN and the Updated Version Models

We start this chapter by briefly describing the fabrication process of our SMRs based on AlN (section 3.1). These devices were manufactured to verify our updated developed models. Afterwards, we describe some designed devices in terms of their geometry (different shapes such as pentagons, ellipses and squares) and also the size of the active area (from 31,512 μm^2 up to 142,912 μm^2). In addition, we describe a new phenomenon that affects the quality factor of the resonators. This new effect is the probing spot and appears as Ohmic losses due to the series resistance of the thin films (top electrode). This effect has different behaviors according to the location where the RF probes make contact with the active area of the resonator. We have included an explanation of both phenomena since they can directly affect the performance of our devices (see section 3.2). A direct is the presence of a new-coupled resonance that affects the fundamental series resonance frequency (f_s) and its quality factor (Q_s). In order to include these phenomena in our models we have updated both the mBVD and Mason one. The update consists in adding a new resonator that is coupled through a capacitance. In the case of the mBVD, we have connected in parallel a new electrical branch. Then, for Mason, we have included a new complete resonator also connected in parallel but only through its electric port, since we are interested in the electrical response. Both models are explained in section 3.3 and its subsections.

Finally, in section 3.4, we briefly explain how our models can take into account the temperature input. We have carried out simulations at different temperatures and we have observed good results in both models. These results will be shown in chapter 5.

3.1. Fabrication Process

We have fabricated SMRs based on acoustic reflectors made of low acoustic impedance Silicon Dioxide (SiO_2) and high acoustic impedance Molybdenum (Mo), with thicknesses of 620 and 629 nm, respectively (see Figure 3.1.). In between each layer a thin Titanium film (15 nm-thick) was used to improve the adhesion. The reflector is placed onto the substrate, which is Silicon (Si). Both materials were deposited by a pulsed-DC sputtering technique [48], [49]. The

thicknesses of these layers correspond to λ/4 for the frequency design of 2.5 GHz. To act as bottom electrode, a thick Ir film was evaporated (120 nm-thick) on top of the acoustic reflector. Onto the Ir bottom electrode, a c-axis oriented AlN thin film (1000 nm) was deposited in an ultra-high vacuum sputtering system. The system is pumped with a cryogenic pump to a base pressure of less than 10^{-8} *Torr* and is fitted with a sample transfer system to avoid oxygen contamination in the deposition chamber. The high purity Aluminum target was sputtered in 40:60 Ar/N2 admixtures with a pulsed DC power supply operating at 250 KHz and 1200 W. A substrate temperature of 400ºC and RF substrate polarization during the deposition allowed to control the stress to low compressive values (<200 MPa). Further, we have used a Molybdenum top electrode (150 nm-thick). The structure makes use of a capacitive coupling to reach the bottom electrode avoiding bias through the AlN film. To pattern the resonators effective area, lithography processes were used.

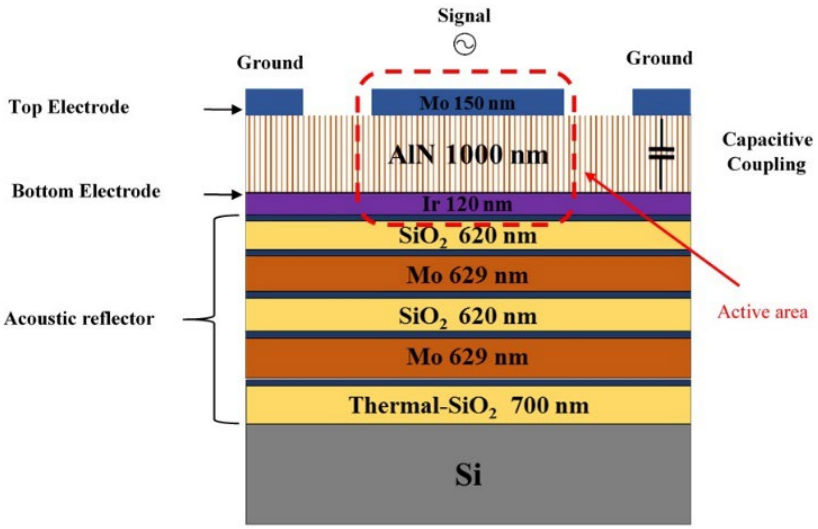

Figure 3. 1. SMR with the capacitive coupling model between the top and bottom electrodes. The thickness of the acoustic reflector corresponds to λ/4 to operate at 2.5 GHz. In the short-dash red square we can see the effective area resonator, where occurs the piezoelectric effect.

We have presented in this section a representative case of our fabricated resonators. However, the geometry configuration, materials and reflector layers can vary along the modelling and experiments of this thesis. Additionally, we will also have cases with a passivation gold (Au) layer on the top electrode. This layer is typically used to avoid oxidation at high temperatures.

3.2. Geometry of Our SMRs

We have fabricated SMRs with various geometries, including pentagons, hexagons, squares and ellipses (see the mask used in Figure 3.2.). However, due to the vast number of configurations,

we have only provided detailed descriptions of a few selected geometries as they serve as representative examples for the whole batch. Each resonator has different effective area. For our resonators this area is given by Area 1 (Figure 3.3). This effective area is the portion of the resonator where almost the whole energy is stored. The effective area in Figure 3.3 corresponds to a Pentagon shape. Additionally, our designs have a path (Area 2), which is the place where we made the contact landing with RF probe tips (those probes will be described in chapter 4, section 4.1.8.) in order to carry out the extraction of the scattering parameters of our resonators. Area 2 is also going to be considered as a part of the effective one since it has shown effects on the performance (this effect will be discussed in this chapter in section 3.2.1). It is important to notice that almost in all cases, Area 2 is smaller than Area 1.

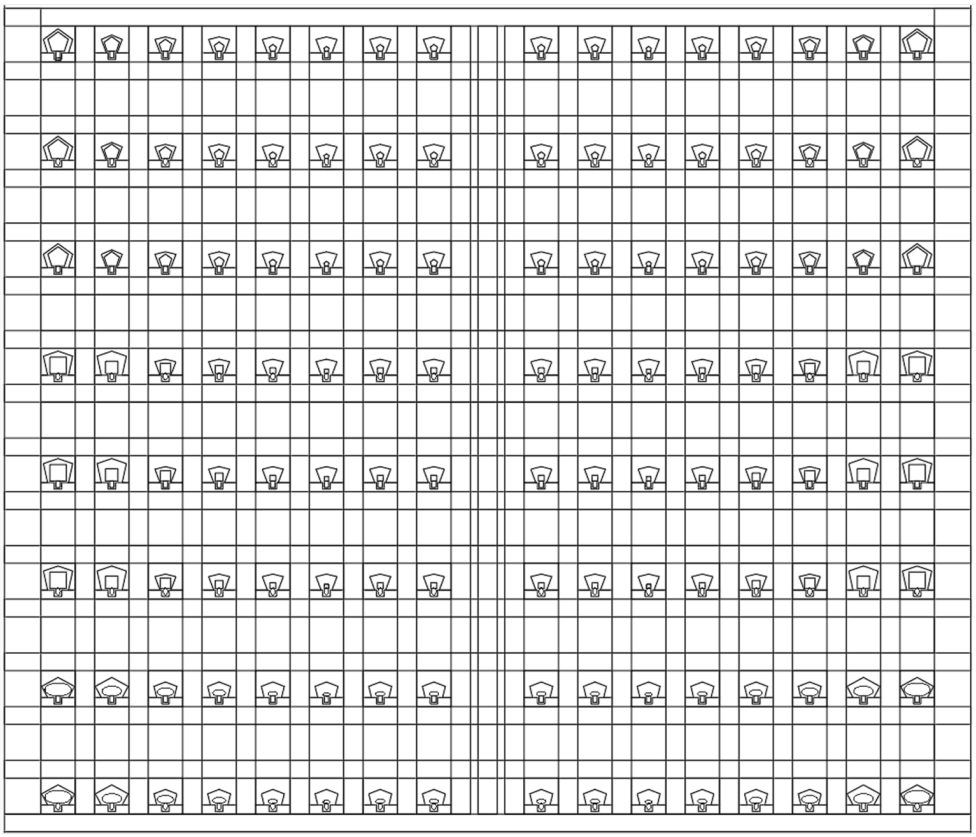

Figure 3. 2. Mask used to pattern the active area of our SMRs.

In Figure 3.3 we represent the values of the shape lengths in capital letters to simplify the interpretation of the figure. In addition, in the Table 3.1, there is a summary of the dimensions for different resonators. The values reported are length and areas. The units of these variables are in micrometers and square micrometers, respectively. Finally, in Figure 3.3 we show that our SMRs have only one port, which is the path where the RF signal is applied. Around the active area there is coplanar ground plane. Hence, the configuration of our devices is Ground-Signal-Ground (GSG). In almost all cases, the path signal is a rectangle shape, although it can vary according to the resonator.

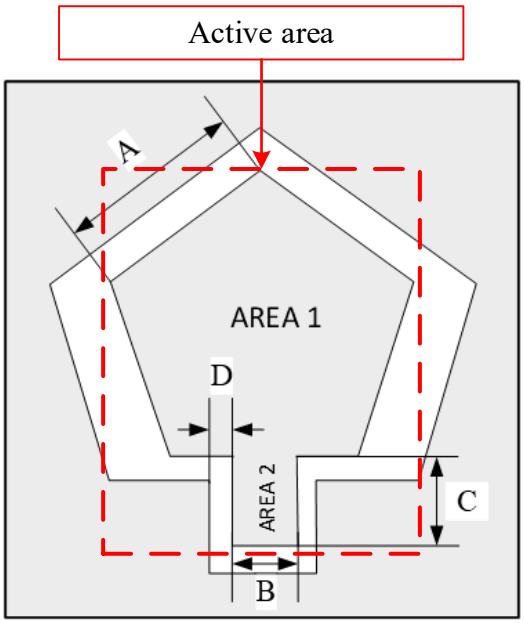

Figure 3. 3. Top view of one SMR, the effective area of the resonator is principally Area 1.

Table 3. 1. Size of the areas and lengths of the resonators.

Device	A [µm]	B [µm]	C [µm]	D [µm]	Area_1 [µm²]	Area_2 [µm²]	Total_Area [µm²]
1A	235	80	120	30	95,105	9,600	104,705
1B	176	80	120	30	53,496	9600	63,096
B3	100	80	190	30	10,000	152,000	162,000
1C	145	80	120	30	36,558	9,600	46,158
1D	112	80	120	30	21,912	9600	31,512
E11	181	175	190	30	56,761	29,157	85,918
F9	181	115	99	45	56,761	17,564	74,321
F10	181	115	99	45	56,761	17,564	74,321
F11	181	175	190	30	56,761	29,163	85,924
H5	439	53	401	73	192,316	-	192,316
J10	249	40	230	52	109,182	-	109,182
K8	272	80	190	30	127,712	15,200	142,912
K12	181	80	190	30	56,761	15,200	71,961

3.2.1. Effective Area and Probing Spot effects

The size of a resonator is an important parameter that also affects its performance, especially for devices based on BAW-Thin Films technology such as SMRs. This size is defined as the effective or active area of the resonator. It is marked in Figures 3.1 and 3.3 inside the red dash line square. The effective area has a limit in its size before the performance of the resonators

would be affected, this effect was demonstrated by simulations and measurements in [87] and [17], respectively. Henceforth, we have deeply investigated this effect. We have carried out simulations to obtain such limit and how this affects our resonators. The simulations were carried out with different sizes of the active area. The proposed resonators can be seen in the mask represented in Figure 3.2. On the other hand, there is another factor that could affect the response of the resonators. This effect occurs when we change the location where we make contact with the active area of the resonator in order to get measurements. This effect is called the landing or probing spot in the rest of this thesis. This last effect has also been studied in [88]. The probing spot effect can be explained by means of the sheet resistance. The resistance (R) of a thin film is defined as follows.

$$R = R_s \frac{L}{W} \tag{3.1}$$

Where, R_s is the sheet resistance (series resistance), L and W are the dimensions of the thin film, i.e., length and width, respectively. The R_s value is the same in all places and cases of the thin film since the thickness of the top electrode does not vary. In most of our resonators the material of this electrode is Molybdenum (Mo), and we can say that it has good uniformity and can be considered with the same thickness along the active area. Nevertheless, if we consider L when we want to measure at the pad or center of our geometry resonators, we can assume that the path travelled by a current from the pad to the opposite border is larger than from the center to the borders (see Figure 3.4.). The orange dot represents the place where the measurement could be taken (probing spot). We will explain two cases of this effect, pad and center, respectively. First, if we took a measurement at the pad, we could consider one resonator just below the probing spot with high quality factor, in parallel with several infinitesimal resonators with lower quality factors due to the larger path to the opposite border of the resonator. Secondly, in case of the center spot, the infinitesimal resonators in parallel have higher quality factor due to the shorter paths to the borders. We have learned by means of simulations that both effects (size of the active area and probing spot) contribute to generate a small new resonator. This new resonator has its own series resistance. Furthermore, we have learned that the resonance frequency of this new second resonator is very close to the main series resonance, which means that both effects contribute to the performance of our SMRs. In order to simulate these effects, we have to modify and update the mBVD and Mason models. Both models have shown excellent results with high accuracy. This is going to be demonstrated in Chapter 5, sub-section 5.1.3.

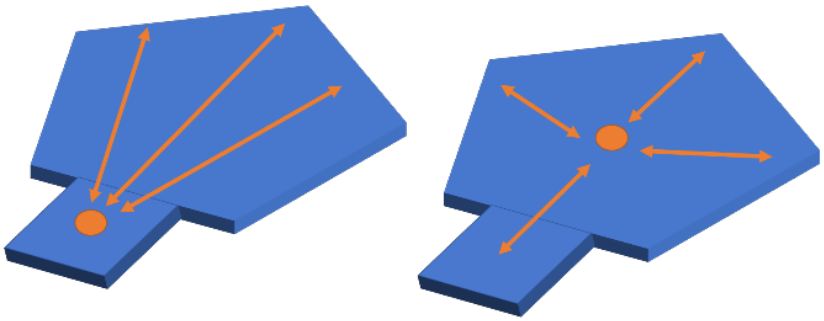

(a) (b)

Figure 3. 4. Lengths travelled by the current when measuring occurs at the pad (a) and center (b). Different lengths (L) influence the series resistances of the resonators.

3.3. Two Branches-Design

There are different one-dimensional models to design SMRs, some of them are based on distributed elements such as Mason and Krimholtz, Leedom and Matthae (KLM) models [89]. On the other hand, there is an electrical model based on lumped elements, which is known as BVD model. The most used of those mentioned above for SMRs are the Mason and BVD ones. In case of the mBVD model. It takes into account the loss mechanisms in the resonator and it is a convenient electrical equivalent circuit for fast simulations that can extract the electrical parameters. However, the BVD model does not take into account the whole structure of the resonator and this is necessary since our resonators are fabricated in the SMR configuration. For these cases, Mason's model is more suitable because it allows a more direct relation of the physical magnitudes with the electrical response of the device. Nevertheless, both models are not able to consider the effects mentioned in sub-section 3.2.1. Since we are interested in understanding and including those effects, we have updated the modified mBVD version by means of a new parallel branch (see Figure 3.5.) in order to take into account the new series resonance that appears near the main one due to the size of the effective area and the landing spot. Subsequently, we have used the results of the updated mBVD as an input to modify the Mason's model for a better understanding of the underlying mechanisms that can explain the electrical performance of the resonators. The update in the Mason's model also consists in adding a new branch connected in parallel to the main resonator. Since we want to know the electrical response of the resonator, we have connected this new branch in parallel but only the electrical ports.

3.3.1. Modified Butterworth Van Dyke, Updated Version

To explain the origin of these new resonators, we present the results of the electrical input impedance as a function of frequency ($Z(\omega)$ in dB Ohms) of two measured resonators, which are shown in Figure 3.6 a) and b). These devices correspond to resonators (1A) and (1B) with different areas: 104,705μm^2 and 63,096 μm^2, respectively. Both resonators have a pentagon shape as part of its active area (see Figure 3.7.). In Addition, in the second row of both Figure 3.6 a) and b), we add the real parts of the electrical impedance, which include insets at low frequencies in order to observe the changes in the series resistance at different probing spots and different size of the active area. In Figure 3.6 b) we can see that the series resistance for the smallest resonator is lower when we extracted it at the center (red solid line), as we have explained in section 3.2.1. Although we can see these differences between each resonator at each probing spot, we still need a proper model to account for the Ohmic effects (series resistance in the electrodes) at the main resonance frequency in our SMRs. We have designed and implemented a combined version of the mBVD model by adding a new resonator (additional series resonance) in parallel with the main one. This second resonator is capacitively coupled through C_{02} (see Figure 3.5.). In this updated version we have included the series resistance for the main and the second resonator that correspond to R_{x1} and R_{x2}, respectively. Considering the mentioned definition of the resistance of thin films in equation (3.1), we can explain how for devices with smaller areas, the difference in series resistances (R_{x1} and R_{x2}) when measuring at different spots are going to be less pronounced since in a small area the lengths (L) are very similar regardless of the spot. In addition, since a thin film resonator can be considered as infinitesimal resonators connected in parallel, for small device, we can consider that almost all of the infinitesimal resonators have the same series resistance. On the other hand, the larger the area of our devices (i.e., 1A), the bigger the number of resonators in parallel. The resonators considered at a further distance from the measuring point have larger series resistances. In our models, this is going to be translated to bigger differences between R_{x1} and R_{x2}. We are going to use these series resistances in order to model the two resonators connected in parallel as we have proposed in our updated model.

The fact that the new resonator appears as a series resonance only reveals that it is strongly related with the series resistance. The larger the area of the resonator the higher its resistance values, which translates to a degradation of the quality factor. The inductors L_{x1} and L_{x2} in the model are necessary for a wideband modelling but they may not be necessary for the narrowband simulations. The existence of such inductors might be due to the input pads of the resonator itself and are required for a proper de-embedding of their performance. The simulations were carried out by means of Advanced Design System (ADS) [90].

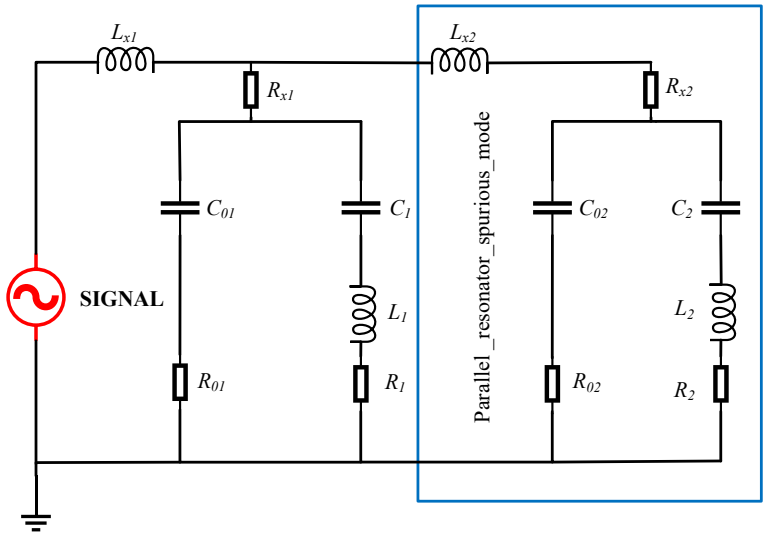

Figure 3. 5. Our updated mBVD circuit model, including the main resonator a) and the new resonator in parallel b) that accounts for the additional series resonance.

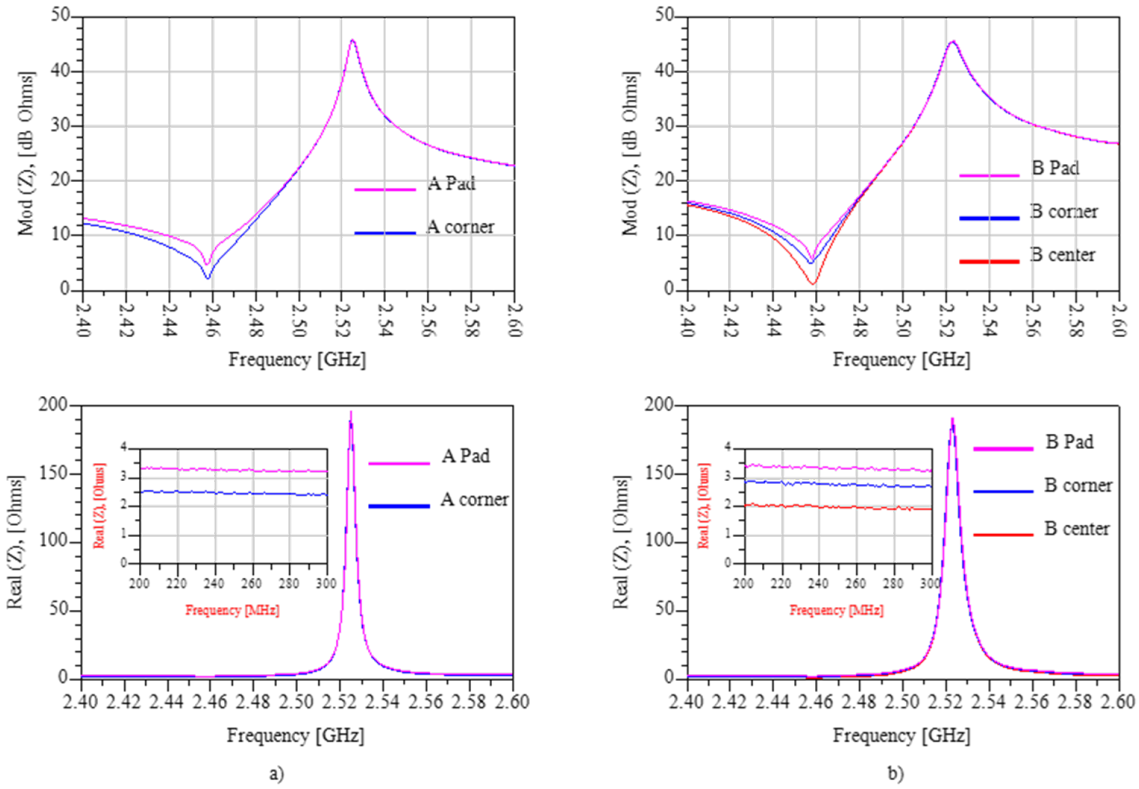

Figure 3. 6. Electrical impedances, magnitude and real parts measured at the pad, corner and center positions; (a) device A and (b) device B. Insets in the Real (Z) graphs show series resistances values at low frequencies.

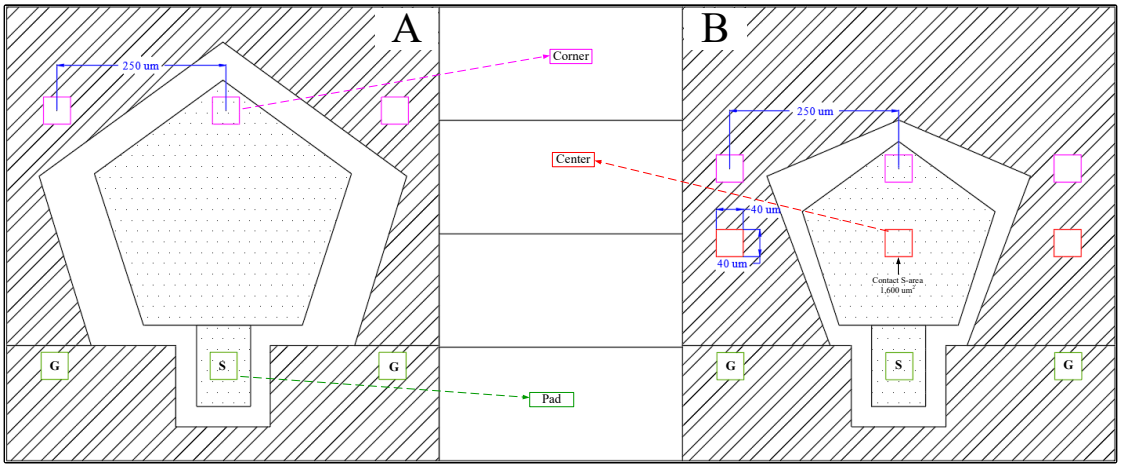

a) b)

Figure 3. 7. Topologies of the resonators measured at specific spots with a GSG probe: (a) Large resonator of 104,705 um2 (b) small resonator with 63,093 um2. The lines textured area shows the ground connection (capacitive coupling to the bottom electrode) and the dots textured area shows the active area of the devices. To be noted that the S-probe is directly connected to the active area of the devices.

3.3.1.1. The electrical Impedance

We have used two ways to compute the electrical input impedance of the updated version of mBVD model. The first method consists in calculating the equivalent impedance ($Zeq(\omega)$) from the circuit showed in Figure 3.5. By means of circuit theory we can simplify this circuit in small sections in order to obtain the new equivalent circuit (see Figure 3.8.). In this equivalent circuit, we represent each resonance with a different color: blue for the main and red for the new one. We have reduced it to three impedance blocks for each resonator in order to simplify the analysis. Once we have followed the four steps shown in the equivalent circuit we are able to compute the equivalent impedance of the updated mBVD according to equation (3.2).

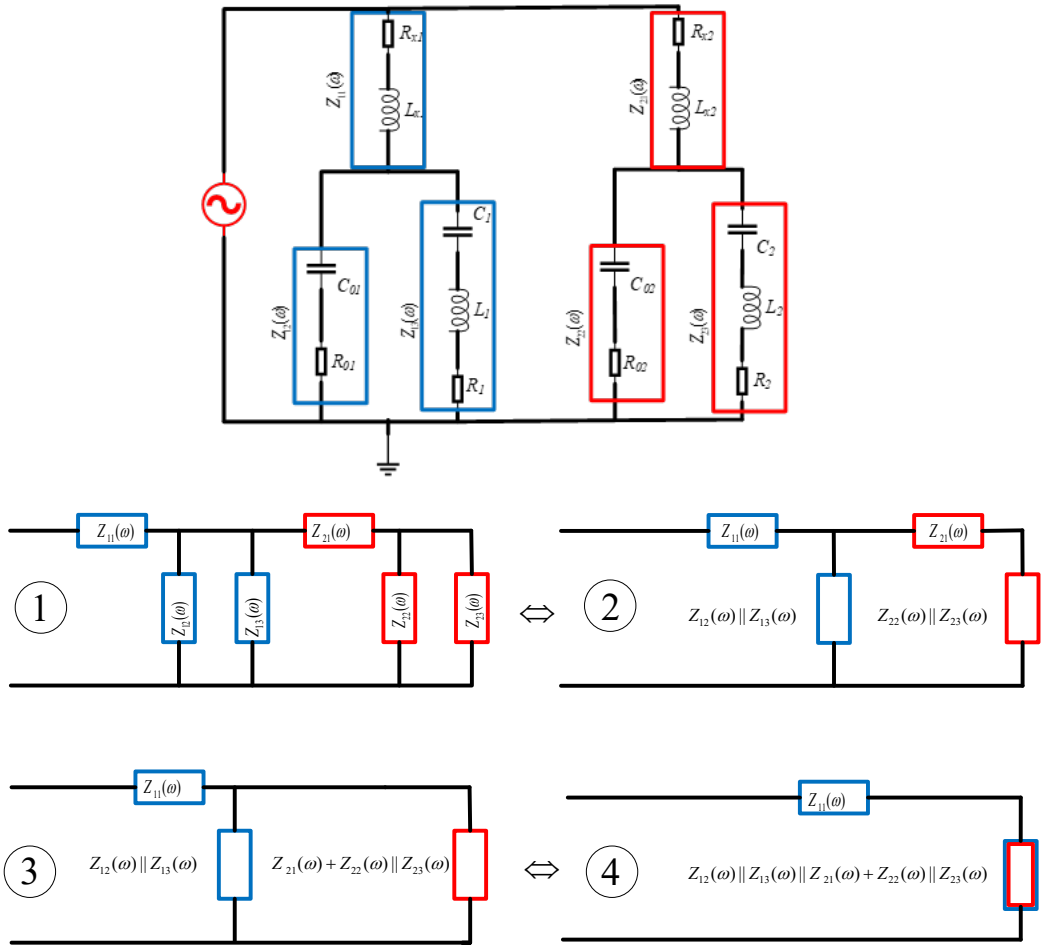

Figure 3. 8. Equivalent circuit for the updated version of mBVD. There are four steps to calculate the equivalent impedance. Blocks in blue correspond to the main resonance and the red ones are for the new resonator.

$$Zeq(\omega) = j\omega L_{x1} + R_{x1} + \left[\frac{1}{\left[\frac{1}{R_{01} + 1/j\omega C_{01}} + \frac{1}{R_1 + j(\omega L_1 - 1/\omega C_1)} \right]^{-1}} + \ldots + \frac{1}{j\omega L_{x2} + R_{x2} + \left[\frac{1}{R_{02} + 1/j\omega C_{02}} + \frac{1}{R_2 + j(\omega L_2 - 1/\omega C_2)} \right]^{-1}} \right]^{-1} \tag{3.2}$$

In the second method we use the S parameters. In our circuit we have only one RF port, which is called port 1. Hence we are able to compute the reflection coefficient S(1,1) between the port impedance and the network's input impedance (updated BVD circuit) by looking from the source end to the load end. Since we are able to compute S(1,1) we can compute the impedance at port 1, which is also the input impedance or the equivalent one. The expression to compute Z(ω) is shown in equation (3.3), where Z0 is a reference impedance of 50 Ω.

$$Z(1,1) = Z0\left(\frac{1+S(1,1)}{1-S(1,1)}\right) \tag{3.3}$$

3.3.2. Modified Mason's model, Updated Version

Figure 3.9 a) shows a block diagram of our updated version of the Mason's model. In this updated version we have used the same principle as in the updated mBVD. We assume that another resonator exists and is coupled capacitively to the main active resonator. The series resistance of each resonator is different due to the size of the effective area and the landing spot. Since we are interested in the electrical input impedance, we have connected the electric ports of each resonator in parallel as we can see in detail in Figure 3.9 b). The acoustic ports in the new resonator have the same material properties for each slab, only the active area is different. Summarizing, in this updated model we change R_x for both resonators and the effective area since those effects affect directly the series resonance frequency and quality factor.

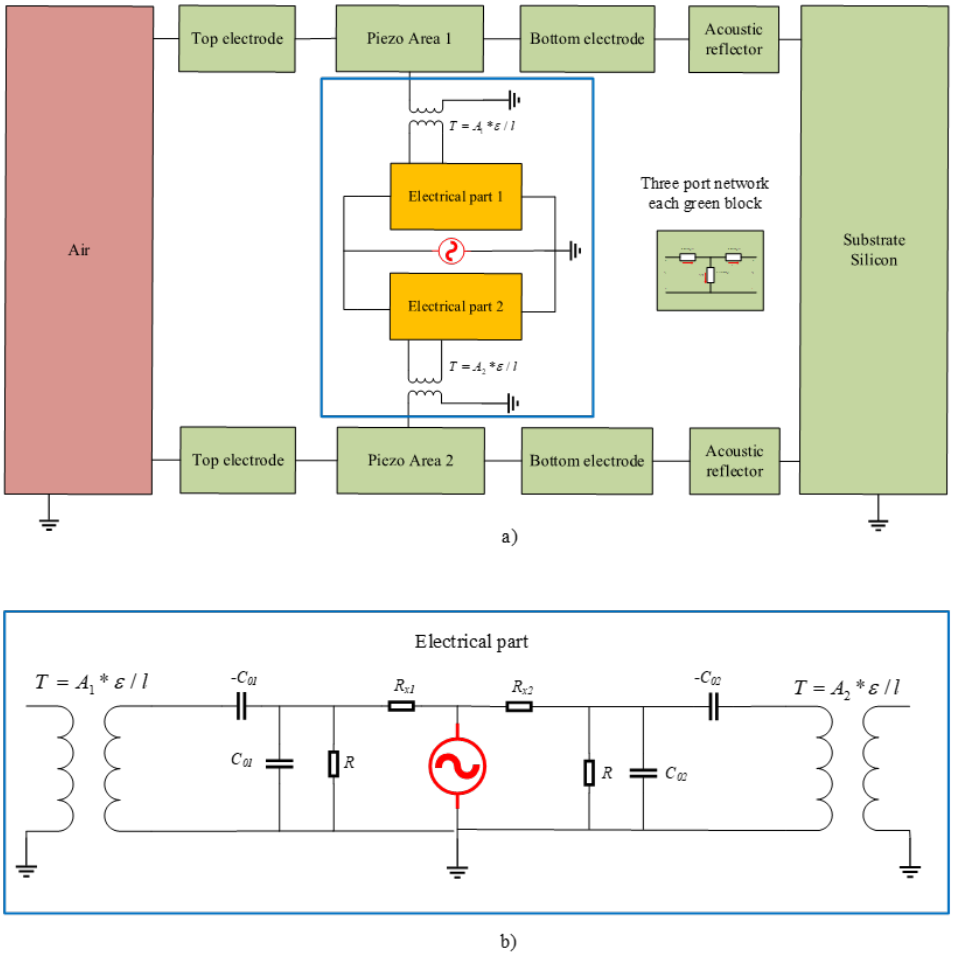

Figure 3. 9. Mason's block Model circuit for two multilayer resonators (SMRs). b) Electric ports of the piezoelectric material are connected in parallel. Each resonator has its own effective area and the thickness of the piezoelectric could be different due to roughness of the material.

3.3.2.1 Electrical Impedance

We have seen in Chapter 2 section 2.2.1 the derivation of the expression to compute the input impedance in terms of frequency $Z(\omega)$ with any loads in their acoustic ports. With this expression we are able to add more layers to the piezoelectric slab and compute its total impedance by connecting each film (i.e., electrodes in both sides of the piezoelectric, acoustic reflector and substrate) in cascade configuration. Each film is modelled in terms of the three ports transmission line model (see Figure 2.8.). In addition, since we have modelled our resonators in an RF simulator we are able to compute the impedance by means of the scattering parameters as for the mBVD model.

3.4. Modelling at Cryogenic and High Temperatures

Simulations at these extreme temperatures had to be carried out since we need acoustic devices in applications in harsh environments such as gas control in propulsion systems, petro-chemical industry, etc. Henceforth, we have added the temperature input to our updated two-branch models for a second bench of simulations. First, we have modelled a few resonators at high temperatures using the updated mBVD model; these simulations were made from room temperature 22°C up to 422°C. In these simulations we can observe how the temperature affects the performance of the resonators, mostly the series resonance frequency (f_s), quality factor and the effective electromechanical coupling coefficient ($keff^2$). Subsequently, we have simulated a series of resonators from cryogenic temperature up to high temperatures (-160°C to 422°C). In addition, we have carried out more simulations by means of the updated Mason's model, which is a complete model because it takes into account the physical properties of each material of the stack, including the substrate. With this model we can obtain the temperature dependence of the material properties. However, our principal objective is observing how the series and parallel resonance frequencies change according to temperatures variations. This is a key parameter since sensitivity of sensors is principally affected by shifts in the series resonance frequency. Both models predict with high accuracy this difference in frequency in terms of temperature changes.

3.5. Summary and conclusions

In this chapter, we have given a briefly explanation of the fabrication process of our SMRs and also the materials have been mentioned. The resonators are based on AlN, which is the most used piezoelectric for electroacoustic resonators in the last years. Our devices are designed to operate at 2.5GHz. In addition, it is important to mention that some cases the number of layers used for the acoustic reflector can vary. Then, we have explained two effects that occurs in our

SMRs duet to their geometry (shape and size of the active area) and the landing spot. Both phenomena are explained due to Ohmic losses and sheet resistance and also they have been included in our models. The updated models with the new effects are presented in this chapter, we have modified the mBVD and Mason ones since both are important tools for resonators designing from the electrical and acoustical points of view. Basically, the update consists in adding a new resonator that is coupled trough a capacitance. This new resonator affects the series resonance frequency of the main resonator. We have proved that our models predict very well this new resonance with high accuracy, by means of these new tools, we are able to avoid such effects. Finally in the section 3.4, we said that our models capable of adding the temperature as an input and see how affects the performance. Principally we want to check the change of the series resonance frequency according to the temperature since this parameter affect directly the sensitivity of gravimetric sensors in harsh environments. The whole results of these simulations will be treated in chapter 5.

Chapter 4

Proposed Methodology for the Characterization Process

This chapter starts describe the operation of the semi-automatic probe station as a unified system (section 4.1). This probe station allows to measure the Devices Under Test (DUTs) at low pressures such as 1^{-8} Torr and also at extreme temperatures (-160 up to 130°C). The pressure inside the chamber can reach levels of high vacuum (HV) due to a turbomolecular pump. In addition, the chuck-plate can be heated or cooled by means of resistors and a circuit of liquid Nitrogen, respectively. The whole system comprises multiple individual modules controlled by a Central Processing Unit (CPU). Our research group has developed a combination of commercial software provided by manufacturers and custom software tailored to our specific project requirements. In this section, we will delve into each module's capabilities and limitations. Moving on to section 4.2, we will outline the methodology employed to extract the S parameters at different temperatures. This section is subdivided into smaller parts (sub-sections 4.2.1 to 4.2.6), each containing a sub-methodology for different tasks. These sub-sections include: the setting up of the cryogenic chamber, alignment, landing and contact with the DUTs, and the calibration process of the Vector Network Analyzer (VNA). In addition, we have put especial attention in the equipment specialized for cryogenic temperatures (Z probe tips) since we need accuracy in our data from the measured resonators at these temperatures. Furthermore, we have included the temperature control section (4.1.7) because we need to find a good approximation of the real temperature in our DUTs in order to obtain better models.

This chapter holds great importance in this thesis, as it will involve the characterization of several SMRs at different temperatures and low pressure values. The characterization process presents various challenges such as alignment, landing and contacting the SMRs. There are technical and human-related drawbacks. Henceforth, to ensure repeatability and high accuracy in our RF characterization, we have developed a well-established protocol (methodology) that must be followed if we want good results. Furthermore, our methodology relies on a semi-automatic process that minimizes human intervention, thereby reducing errors.

4.1. Semiautomatic Probe Station Measurements Setup

To carry out measurements of our SMRs at different temperatures, we have used a complete modular system adapted for a specialized vacuum chamber, which is capable of working at cryogenic temperatures as low as -170°C (see Figure 4.2.). The entire system is almost a complete homemade adaptation for such purposes. This system is a modular entity, and throughout this chapter, we will describe each module individually to provide a comprehensive understanding of their functionalities, capabilities and limitations. In addition, we will provide an overview of the complete system operation. It is worth mentioning that our research group has dedicated considerable effort to overcome the challenges associated with this complex task, aiming to establish a semi-automatic probe station capable of conducting measurements at extreme temperatures. In Figure 4.1, we can observe a scheme of the semi-automatic probe station measurements with all its modules connected to a the Central Processing Unit (CPU), each module is able to operate as an Input and Output (I/O) port because they are able to send and receive data to the CPU. In the scheme we can see in Figure 4.1 a) each type of communication interface used to connect them to the CPU, such as Universal Serial Bus (USB), Recommended Standard 232 (RS232), Radio Frequency cables and Ethernet one. Furthermore, we have included in Figure 4.1 b) the air and nitrogen circuits used to make the vacuum and cold the samples, respectively.

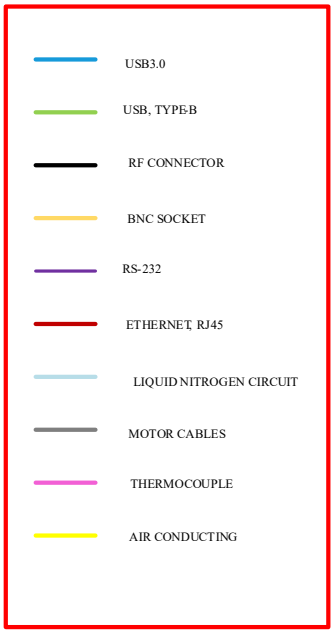

a)

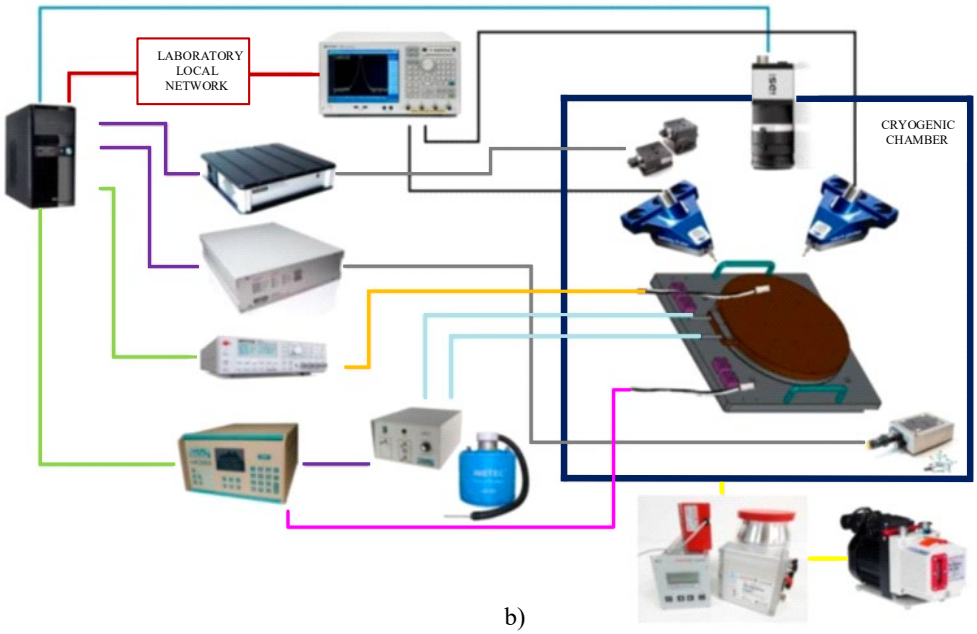

b)

Figure 4. 1. Schematic of the entire set up for the semi-automatic probe station measurements. a), shows the description of each communication protocol with their respective label in color and b) corresponds to the interconnection of the whole modules, the figure was taken and modified from [91].

4.1.1. Adapted Cryogenic Chamber

The model of the vacuum cryogenic chamber is BX2424S, which has the next dimensions: 24" x 24" x 24" width, depth and height respectively (60.96 x 60.96 x 60.96 cm) [92]. The

chamber is fabricated by stainless steel. In the front part of the chamber it is located a hinged aluminum door with an O-ring and dovetail groove sealed system, which likely ensures a tight and secure seal when the door is closed. The O-ring is based on Fluoroelastomer (FKM O-rings are able to operate at high temperatures and also are resistant to many chemical process). Furthermore, in the middle of the door there is a rectangular viewport (viewing area of 13.3 x 8.2 cm) that allows for observations or monitoring of the chamber's contents (DUTs) without having to open the door (vacuum case). Summarizing, the chamber is capable of being used in many applications at extreme temperatures, including thin film deposition, atmospheric testing, space simulation and clearly RF characterization.

Although the chamber was acquired without any modification, see Figure 4.2 a), we had to make some arrangements in order to connect our devices. Principally, we have made through-holes in its walls to pass in cables (see Figure 4.2 b). In addition, on top of the chamber there is a skylight for the optical system (camera) and a set of light-emitting diodes that illuminate the top of the samples inside the chamber. This is important since the alignment and landing on the samples is a complicated task and a good illumination is highly required (see Figure 4.2. c).

Figure 4. 2. Vacuum chamber made of aluminum with a specialized sealing system based on Fluoroelastomer O-rings. a), the chamber is stainless steel. Subsequently, b), c), d), and e) display the front, top, transverse, and back views, respectively.

On the back of the chamber there is a set of holes for dedicated purposes: the input/output to the cooling system (Liquid Nitrogen Circuit) and two outputs for the RF ports (see Fig. 4.2. e). The connectors that can be used at these ports are: SMA and K type, which are capable of working at frequencies up to 40 GHz. As we have mentioned, this chamber is able to perform measurements at different temperatures from -170°C up to 130°C. In addition, the pressure inside the chamber can be controlled, the system dedicated to carry out the vacuum is able to reach ultra-high vacuum values (10^{-7} to 10^{-12} Torr) using a turbo pump. Inside the chamber, there are the next modules: RF probe tips, RF K type connectors and cables, temperature sensors, motors to control the movement of the RF probes, camera, samples, and the chuck (see Figures 4.1b and 4.3). Finally, the chamber has a base with wheels to facilitate its movement in the laboratory making

it a versatile system. In the next sub-sections, we are going to describe each system inside the chamber.

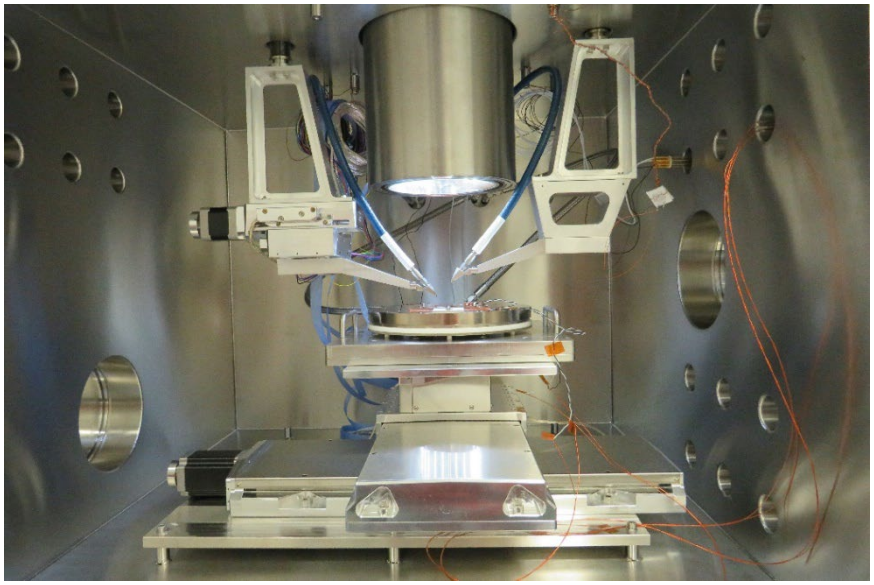

Figure 4. 3. Actual view of the modules inside the vacuum chamber. There are visible the RF probe tips, the chuck and the skylight for the optical system. In the walls, there are the through-holes made in order to cabling each module.

4.1.2. Camera and Optical System

The camera installed inside the vacuum chamber is the USB 3.0 interfaz uEye CP model. This camera is designed for industrial applications as is shown in [93]. It features an optical zoom precision lens with a magnification of 12.5x, manufactured by Edmund Optic. Additionally, it includes an auxiliary magnification lens of 0.5x, which allows for doubling the distance between the camera and the sample. This means that it is possible to work at a distance of 178 mm from the sample. However, we lose magnification capabilities although the system still has a 12.5x [94]. The position of the camera is in the three space coordinates X, Y, Z and it is controlled by means of three endless screws whom model is (A2506B-S2.5) based on stainless Aluminum (see Figure 4.4a) also magnifications and focusing can be made using a wheel mounted in the screw driver in the Z axis (see Figure 4.4b). The complete optical characteristics of the system are: Work distance of 178mm, magnification goes since 0.52 up to 6.5 and the field of view goes from 12.3 up to 0.98mm. By means of this optical system we can work with sufficient clarity and see elements with sizes of 10 μm.

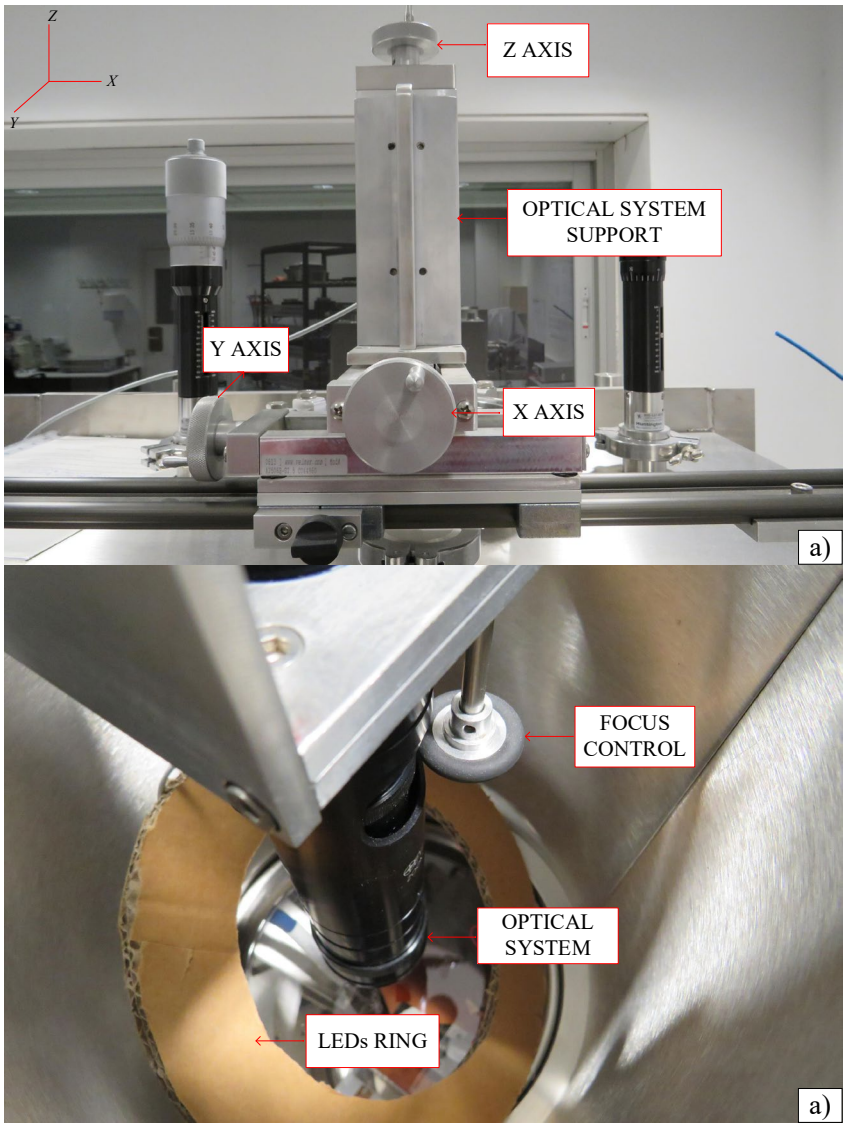

Figure 4. 4. Optical System. a) Shows us the support of the camera and optical lens, which is made of stainless steel (Aluminum). The support has three endless screws to control the position of the camera in the Cartesian system (X, Y, Z). In b), we can appreciate the optical system devices and also the wheel that controls magnification and focus of the camera. In addition, there is the ring that contains LEDs for an optimal illumination.

4.1.3. Round Wafer Chuck-Plate

This round chuck is designed for wafer handling by means of vacuum holes distributed in five concentric rings separated 40 mm. With this separation we could allocate samples of different sizes i.e., 200 mm (see Figure 4.5.). However, it is not able to hold samples in this way since the vaccuum circuit is not connecteted yet. Henceforth, in order to hold our samples we have used a special silver paste and kapton tape, both capable of working at high temperatures and low pressures. The diameter of the plate is around 210 mm. On the other hand, this plate is capable of working at low and high temperatures. In order to cool the chuck-plate a modular system of

refrigeration is used. This module uses liquid Nitrogen (LN_2). The system consists of one pump (LN2-P INSTEC), a cryogenic storage Dewar (LN2-D30), a lid with a stoppered port and a connecting tubing where the liquid nitrogen goes through a pipe to the chuck-plate to get cold it. On the other side, a serie of resistors heat the plate to reach high temperatures. The chuck presents a low and uniform gradient of temperature, which is around of ± 0.1°C per centimeter. Furthermore, to control the temperature on the chuck the mk200 module is used.

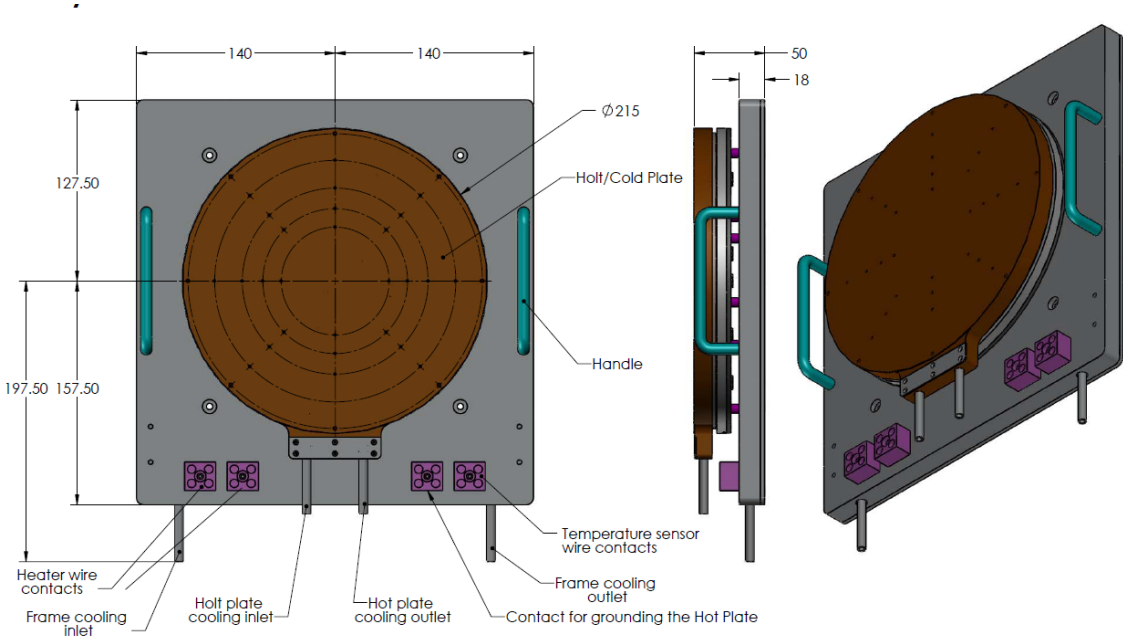

Figure 4. 5. Round 21 milimeters diameter hot/cold plate [95]. All values are given in mm.

4.1.4. RTD Temperature Sensors

The Resistance temperature detectors (RTDs) are temperature sensors that contain a resistor that changes its resistance value as the temperature changes. The most common RTD sensor is the Pt100 because they have shown excellent performance in industrial and laboratory applications. These devices have high accuracy, repeatability and stability. In addition, they are relatively immune to electrical noise and therefore well suited for temperature measurements in industrial environments (such gas detectors at harsh environments), especially around motors and generators.

We have used the HEL-700 model based on the Pt100 configuration, which can be suit to three or four wire configurations. Since resistance across the sensing element is considerably lower than other configurations such as Pt1000, unwanted resistance from lead wires and connectors

will have a larger distorting effect on overall resistance measurements, since it will comprise a greater percentage of the total resistance measured in the circuit. The lead wire resistance is measured and compensated by an instrument that accepts the 3 or 4 wire configurations. We have measured the temperature on three points distributed in the chuck. These spots are the following: under and onto the surface of the chuck and also onto the surface of a Beryllium Cupper sheet where the wafers are allocated.

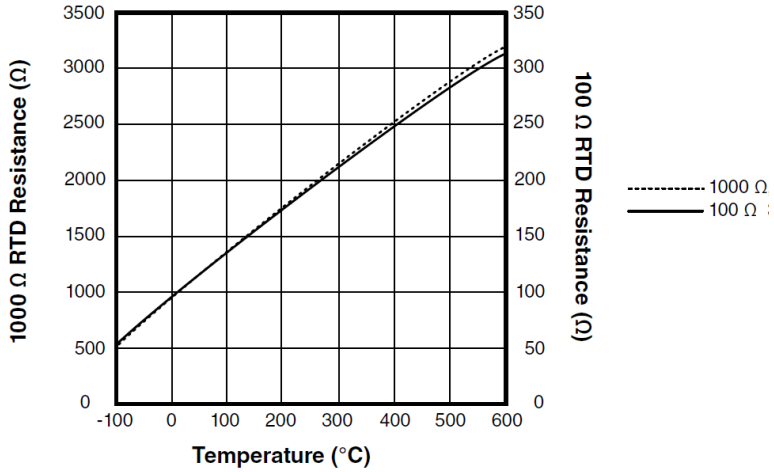

Figure 4. 6. The HEL 700 platinum temperature sensor behavior of the resistance versus temperature. The dash line corresponds to a RTD graph when its resistance at 0°C is 1000 ohms and the solid line when its resistance is 100 ohms at 0°C [96].

The behavior (tendency) of the RTD resistance with the temperature changes is a lineal response for the whole range of operation (-75 °C up to 540°C). This is shown in Figure 4.6, where the solid line corresponds to the RTD Pt100 configuration. Additionally, the RTD sensor is covered by a thin sheet of Indium because of its thermal conductivity (81.6 W/ K m). However, the melting temperature of the Indium is around of 156.6 °C, therefore the maximum temperature on the chuck plate has to be lower than this boundary in order to avoid malfunction problems.

4.1.5. HM8118 LCR-Bridge and HMC8012 Digital Multimeter

These devices are designed as general-purpose components. Both are well suited for our objectives since they are capable of measuring the instant resistance (R) under the two or four wire configuration technique [97], [98]. We have used the 4-wire configuration (see Figure 4.7.) since it takes into account the impedance of the cables and connectors, which allows internal de-embedding. In addition, this configuration has a good performance because of its high accuracy for small resistance values (i.e., lower than 0.1 Ω); an important characteristic since it improves the sensibility of the RTDs. Another important characteristic is the accuracy, which is excellent in both cases, with values of 0.05% and 0.015% for Hameg and the digital multimeter,

respectively. This values guarantee good temperature approximations. The LCR-Bridge and the digital multimeter are used to measure the instant resistance of the RTDs, which are set onto the BeCu plate and also onto the chuck (see Figure 4.9.). Afterwards, when resistance has been measured the temperature can be computed by means of equation (4.1). The computation is carried out by a function created in a programming language.

$$T = \frac{\left(-A + \sqrt{A^2 - 4B\frac{R_0 - R_t}{R_0}} \right)}{2B} \tag{4.1}$$

The value of each variable is shown below:

$A(°C^{-1}) = 3.908x10^{-3}$
$B(°C^{-2}) = -5.775x10^{-7}$
R_0 = Nominal Resistance at 0°C, (100 Ω)
T = Temperature (°C)
$R_t = R_0(1 + AT + BT^2)$

Finally, both devices are connected by means of USB protocol communication to the CPU, where the equivalent temperature in real time (*in situ*) is computed. It is important to notice that we can change the sampling time of the resistance measurements, hence we are capable of collecting more data in order to ensure high accuracy for the temperature computation.

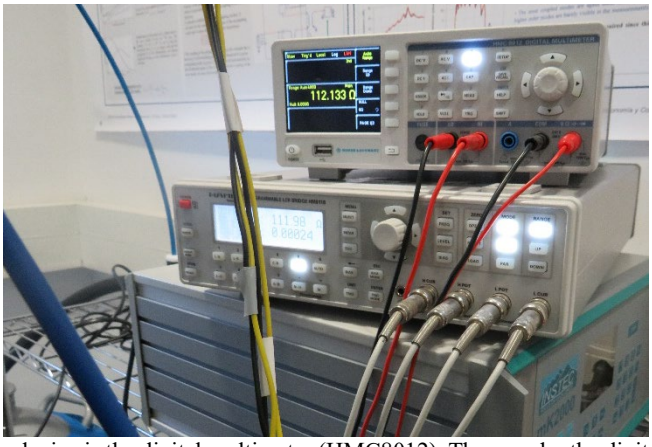

Figure 4. 7. The upper device is the digital multimeter (HMC8012). Then, under the digital multimeter is the LCR-Bridge (HM8118N). Both devices use the 4-wire technique in order to measure the instant resistance of the RTDs.

4.1.6. Instec mk200 Temperature Controller

The mk200 temperature controller is one of the most reliable systems in the market. One of the most important characteristics of this device is its resolution (± 0.01°C) if we use an RTD sensor (Pt100). This controller can reach a minimum heating and cooling rate of ± 0.1°C per hour. Since we needed temperature stability, the mk2000 controller was our best option. There are two

methods to control the temperature on the system. First, the manual option that consists in configuring the system using the buttons located in the front-panel of the controller (see Figure 4.8a). The second method is through its commercial software (see Figure 4.8b).

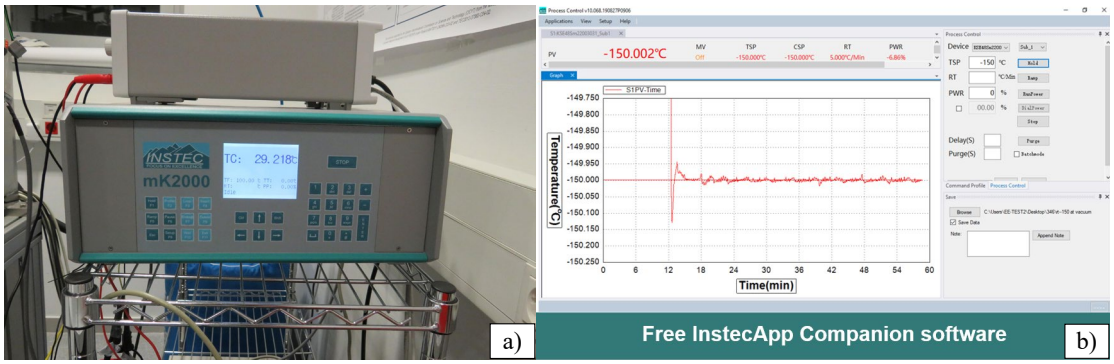

Figure 4. 8. In a) is the hardware of the mk200 instec and b) shows the software tool used to control the mk200 device.

4.1.7. Monitoring and Control of the Temperature

Since the samples (DUTs) are going to be set onto the chuck plate, we have put especial attention on this module. The reading and control of the temperature is a crucial step in the measurement process since changes in temperature affect the series resonance frequency of the SMRs. We have included three RTDs, which are identified as Hameg-Wafer (LCR-Bridge), a Multimeter-chuck (Digital Multimeter) and Instec chuck (mk200 Instec). These are set onto the BeCu sheet, onto the chuck and under the chuck, respectively. We have distributed the RTDs over the surface of the chuck to obtain reliable readings of the nominal resistance with respect to the temperature in the whole surface of the chuck plate.

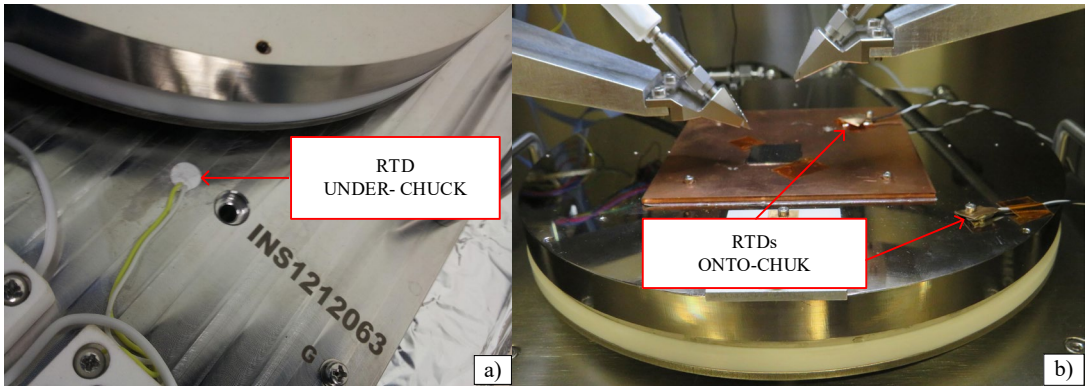

Figure 4. 9. In a) is shown the place where is collocated the RTD sensor that is readed by the INSTEC comtroller, this sensor is backside of the chuck. n in b) we can see both RTDs collocated onto the chuck and cupper plates respectively. In total there are three temperaure sensors.

The BeCu plate was mounted in order to assure good temperature conductivity between the chuck and the sample since they are fabricated of different materials, and they have different thermal expansion coefficients. Furthermore, between the BeCu film and the samples we added a high-performance silver paste, which has good thermal and electrical conductivity and ensures good heat propagation. This Ag paste is also good for very low temperatures, even at cryogenic ones. However, its performance at these temperatures depends on the joint design and the difference in the thermal expansion coefficient. Another important characteristic of this paste is its low sheet resistance, which can be modeled as Ohmic losses that could affect the quality factor. In addition, the RTD sensors are held by a screw and a thin sheet of Indium, which are necessary to obtain good thermal performance.

In Figures 4.10 and 4.11 we can observe the profile of temperatures variations with time for all RTDs. Figure 4.10 was taken only for increments of temperature; the heating process started at room temperature up to 100°C for 100 minutes. We can observe the difference between each RTD at certain set point temperatures (40, 80 and 100°C). The temperature computed is the one used in the modelling process for our SMRs because this difference of temperature is almost the same in a wide range. This last statement is also visible in Figure 4.11, which shows the profile on the BeCu plate, the blue one corresponds to the sensor allocated onto the chuck surface and the green one corresponds to the sensor set under the chuck surface.

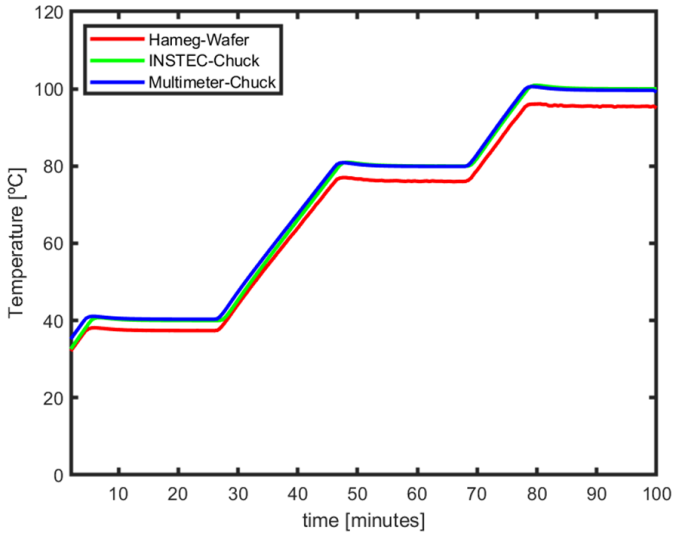

Figure 4. 10. Temperature profile recorded by all RTDs, ranging from room temperature up to 100°C, over a duration of 100 minutes.

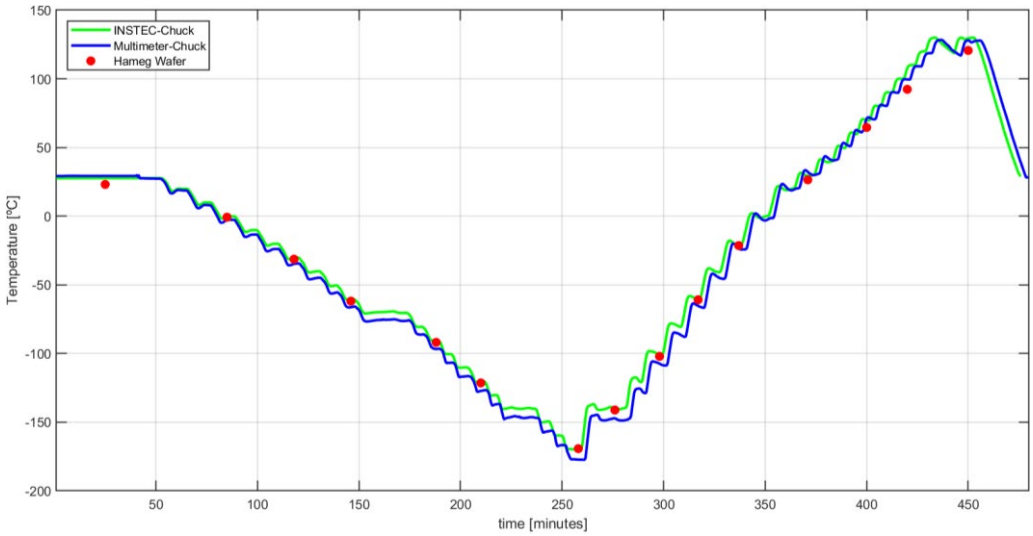

Figure 4. 11. Temperature profile recorded by all RTDs, ranging from -170°C up to 130°C, over a duration of 480 minutes.

4.1.8. Cryogenic |Z| Probe Tips

Inside the chamber there are two arms (post) for the RF probes. These arms are controlled by means of a motor that can move in the Cartesian system (X, Y, Z), although the second arm (port 2) does not have this system. On the other side, the RF probe tips chosen for our purposes were the |Z| probes configuration. These devices were considered because of their intrinsic characteristics and good performance showed at vacuum conditions and also at extreme temperatures such the cryogenic ones. The model used corresponds to the **SP-Z40-XV-GSG-150** one**.** This model operates from DC up to 40 GHz. The configuration of the probe is the ground-signal-ground (GSG) and the separation between each tip is 150µm (see Figure 4.12). Additionally, this model assures very high accuracy measurements with low contact resistance (*Rs*) and superior impedance control.

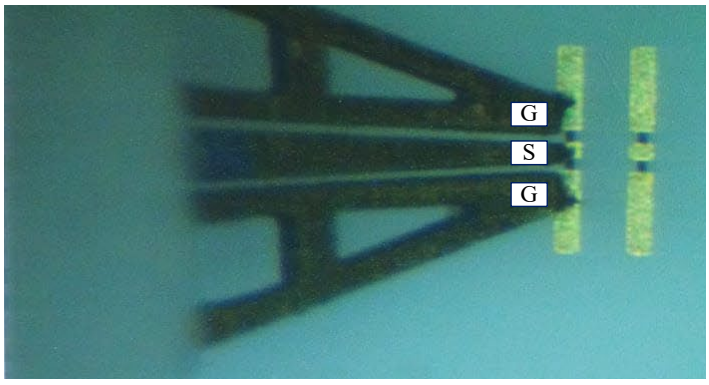

Figure 4. 12. RF Z vacuum and cryogenic probe tips (SP-Z40-XV-GSG-150). The configuration of these Z probe tips is the GSG. In the image there are making contact with a load of 50 Ω.

The RF signal makes only one transition to the coplanar contact structure within the shielded, air-isolated probe body, maintaining signal integrity at temperatures as low as -269.15°C (4K), or as high as 300°C. This capability makes the |Z| probes suitable for harsh test environments (cryogenic and high temperature ones). Another important characteristic of these probe tips is that each tip moves independently, allowing us to contact on three-dimensional structures and wafers with pad-height deviation up to 50 µm. Summarizing, these probes have good durability, flexibility and good RF performance. In Figure 4.13 we can observe the top view of two types of Z probe tips with the GSG configuration. In Figure 4.13 a) it is shown the classic configuration, then in b), we can see the 1MX technology, which ensures low insertion losses, high isolation and accurate measurements. We use the 1MX configuration.

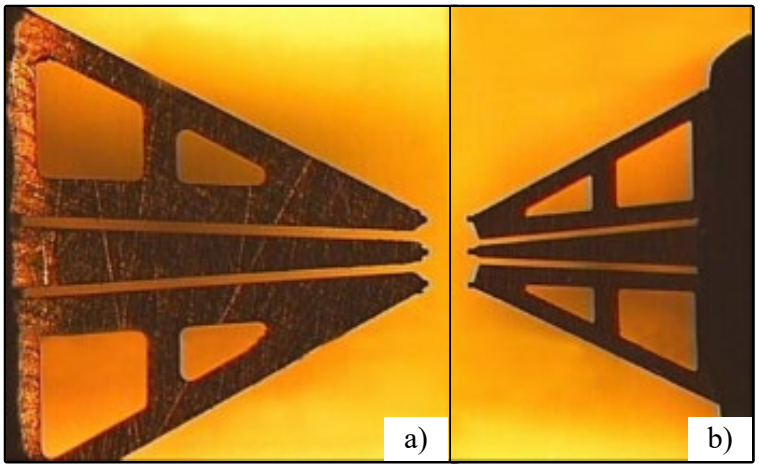

Figure 4. 13. RF Z vacuum and cryogenic probe tips. There is the classic Z probes a) and b) corresponds to the 1MX technology. [99].

4.1.9. High Resolution Positioning Controllers

The high resolution positioning controllers used in order to control the movement of the chuck and the Z probe tips (port 1) throughout the servomotors are: the series SMC Corvus and the SMC Corvus eco version. These controllers have excellent capabilities to industrial and precision applications. One important characteristic of these systems is the velocity-range, which is lower than 0.1 µm/s with 1 mm of pitch. These characteristics are pivotal to not damage the probe tips and samples. In addition, they have the option to operate in two (X, Y) or three (X, Y, Z) axes. In the case of the chuck plate, we have chosen the controller for the three axes since it offers a great advantage when we have to align the samples. Then, for Port 1, we have the two axes (X, Y) version. We use this controller only for positioning purposes of the probe tips (see Figure 4.14). The resolution of this controller reaches the nanometer range. The interface communication

interface used is the RS-232, which is connected to the CPU throughout a virtual COM port. Finally, the software used is the Venus-, which was provided by the manufacturer.

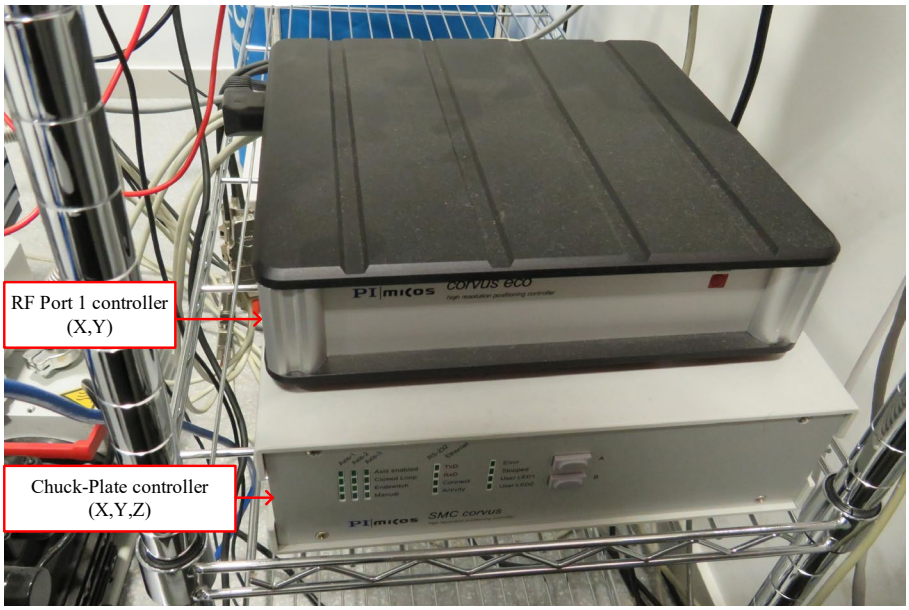

Figure 4. 14. Positioning controllers (Corvus and Corvus eco) the chuck plate and the RF probe tips (port 1), respectively. The probe tips of the port 1 only can move in the (X, Y) direction while the chuck-plate has three grades of movement (X, Y ,Z).

4.1.10. High and Ultra High Vacuum Equipment

The DuoLine 5M pump is a dual-stage rotary vane pump that ensures reliable operation for various applications, including industrial requirements and scientific applications in laboratory conditions. This pump can achieve vacuum levels of approximately 10^{-4} Torr, which falls within the low to medium range of vacuum (see Figure 4.15a). It is designed to provide long-term operation, which is crucial as many of our measurements require a significant amount of time to complete them. To enhance its performance, the DuoLine 5M pump is backed up by a turbomolecular pump (Pfeiffer TC-400), as shown in Figure 4.15b. The turbomolecular pump is regularly employed to attain stable pressure values, specifically for achieving High Vacuum (HV) and Ultra-High Vacuum (UHV) conditions. HV pressure ranges from 10^{-3} to 10^{-8} mbar, while UHV ranges from 10^{-8} to 10^{-12} Torr [100]. These pressure ranges are commonly utilized in simulating space conditions and conducting cryogenic research. Although reaching such values is not crucial for our work, the use of a turbomolecular pump ensures reliable pressure control. It is important to note that the DuoLine 5M pump offers additional advantages suitable for various industrial and scientific applications. These advantages include high pumping speed, low noise operation, and robust construction. On the other hand, to display the pressure value, we have used two modules. The first module (Pfeiffer gauge) monitors the pressure inside the vacuum chamber

(see Figure 4.12d) in the full-range from 10^{1} up to 10^{-10} Torr. Afterwards, to see these values we have mounted the Pfeiffer DCU display, which is also capable to control the turbomolecular pump (see Figure 4.15c).

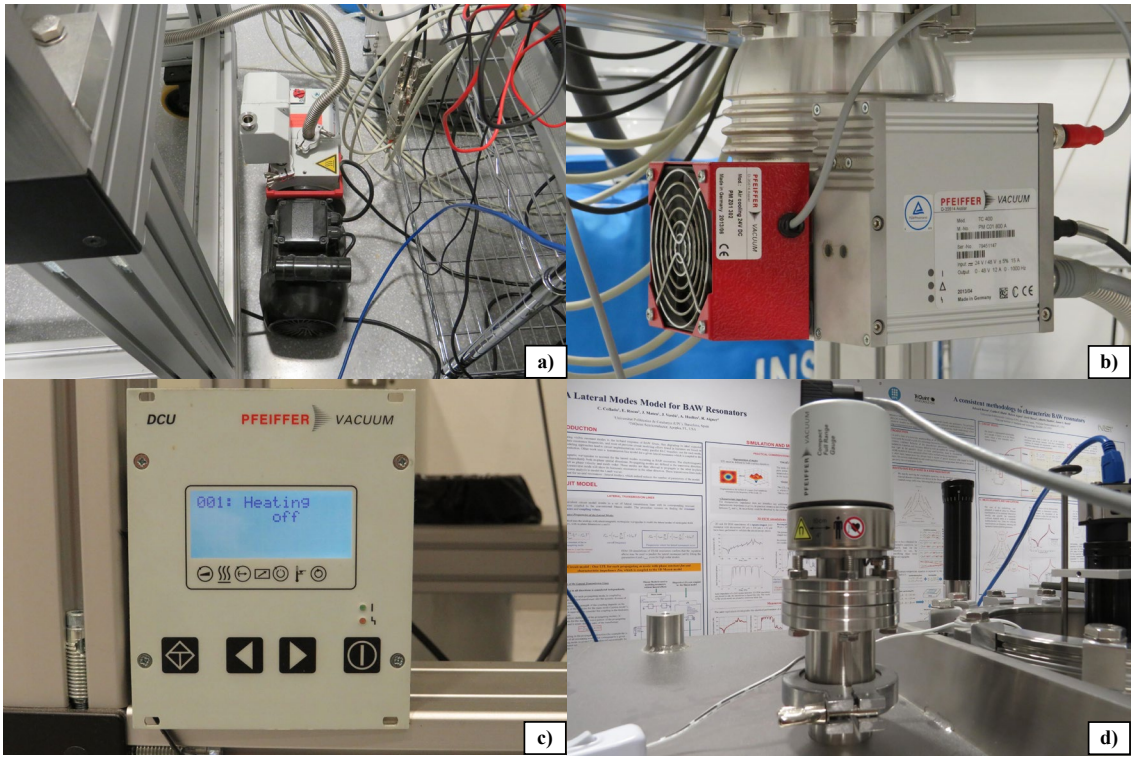

Figure 4. 15. Vacuum System. a) DuoLine 5M pump, b) TC-400 turbomolecular pump, c) turbomolecular controller and d) is the compact full range gauge.

4.1.11. Vector Network Analyzer E5071C

The Vector Network Analyzer (VNA) E5071C is a sophisticated and versatile instrument used in the field of RF and microwave engineering. It is designed for precise and accurate characterization and measurement of electrical networks and RF devices. The VNA offers a wide frequency range, typically spanning from a few kilohertz up to 20 GHz. This broadband frequency coverage allows us to analyze and evaluate devices and circuits operating in various frequency bands or wideband devices such as SMRs. One of the key features of this model is its ability to measure and display both magnitude and phase information of complex electrical quantities such as the electrical impedance (Z). This capability is essential for analyzing the behavior of components such as amplifiers, filters, antennas, transmission lines and SMRs. The E5071C VNA offers multiple measurement modes, including transmission, reflection, and S parameter measurements. These measurement modes allow users to investigate a wide range of characteristics, such as insertion loss, return loss, group delay, and scattering parameters. The S parameters are particularly valuable as they describe the signal behavior at different ports of a

device. In our case, we are going to extract the S parameters of SMRs at different temperatures. In addition to its comprehensive measurement capabilities, the E5071C VNA provides advanced calibration techniques to ensure accurate and reliable results. Calibration standards, such as open, short, and load, are used to establish a reference plane and remove systematic errors caused by cables and connectors. This calibration process enhances the measurement accuracy and enables precise characterization of devices with high precision. The VNA is equipped with a user-friendly interface and powerful software, enabling users to control the instrument, visualize measurement results, and perform complex analysis and data processing. However, we control this device with our specific programing routines.

4.2. Methodology Used to Extract the S parameters at Different Temperatures

The procedure used to carry out our measurements (extract the S parameters) in the semi-automatic probe tips system at different temperatures is described step by step in the next sub-sections.

4.2.1. Physical and Virtual Connections

The first step of our methodology is a simple one, but not less important, and consists in checking all the physical connections of our equipment (see Figure 4.1). In addition, we have to check if all of them are detected by the CPU. To accomplish this task, we have to carry out two or three tests to verify it. Once we are sure about this step, we are able to move to the next one.

4.2.2. Setting of the Calibration Kit, Z Probe Tips, and the Sample

To accomplish these tasks we have to make some considerations. The first one is choosing the correct probe tips and calibration kit configuration; they have to be compatible between each other (in the data sheet of the probe tips we can find this information) [99]. Furthermore, both devices have to correspond to the configuration of the DUTs (i.e., GSG with a 150 μm pitch). At this point we are able to set them inside the vacuum chamber at their corresponding locations (see Figure 4.16a). Cleaning of both devices can be made either with dry air or by means of the special kit (Probe polish, K25-39045); the methodology that can be used is explained in [101]. In order to set the Z probe tips we need to be very careful since this technology is extremely small, fragile and expensive. Once mounted, we need to position the arm parallel to the sample surface. Fortunately, since our SMRs have only one port we can use only (Port 1).

Then, we can set the kit calibration onto the surface of the chuck-plate. Since we are not capable of making vacuum throughout the holes dedicated in the chuck, we had to set up a dedicated base onto the surface chuck in order to hold the calibration kit. In addition, we have used two sheets of Indium to hold the calibration kit at two borders (see Figure 4.16b). Finally, we can set the sample (DUTs) onto the BeCu plate by means of the Ag paste. This last step is important because the sample is attached to the Ag paste and is hard to remove it. Since our chuck plate is not able to rotate, we have to align the SMRs with the probe tips. If the sample or the kit calibration are not well positioned (see Figure 4.17a) we have to rotate them to correct the shift angle (λ). We can observe when the SMR is well aligned in Figure 4.17b). Finally, in order to correct this shift angle, the software offers us useful tools such as guidelines and marks.

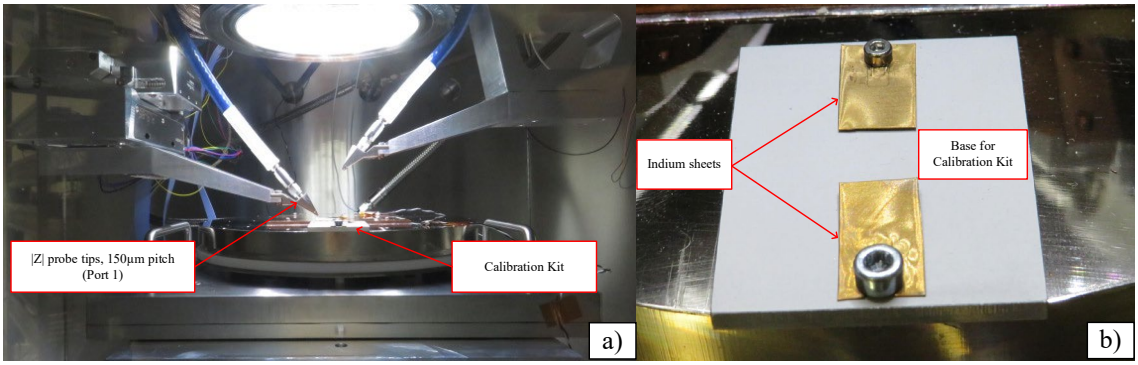

Figure 4. 16. In this picture we can see the arm dedicated for the Z probe tips and also we can see the base for the calibration Kit.

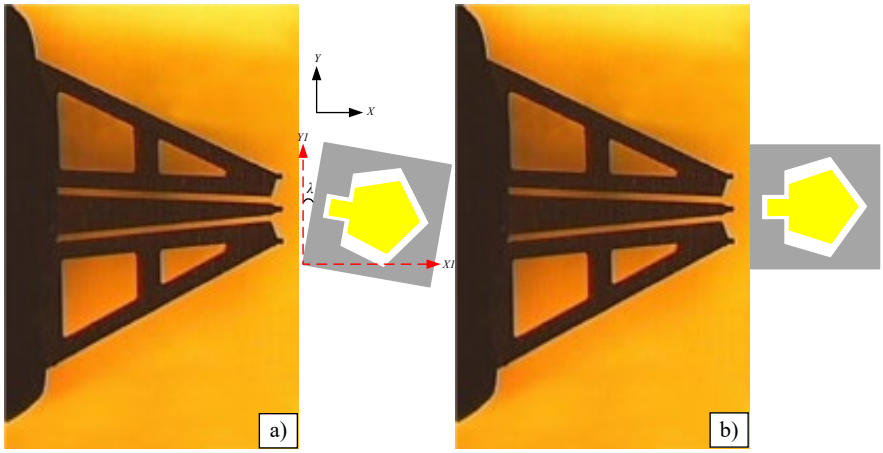

Figure 4. 17. a) DUT with a sift angle (λ) for this case the landing is not possible until we correct λ to 0°, then in b) we observe that λ is corrected and the landing process is possible.

4.2.3. Vacuum Process

Before the vacuum process the high performance Ag (silver) paste has to be cured at 93°C for two hours in order to achieve the high conductivity and strong bond to the sample and the BeCu sheet [102]. To achieve the target temperature during this time, we have created a script in the instec controller with its own syntax. This is an easy task since we can use the controller of the

temperature software. Afterwards, we can perform the vacuum step. First, we vacuum using the normal pump for almost 2 hours, then we have to power on the turbomolecular pump in order to reach high vacuum values. The second step takes a few hours, even a complete day.

4.2.4. Alignment and Contact Samples, Our Proposed Methodology

In this section we present our methodology to align and contact the calibration kit. This method is also valid for our SMRs.

1- Lower the probe tips using the positioning arm until its limit (45 mm upper the chuck-plate), do not move the arm in the X or Y direction. The movement of this arm is limited to the Z direction (manually). The position of the tips must be parallel to the wafer surface.

2- Move the chuck-plate in (X, Y, Z) directions until we can locate the probe tips by means of the optical system. When we have found them, we have to focus the probe tips in order to find the SMR in the sample (at this point the SMR is not focused yet).

3- Once the DUTs is located, we have to focus both the probe tips and DUT within the same plane (by means of moving the chuck-plate). When both devices are focused (see Figure 4.20a), we are able to make the landing process.

4- When we are completely sure that the probe tips and the SMRs are well aligned and focused, we can make contact between each other. This step can be reached raising the chuck-plate (movement in Z direction). We have to be cautious with this step because if we overpass the skating and overtravel values recommended by the fabricant of the probe tips, 100µm and 5-30µm, respectively, we can damage either the SMR's pads or the probe tips. At this point we recommend move the chuck-plate with steps of micrometers (i.e., 10 µm).

4.2.5. Calibration process of the VNA, our methodology

Once made the landing step and contacted the SMRs, we can extract the S parameters. However, we have to calibrate the VNA before any measurement. This step is required because it compensates for the inaccuracies or errors introduced by the VNA and the measurement setup (systematic errors). There are many factors that can cause these errors or inaccuracies, such as cable loss or connector imperfections, component or impedance mismatches in the measurement setup. Calibration corrects for these errors by establishing a reference plane that serves as a baseline for accurate measurements. There are many types of calibration methods that are commonly used for VNA, such as Short-Open-Load-Thru (SOLT), Thru-Reflect-Line (TRL) and Line-Reflect-Match (LRM). Each method uses a different set of calibration standards and techniques to achieve the desired level of accuracy. We have used the full one port calibration

that uses the standards (SOL). This calibration provides high accuracy. The calibration methodology that we have followed (step by step) is shown in the flowchart drawn in Figure 4.18.

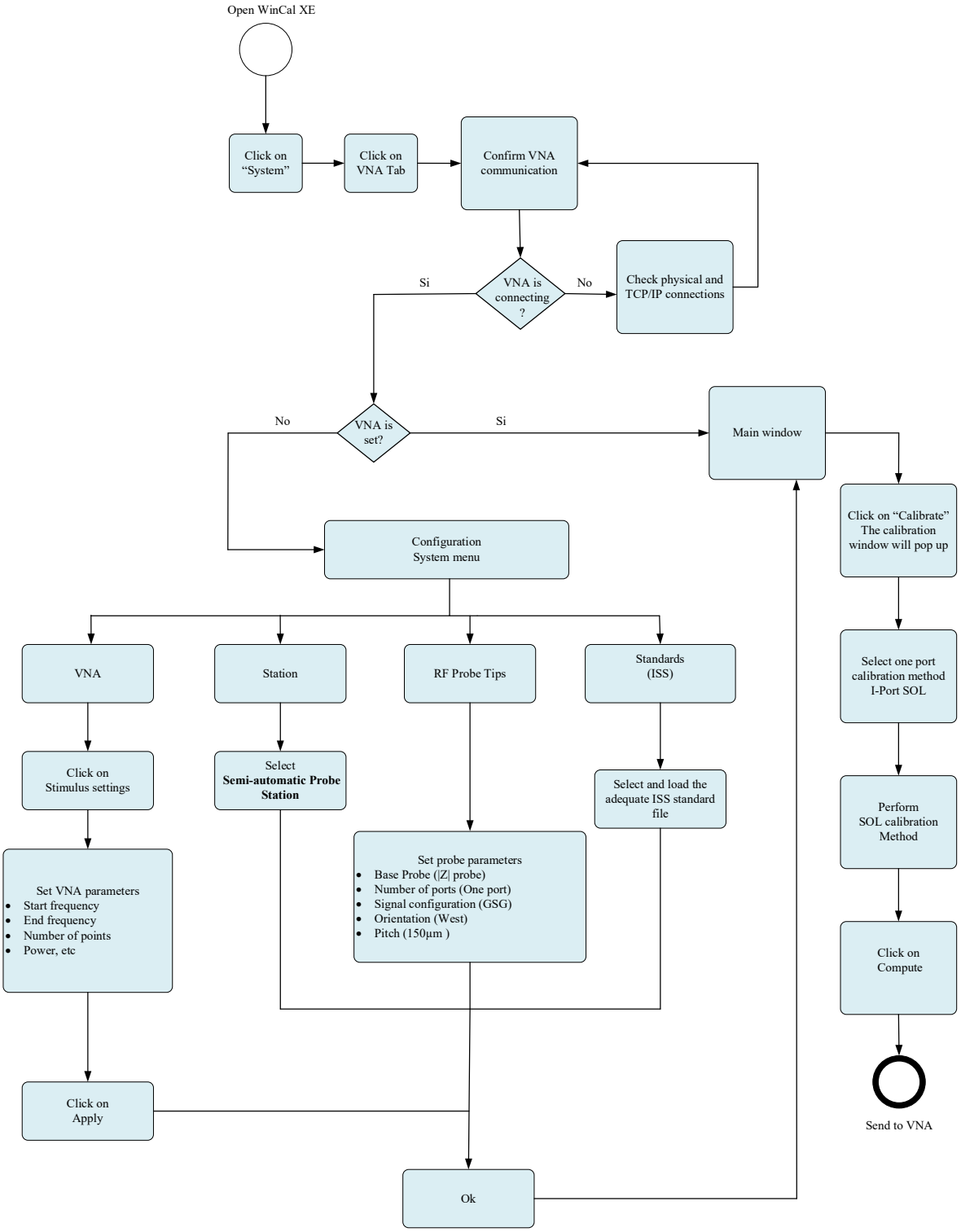

Figure 4. 18. Flowchart of the calibration process of the VNA. We have used the one port method using the SOL standards.

On the other hand, there are other two causes that can introduce inaccuracies in measurements. These are due to drift and random errors. Both vary in time and are not reproducible and predictable. The principal causes of these errors are due to environment changes (temperature changes), test setup (instrument noise, measurement practices, cables and connectors). Bothe types of errors cannot be removed due to their nature, but they can be minimized. In our case, temperature and pressure inside the chamber changes. We could correct these errors by performing a new calibration at each temperature. However, we have demonstrated that it is not necessary since the calibration remains almost the same at different temperatures and also at low pressure for all SOL standards (see Figure 4.19a). Henceforth, we have performed only one calibration at room temperature and vacuum condition (1^{-7} Torr). We can observe in Figure 4.19b) a close-up for the load standard (L) within a scale of 0.05 circle in the Smith chart. The reflection coefficient S(1,1) at three different temperatures, -140, 25 and 130°C, respectively is not changing substantially. Further, for our calibration wideband S(1,1) values are under -40 dB, which assures us reliable measurements since it is below of the -10dB standard.

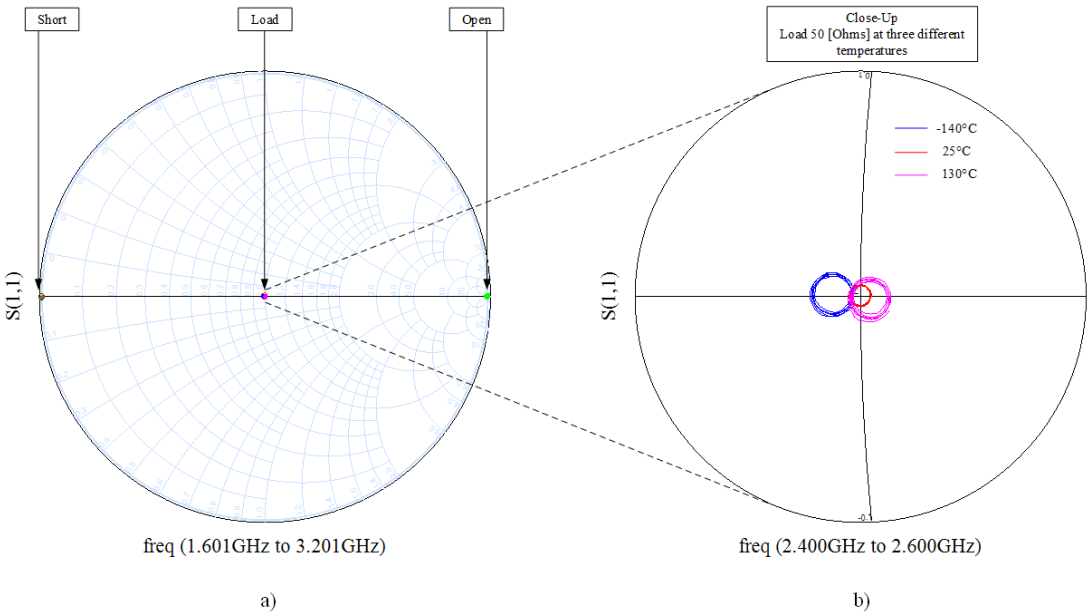

Figure 4. 19. S(1,1) in Smith Chart, where a) shows circles for calibration micro-strips (Impedance Standard Substrate); short, load and open at three different temperatures since 1.601 up to 3.201GHz. In addition, b) is a close-up for the load strip only since 2.40 GHz up 2.60 GHz. The blue circles correspond to the lowest temperature-140°C, red circles are for 25°C and the magenta ones correspond for 130°C.

4.2.6. DUTs and Measurements

Once the calibration process is performed, we can carry out the measurements of DUTs. First, we can make the landing following the steps mentioned in (section 4.2.4). Afterwards, we can make measurements at different temperatures. For instance, if we want to perform measurements at low temperatures, we have to decrease the temperature in the chuck-plate by means of the

temperature controller (mk200). Then, we can carry out measurements at each temperature. The extraction of the S(1,1) must be when the profile temperature is almost flat (see Figure 4.10). The process of extracting the S parameters is governed by the routines created in a programming language. This program is mostly divided in five blocks. These blocks are:

1- Connecting the VNA by means of TCP/IP communication protocol.
2- Define global variables, such as frequency operation bandwidth, intrinsic impedance, directories, etc.
3- Load the calibration file and set the VNA parameters such as trigger, display output, etc.
4- Extract the S parameters by means of specific functions.
5- Save the data in SP1 format in order to process the data lately.

4.3. Summary and Conclusions

In conclusion, in this this chapter we have provided a comprehensive overview of the functioning and capabilities of a semi-automatic probe station measurements as a unified system. We have explored its ability to measure DUTs at low pressures and extreme temperatures, thanks to features such as high vacuum levels and temperature control modules. We have also highlighted the importance of the each individual module within the system, which is controlled by a CPU. The control software is a combination of both commercial and software developed by our research group. By delving into each module's capabilities and limitations, we have gained a deeper understanding of their role in the overall measurement system and also the measurement process. On the other hand, we have outlined the methodology employed to extract the S parameters at different temperatures (-170 to 130°C). The subdivision of this methodology into smaller parts allowed us to address critical tasks such as cryogenic chamber setup, alignment, landing, contact with the DUTs, and the calibration process of the VNA. We also underscored the significance of equipment specialized for cryogenic temperatures since accuracy is crucial parameter in obtaining reliable data.

Additionally, we spotlighted the inclusion of the temperature control section, which explains a better understanding of temperature changes within the DUTs, this will enhances the accuracy and reliability of our modelling. In the end of the chapter, we have explained that the characterization process of many SMRs at different temperatures and low pressure values is a challenging task. Henceforth, in order to ensure repeatability and achieve high accuracy data, the implementation of a well-established protocol is essential. Our methodology employs a semi-automatic process that effectively minimizes human intervention and mitigates errors, resulting in reliable and precise measurements.

Chapter 5

Simulations, Measurements and Results

In this chapter we present simulated data for a variety of SMRs with different active areas at different temperatures (from -160 to 422°C). The simulations were performed using our updated models, which are based on one-dimensional analysis and the electric equivalent circuit (the Mason and mBVD models, respectively). We also present experimental data from our fabricated SMRs to demonstrate the accuracy of our models.

First, we have modeled resonators at room temperature at an operating frequency of 2.5GHz. The reason of this study is to observe how the geometry and topology of the resonators affect their performance, specially the size of the active area. In addition, we have studied the effect of changing the location where we land the probe tips on the active area of the resonators in order to extract the electrical parameters. This study is going to be called the probing spot effect. We have introduced both effects in Chapter 3, Section 3.2.1, and also updated our models in order to include them in Section 3.3. We briefly explain these effects again in this Chapter (sub-sections 5.1.1 and 5.1.2) for a better understanding of our experiments in sub-sections 5.1.3. Both effects directly affect the main series resonance frequency because of Ohmic losses. This resulted in a new resonator that is modelled with a new parallel branch connected in parallel to the main one for both models. Models have shown high accuracy compared to our extracted data from fabricated SMRs (sub-section 5.1.3). Finally, in sub-section 5.1.5, we present the most relevant output parameters that measure the performance of the resonators such: the quality factor and the effective piezoelectric coupling coefficient, series resonance and parallel one. We summarize them in Table 5.4.

In the second part of this chapter, we have carried out the temperature dependence analysis for high temperatures. This consists in modelling resonators by means of our updated models and the temperature dependence equations (see section 5.2.2). This analysis was carried out from 22°C up to 422°C. In addition, to prove the accuracy of our models, we present results from the extracted data of our fabricated SMRs. The devices used for this section are described in section (5.2.1). Then, in section 5.2.3, we describe the setup measurement and also the methodology used to carry out the extraction of the data at high temperatures. The last point reviewed in this section is the accuracy of the model with respect to the data of our SMRs. We present results for the most

important performance parameters of the resonators as a function of temperature. Such parameters are: both resonance frequencies (f_s and f_p), the effective electroacoustic coupling coefficient (k_{eff}^2) and the quality factor (Q). Furthermore, we also introduce the temperature coefficient of frequency (TCF). This parameter measures the ratio of change of the resonance frequency respect to changes in temperature.

Finally, we present the results for simulations and extracted data for the analysis at very low temperatures. The model used to carry out such simulations is the same for the high temperature analysis. However, simulations below -120°C were not carried out since at these temperatures results present nonlinearities. Furthermore, at these temperatures, the typical applications are out of our scope of investigation. In the next sub-section (5.3.2), we give a briefly explanation of the setup at cryogenic measurements and the methodology that we have used to measure the resonators. In sub-section 5.3.3 we present both, simulations and extracted data results with respect to temperature. We have computed the TCF, k_{eff}^2 and quality factor at very low temperatures. Furthermore, we have represented results for both analysis at low and high temperatures, respectively. This last experiment is carried out in order to get a wideband response with respect to the temperature.

5.1. Active Area and Probing Spot Effects

Thin film SMRs should have high quality factors (Q) and spurious free resonances. This second requirement is crucial as the presence of spurious resonances can distort their behavior in sensing applications (i.e., sensitivity). Previous works have shown that the device size and shape strongly influence the quality factor Q [16]. Other studies have revealed that the conductivity of the electrode's materials can lead to high Ohmic losses and the presence of a spurious mode at series resonance [18]. However, this effect has been less studied and only considered in finite element modelling. In this section, we analyze the effect of the SMR's active area and the probing spot by modelling them through our updated mBVD and Mason's models. Mason's model has been less studied when considering spurious resonances. Compared to other models, where spurious resonances are typically introduced by parallel motional branches, we have found that, depending on the electrical probing spot on the top electrode and having a capacitive coupling to the bottom electrode, a complete parallel resonator including different series resistance and series inductance (R_{x2} and L_{x2}) is needed.

5.1.1. How the Size of the Active Area Affects the SMR Performance ?

This section pays special attention to the active area of the resonators. Its variation could affect the performance of the resonators. For instance, if the series resistance increases at the electrodes, the quality factor decreases. In order to simulate the variation of the active area, we have considered three different sizes of our SMRs, which are divided in: small, medium and large, each size with a different series resistance (R_{x1}). The values of each active area are shown in Table 5.1. These areas correspond to our fabricated SMRs geometries. All values are in square micrometers (μm^2). In addition, we have divided the total active area of the resonators in two parts: pad (RF input port) and pentagon shape (active area), these geometries where defined in Chapter 3, section 3.2. The area of the pad is the same for all SMRs, although the shape can be different, we have designed different forms such as circles, ellipses and romboids. We said that Ohmic losses due to the contact between the RF probe tips and the top electrode affects the performance of the resonator, especially the series resonance frequency (f_s), therby the quality factor (Q). We can see an example of this effect if we look carefully at the curves plotted in Figure 5.1.

First, we can observe a bump in the smith chart inside the black solid squeare. This effect aparently affects particularly the series resoance frequency (f_s). In addition, we can notice that this effect is more evident for resonators with bigger active areas (see Figure 5.1b, magenta curve). We need the values for f_s in order to demosntrate that this effect disturbs the performance of our SMRs. In Table 5.2, we can see the values of the f_s. We have noticed that the f_s decreases as the active area increases. Finally, Figure 5.1 c) and d) show the quality factor (Q) and phase of the impedance, respectively. It is clear how this effect also affects the behavior of the resonator.

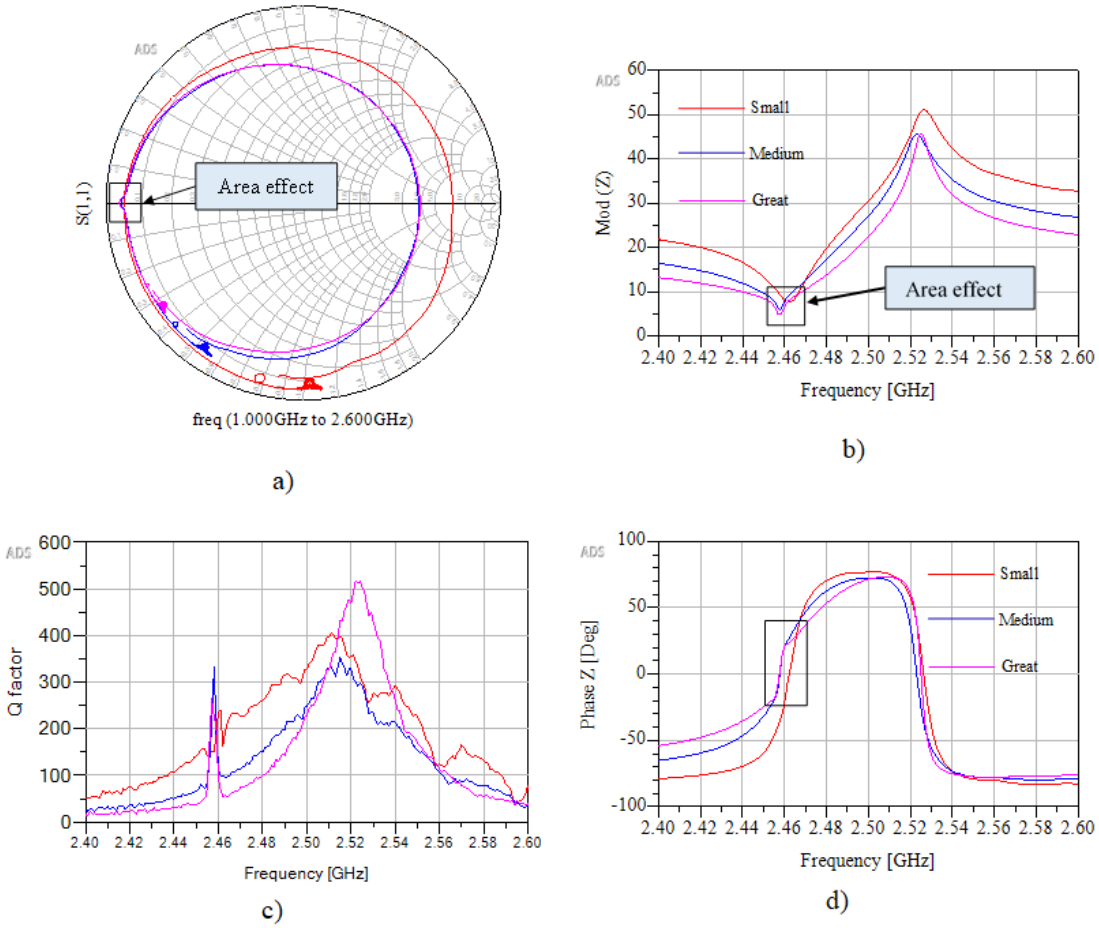

Figure 5. 1. Curves for three different SMRs that correspond to the small, medium and great active area, respectively. In (a) there is the S (1, 1) in the Smith chart format, then (b) corresponds to the electric input impedance Z [dBΩ], the series resonance frequency for each case corresponds to 2.462, 2.458 and 2.457 GHz, respectively. In (c) we have the Quality factor (Q). And (d) Corresponds to the phase of the electric impedance. The red curves correspond to the small resonator, the blue one to the medium and the magenta is for the greatest resonator. All curves are plotted as a function of frequency.

Table 5. 1. Size of the active areas of three resonators: great, medium and small one (1A, 1B, and 1D, respectively). All values are in square micrometers (µm2).

Device	**Size**	**Pent_area [µm^2]**	**Pad_area [µm^2]**	**Total_area [µm^2]**
(1A)	Great	95,105	9,600	104,705
(1B)	Medium	53,496	9,600	63,093
(1D)	Small	21,912	9,600	31,512

Table 5. 2. Series resonance frequencies (f_s) values for three different resonators (1A, 1B, and 1D, respectively).

Size-Area	f_s **[GHz]**
Small	2.462
Medium	2.458
Great	2.457

5.1.2. Pad, Corner and Center Spots

As mentioned, if we increase the size of the active area of the resonator the Ohmic losses increases and generate an extra resonance. However, this new resonance is not generated only by this effect. The new resonators are also dependent on where we measure the DUTs, either in the pentagon or the pad active area. These spots are reffered as the pad, corner and center (probing spot). The new resonator is capacitevly coupled through a capacitance (C_{02}), (see Figure 3.5). This is due to the path that the signal has to travel through the active area, which is different in every case (see Figure 3.4). We can see this new effect, which is added to the area effect (Devices A and B), but in this case we also change the place where the resonators are contacted by the RF probe tips. In Figures 5.2 to 5.3 a) - d), we can observe how the series resonance frequency is also affected by the probing spot effect. The phenomena behind this effect corresponds to the sheet resistance on thin film devices (see sub-sections 3.2.1 and 3.3.1). For instance, when we measure the bigger resonator (1A) at the pad, the new resonance is more evident, as shown in Figure 5.2 a) and b). The curves for the pad are represented in blue solid lines. On the other hand, the new resonator is less evident in the case of the corner measurements, which are represented in red solid curves.

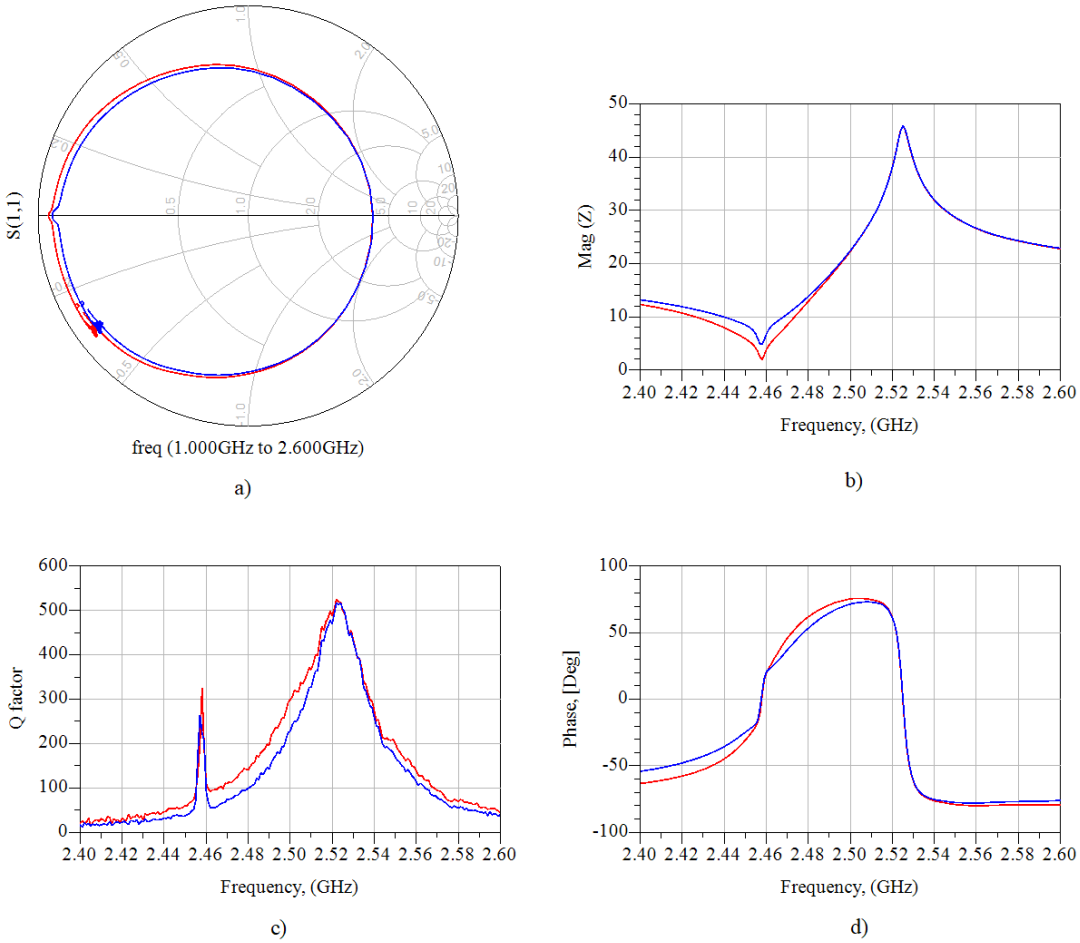

Figure 5. 2. Device (1A) measured at the corner and pad. (a) S (1, 1) in Smith chart. (b) Electric input impedance Z in dB ohms with series resonance at 2.458 GHz and 2.457 GHz for the corner and pad respectively. (c) Quality factors Q at resonance (series) and anti-resonance (parallel). (d) Z phase. The red curve is the measurement at the corner and the blue one is the data from the pad.

In Figure 5.3 we present data for a smaller resonator (1B), which was measured at three different probing spots (pad, corner and center). Each case corresponds to a different color curve (blue, red and magenta, respectively). We know that the new resonator will be less noticeable due to the size of the active area. Since the series resistance changes due to the probing spot, we can expect that effect of the new resonator in the center and corner will be less evident. For instance, for the case of the center, we see in the Smith chart (see Figure 5.3a) that the bump appears not to be there even for the corner case. In addition, in the input impedance (see Figure 5.3b), we can see the same effect. According to the theory of the sheet resistance, the series resistances (R_{x1} and R_{x2}) for these resonators at the corner and center will be almost the same. Another interesting thing can be observed in the quality factor graphs (see Figures 5.2c and 5.3c). The values at the series resonance frequency increase slightly when we measure closely to the center and corner of the resonator and decreases when we take the measurement far from the center (i.e., pad).

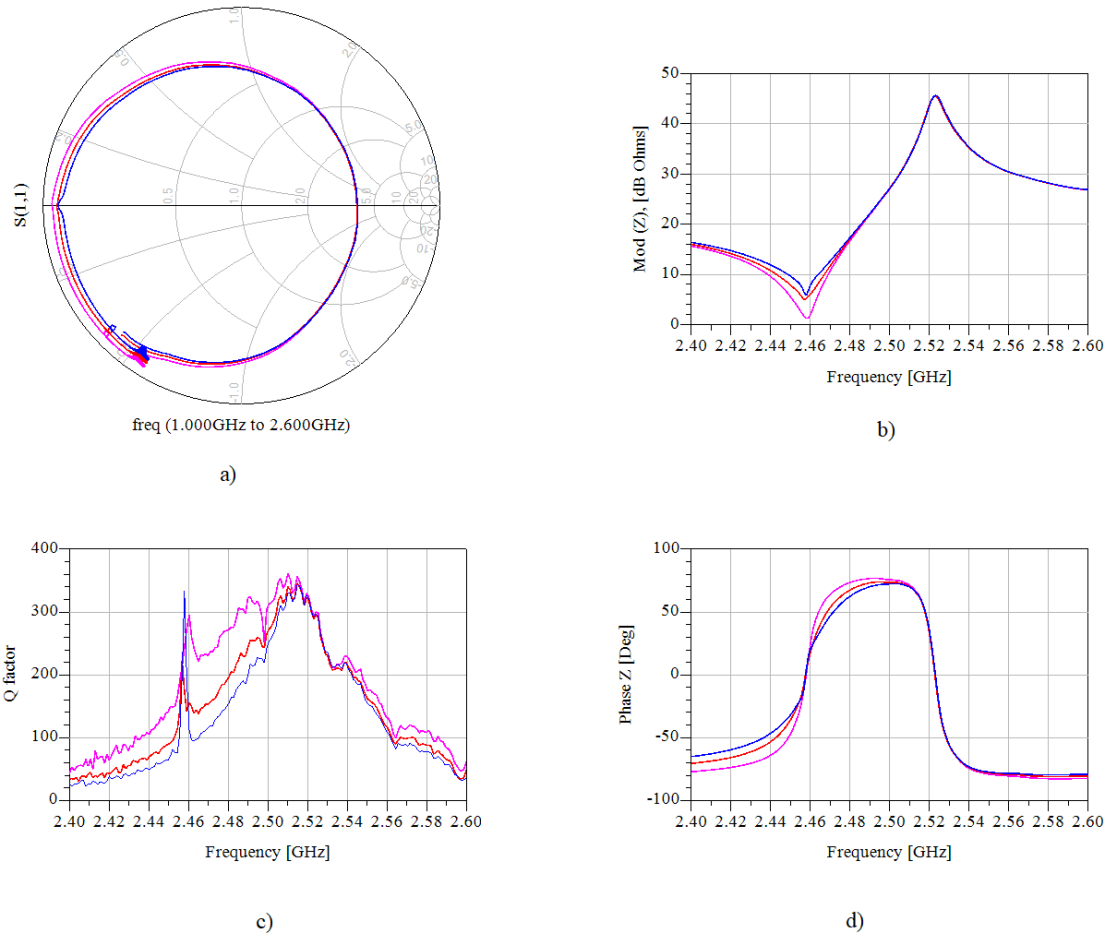

Figure 5. 3. Device (1B) measured at the corner and pad and center. (a) S (1,1) in Smith chart. (b) Electric input impedance Z in dB ohms with series resonance at 2.457 GHz, 2.458GHz and 2.459 GHz for the corner, pad and center respectively. (c) Quality factors Q at resonance (series) and anti-resonance (parallel). (d) Z phase. The red curve is the measurement at the corner, the blue one is the data from the pad and the magenta corresponds to the center.

Henceforth, since we know that series resonance frequency can be affected by the size of the active area and the probing spot, we have designed and modelled several SMRs in order to overcome and explain these phenomena. In addition, we have proved the accuracy of our models with data from our SMRs. The frequency range of the simulations goes from 0.1 up to 6 GHz. However, we only show a gap from 2.40 up to 2.60 GHz because there are no more modes in the wideband range. For these resonators the temperature is assumed to be 25°C, as room temperature. In the next sub-section we will show these results.

5.1.3. High Accuracy in Our Models

The next set of figures (Figure 5.4 to Figure 5.8) we are going to show the electrical responses of three SMRs (1A, 1B and 1D). Each device has a different effective area (see Table. 5.1). The resonators are simulated at three different probing spots (pad, corner and center). The models used to carry out the simulations are our updated versions of the mBVD and Mason one (sections 3.3.1

and 3.3.2, respectively). Additionally, we are going to compare our results with data from measured SMRs. We will prove that our models have excellent agreement and high accuracy according to the extracted data. In the first case we show the results for the biggest resonator (1A); this resonator was simulated and measured at the pad and also at the corner spot, which correspond to Figure 5.4 and Figure 5.5, respectively. In these figures we can see the corresponding curves for the updated mBVD, Mason models and the experimental measurements for each resonator corresponding. The black dash curve is for the mBVD, the red solid line corresponds to Mason's model and the blue solid line corresponds to the experimental data. Both figures are composed of four graphs from a) to d), which are related to the reflection coefficient at port 1, the electrical input impedance, the quality factor and the phase of the impedance, respectively. In addition, at the top of each figure we can see a representation of the active area of the resonator and the corresponding probing spot.

First, in Figure 5.4 a) we can notice for the reflection coefficient curves plotted into the Smith chart, a small bump (the new resonator) close to the main series resonance frequency (2.458 GHz, for 1A resonator). For this case the probing spot corresponds to the pad of the resonator. In Figure 5.5 a) the curves correspond to the corner of the active area. We clearly observe how at the corner the peak is reduced, while curves at the pad show a secondary peak more pronounced. Additionally, we note this difference in the rest of the curves. For instance, in both cases for resonator 1A (pad and corner), the impedance and its phase endure a heightened level of impact due to the new resonance at the pad, while the resonator probed at the corner is less affected. In the case of the smaller devices (1B and 1D), which have a smaller active area than device (1A), we observed the same effect when the simulation and measurements were performed towards the center of the active area (Figure 5.6 b) and c) and Figure 5.8 a), b) and d)). In these cases, the measurements and simulations were performed close to the center of the device and both present a less pronounced secondary peak (the new resonator contribution) since the distances towards the borders of the active area are almost the same (see Figure 3.4b). The smaller the area of the device is, the smaller the difference between their series resistances (R_{x1} and R_{x2}), becoming almost the same one. Therefore, this explains why the presence of this secondary peak at the series resonance is more pronounced for devices with larger areas and why the difference between R_{x1} and R_{x2} is reduced as we move towards the center of the devices, where the series resistances of all infinitesimal resonators connected in parallel becomes similar.

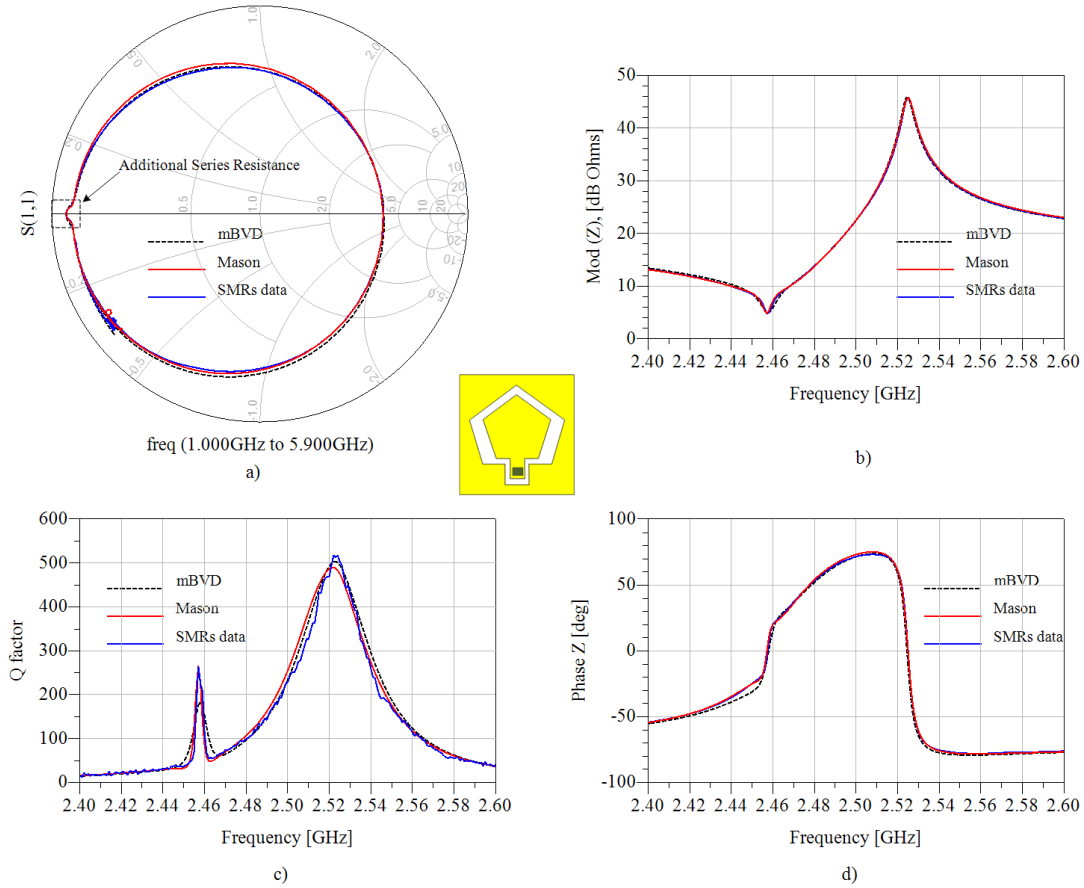

Figure 5. 4. Device (1A) measured at the pad. (a) S (1,1) in Smith chart where we can see the effect of the additional series resonance inside the grey square. (b) Electric input impedance Z in ohms with series resonance at 2.458GHz. (c) Quality factors Q at resonance (series) and anti-resonance (parallel). (d) Z phase. The short black dash curve corresponds to the mBVD model, the red one is the Mason model and the blue one is the experimental measurement.

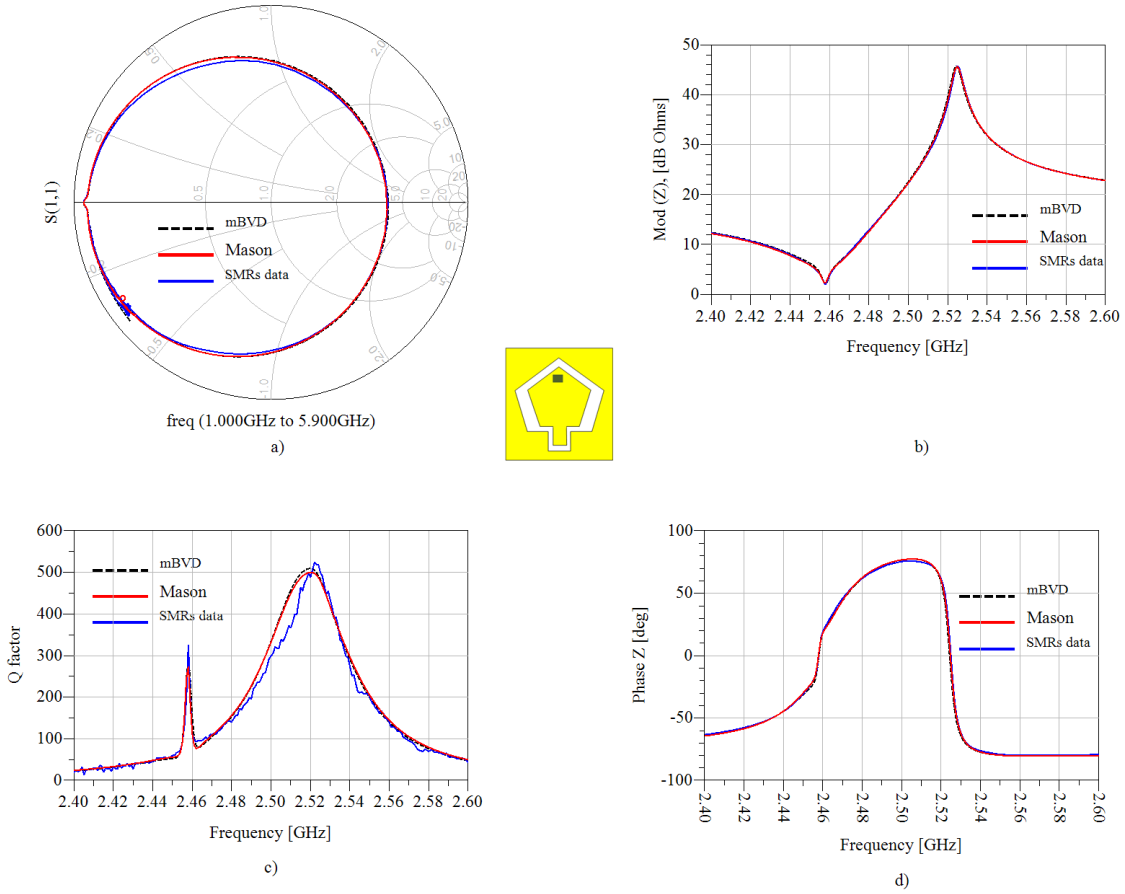

Figure 5. 5. Device (1A) measured at the corner. (a) S (1,1) in Smith chart, (b) Electric input impedance Z in ohms with series resonance at 2.458 GHz. (c) Quality factors Q at resonance (series) and antiresonance (parallel). (d) Z phase. The short black dash curve corresponds to the mBVD model, the red curve is the Mason model and the blue one is the experimental measurement.

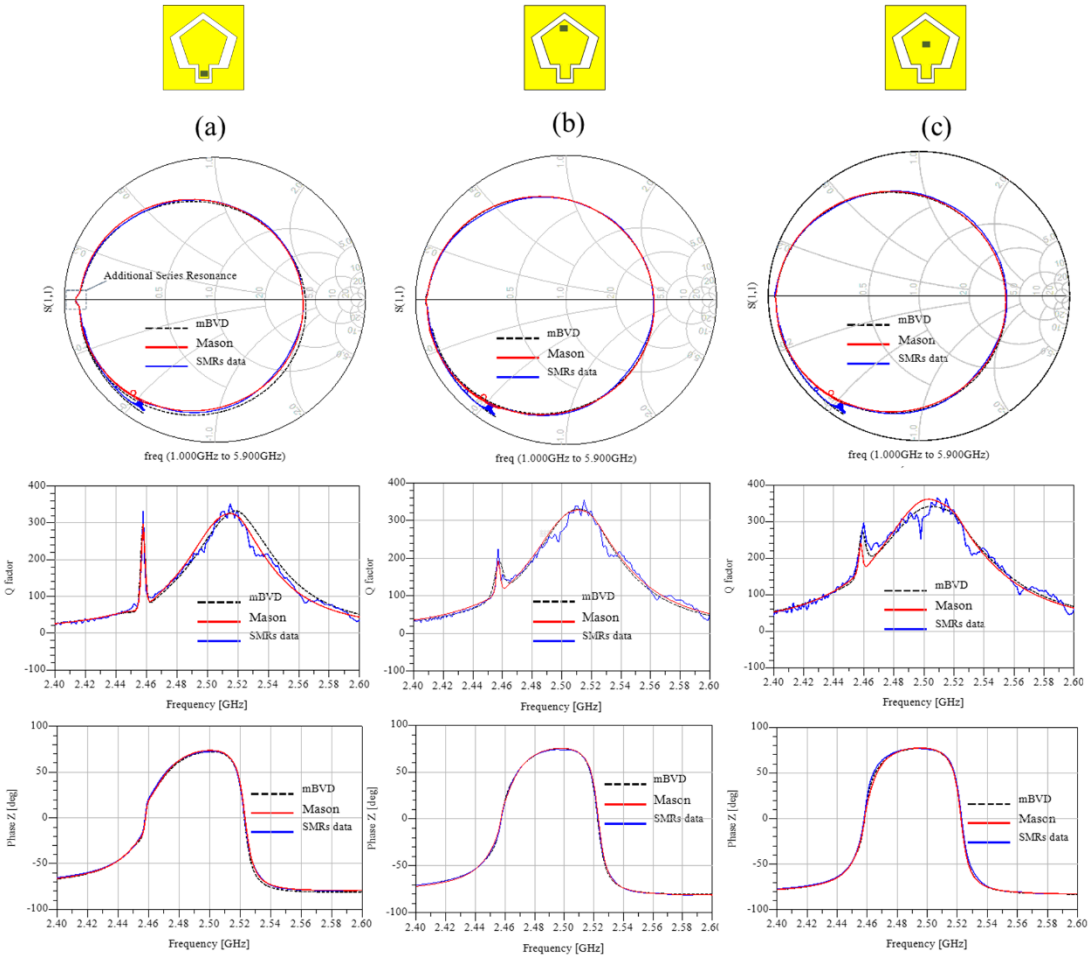

Figure 5. 6. Device (B) measured at the pad in column (a), corner in column (b) and center in column (c). First row shows the S (1,1) in Smith chart., second row the quality factors Q at resonance (series) and anti-resonance (parallel) and the third row the impedance phase. The short black dash curve corresponds to the mBVD model, the red curve is the Mason's model and the blue one is the experimental measurement.

Figures 5.7 and 5.8 show the electric response of the smallest resonator (1D) for the simulated and experimental cases at the pad and corner, respectively. We can notice immediately that the second resonator barely affected at the series resonance for both probing spots (see Figures 5.7 and 5.8 for a, b and d cases). This is because under the probe tips there are resonators connected in parallel with almost the same series resistance value ($R_{x1} \approx R_{x2}$). Since the path that the electric signal has to travel is almost the same in all directions because the size of the active area, for the smallest cases the difference between R_{x1} and R_{x2} in both probing spots is almost zero (0.1Ω for our models, mBVD and Mason). These values can be seen in Table 5.3. Additionally, the quality factor presents a similar behavior, although the values for the corner are greater than the pad scenario. The data presented in Table 5.3 and Table 5.4, proves our hypothesis about both active area and probing spot effects.

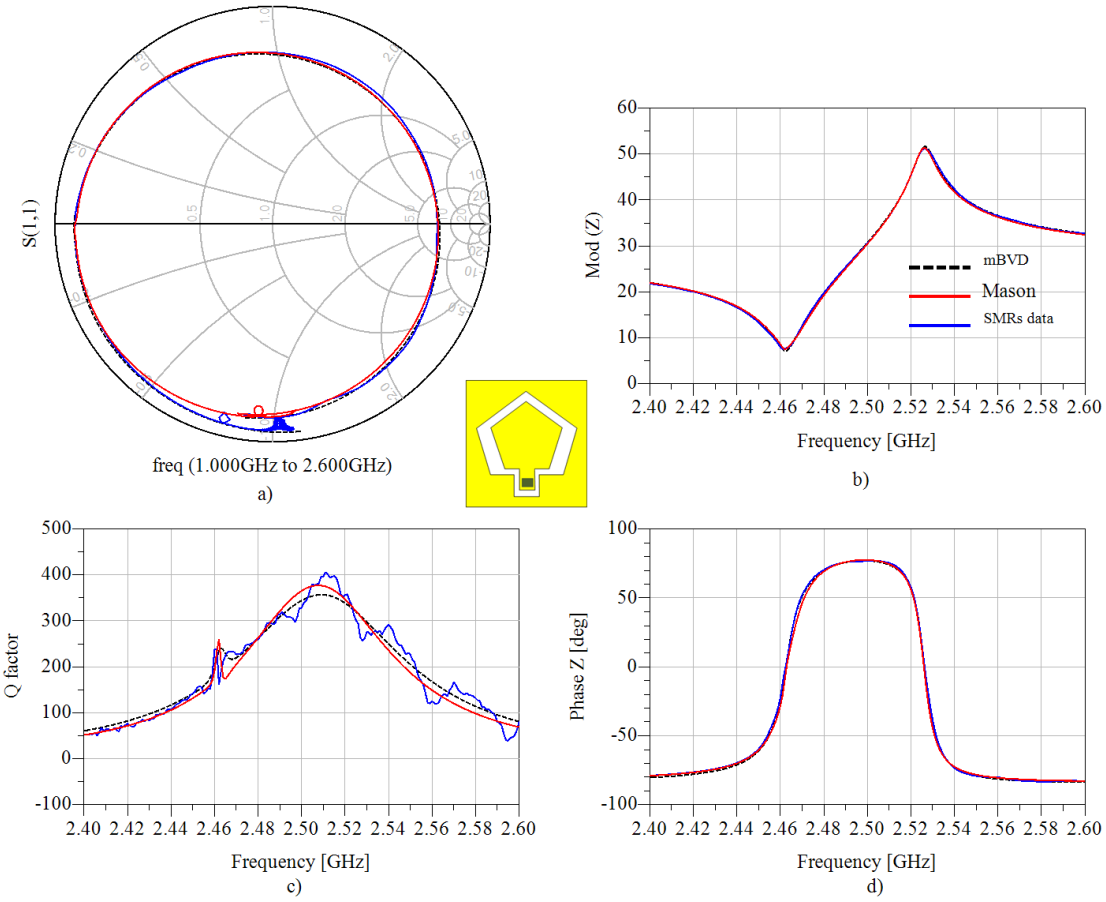

Figure 5. 7. Device (1D) measured at the pad. (a) S (1,1) in Smith chart where we can see barely the effect of the additional series resonance inside the grey square. (b) Electric input impedance Z in ohms with series resonance at 2.458GHz. (c) Quality factors Q at resonance (series) and anti-resonance (parallel). (d) Z phase. The short black dash curve corresponds to the mBVD model, the red one is the Mason model and the blue one corresponds to the data measurements.

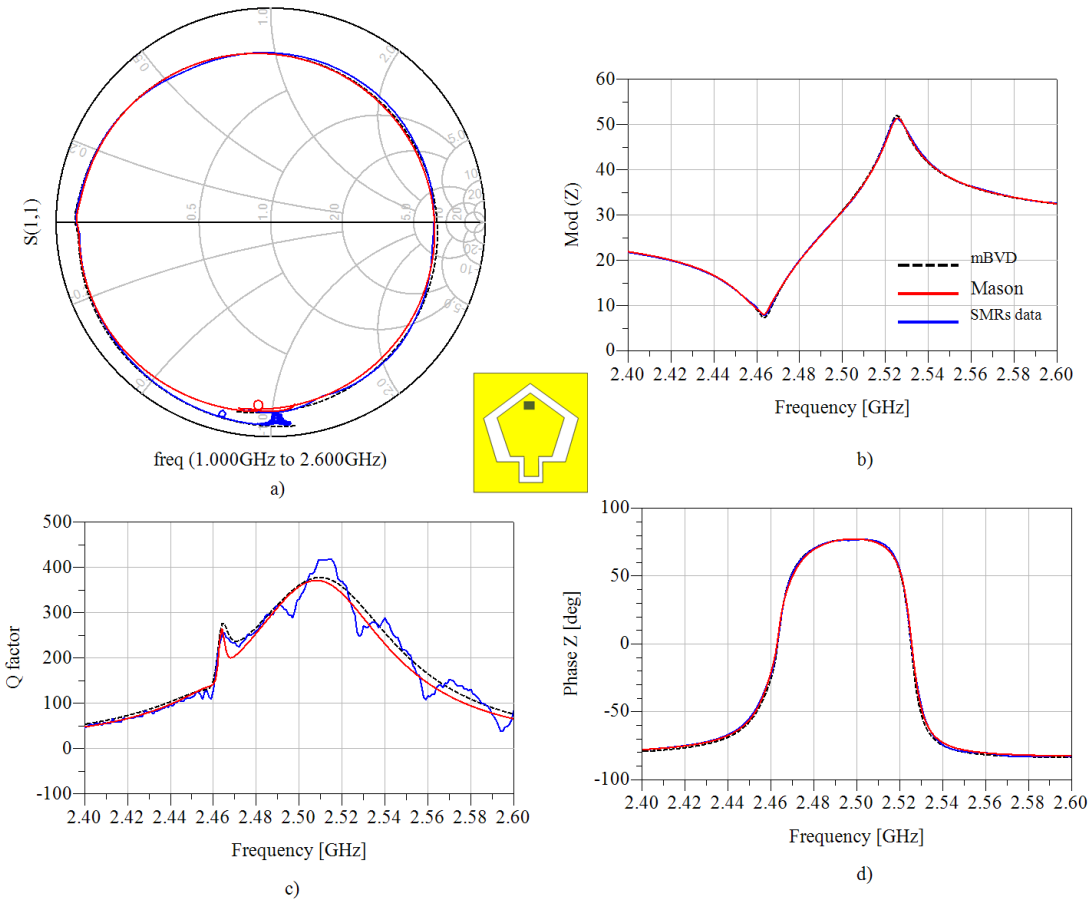

Figure 5. 8. Device (1D) measured at the corner. (a) S (1,1) in Smith chart where we can see barely the effect of the additional series resonance in the Smith chart representation. (b) Electric input impedance Z in ohms with series resonance at 2.458GHz. (c) Quality factors Q at resonance (series) and anti-resonance (parallel). (d) Z phase. The short black dash curve corresponds to the mBVD model, the red one is the Mason model and the blue one corresponds to the data measurements.

5.1.4. Series Resistances (R_{x1} and R_{x2}), the main and new resonator

We summarize the values of R_{x1} and R_{x2} for three resonators (1A, 1B and 1D) in Table 5.3. The R_{x1} and R_{x2} values correspond to the series resistance for the main and the new resonator, respectively. Both values are proposed in our updated models (see Figures 3.5 and 3.9 b). In Table 5.3 we report the series resistance values, which were extracted from the real part of the impedance computed at low frequencies. If we analyze some of these values, we can prove that these ones are related to the size of the active area and also the probing spot. For example: the Ohmic losses obtained by means of mBVD model at the pad for a big device (1A) are R_{x1} = 2.9 Ω and R_{x2} = 2 Ω. Their difference is 0.9 Ω, which is a big difference as we have expected. On the other hand, if we see the values for a smaller resonator (i.e., 1B) at the corner, R_{x1} and R_{x2} are 1.9 and 1.8 Ω, respectively, and the difference is 0.1Ω, which is a small value as we have expected too. Meanwhile for the same resonator (1B) measured at the pad the values are 2.9 Ω and 2.2Ω,

showing again a big difference between them. Henceforth, when we measure our devices at large distances from the center of the active area the signal has to travel more distance and the Ohmic losses increase according to the theory described in section 3.2.1. The influence of these resistances is directly translated to the series quality factors, as shown in Table 5.4. For instance, in the case of device (B), the closer to the center the lower the series resistance and hence higher *Qs*. We can infer from all these results that smaller areas reduce the effect of secondary peaks at the series resonance.

Table 5. 3. Series resistances vales (Rx1 and Rx2) of three resonators (1A, 1B and 1D), respectively. Each resonator has values for pad and corner, only (1B) has the three probing spots (pad, corner and center). The last column contents the series resistance extracted.

Device	**Spot**	**mBVD**		**Mason**		**Extracted**
		Rx1 **[Ω]**	***Rx2*** **[Ω]**	***Rx1*** **[Ω]**	***Rx2*** **[Ω]**	***Rx*** **[Ω]**
(1A)	pad	2,9	2	2.9	2.05	3.2
(1A)	corner	1.9	1.5	1.9	1.5	2.3
(1B)	pad	2.8	2.2	2.75	2,2	3.1
(1B)	corner	1.9	1.8	1.9	1.7	2.2
(1B)	center	1.3	1.1	1.2	1.1	1.7
(1D)	pad	2.9	2.8	2.5	2.5	2.9
(1D)	corner	2.9	2.8	2.5	2.5	3

5.1.5. Performance at Room Temperature

Table 5.4 lists the most significant parameters for our SMRs, which are important in the sensors design (see sub-sections 2.3.3 and 2.3.4.). These parameters were extracted from our data measurements and simulating for three different probing spots (pad, corner and center) and for three different active areas (1A, 1B and 1D), all of them at room temperature 25°C (298.15K). The third and fourth columns show the series and parallel resonant frequencies, respectively. It is interesting to see the effect of the area on f_s, which reveals that when the size of the active area changes, the series resonant frequency changes too. This is an important parameter that we have to take into account in gravimetric sensing applications based on SMRs since the series resonance frequency affects directly the sensitivity. Then, we can see the effective piezoelectric coupling coefficient, which is calculated in terms of the distance of the frequency resonances (f_s and f_p). The value of this parameter for all cases is almost the same, around 6%, which is an expected value for SMRs based on AlN. Finally, we present the quality factor values for series resonance (Q_s) and parallel one (Q_p) for our three devices at each probing spot. For instance, the larger values of the series quality factor correspond to geometries measured near the center of the active area. Henceforth, we can conclude that the size of the active area and probing spot affect directly the series quality factor due to Ohmic losses in devices based on thin films such as SMRs.

Table 5. 4. Performance of three SMRs (1A, 1B and 1D) at different probing spots. Each resonator has values for pad and corner, only (1B) has the three probing spots (pad, corner and center).

Device	Spot	f_s	f_p	K_{eff}^2	Mason		mBVD		Extracted	
		[GHz]	[GHz]	[%]	Q_s	Q_p	Q_s	Q_p	Q_s	Q_p
(1A)	pad	2.458	2.526	6.467	190	475	232	490	264	503
(1A)	corner	2.458	2.526	6.467	274	468	300	483	325	490
(1B)	pad	2.457	2.523	6.289	195	309	200	305	264	291
(1B)	corner	2.457	2.523	6.289	225	300	218	300	281	289
(1B)	center	2.458	2.523	6.196	241	309	263	305	321	293
(1D)	pad	2.463	2.526	6.003	250	315	240	334	239	290
(1D)	corner	2.464	2.526	5.910	255	310	260	360	250	294

5.2. High Temperature Analysis (22 to 422°C)

In this section we present a model for our SMRs capable of handling extreme temperatures as input and operation in the GHz range. One of the most used tools for thin film resonators is the well-known Finite Element Method (FEM) [103], [104]. This method is capable of solving the set of constitutive equations (2.31) for each layer of the resonator (electrodes, piezoelectric and acoustic reflector) including the substrate. By solving these equations we are able to see the temperature profile, Strain and particle displacement on each film. However, this method is not a good option if we want to accelerate the characterization process of the resonators. The FEM method consumes too many computational resource. Even though this is a robust and reliable method, it is not the principal option to carry out the modelling of our SMRs. Henceforth, we need an accurate and simple model that can predict the SMRs behavior at high temperatures. We present our updated version of the mBVD model, which is capable of operating at low and high temperatures. In this sub-section, we show the results of simulations at high temperatures (from 25 ºC to 420°C). We have verified our model by means of extracted data of our fabricated SMRs at 2.4 GHz. These fabricated SMRs are not the same as those used to prove the active area and probing spot effects (see section 5.1). Although the differences between both configurations are not pronounced, we introduce the new configuration in the next sub-section. On the other hand, in order to follow the changes in the series resonance frequency and quality factor, we have also added the area and probing spot effects (Ohmic losses). In other words, first, we model the active area and probing spot effects and then the temperature changes.

5.2.1. SMRs with a Gold Passivation Layer

The new SMRs were fabricated by means of the same methodology followed in section 3.1. However, the new resonators have a new acoustic reflector, which has 9 alternating layers of SiO_2 and Mo, respectively. Furthermore, they have a passivation gold (Au) layer onto the top electrode. This layer prevents the oxidation of the top electrode at high temperatures. The thickness of this layer is 50 nm (see Figure 5.9a). The mask used to pattern the active area of the resonators onto the top electrode is different from the first resonators. The active area of the studied SMR including the pad is 74,322 μm^2. Our resonator is referred as F10 (see Fig. 5.9 b). In addition, the thickness of the piezoelectric AlN film is 900 nm. The bottom and top electrodes are made of Ir with 120 nm and 100 nm of thickness, respectively. The top and bottom electrodes are coupled capacitively in order to avoid the through-holes process. Finally, at each interface of the Mo and SiO_2 films there is a thin film of Titanium (13 nm), which is used to improve the adhesion.

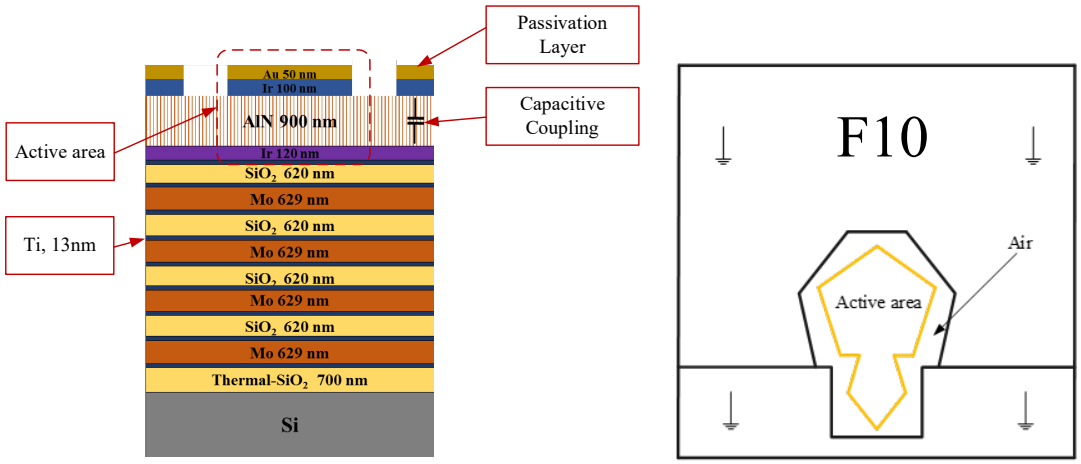

Figure 5. 9. Fabricated-SMR with capacitive coupling between top and bottom electrodes. Where, a) is the stack composition of the resonator in the bulk configuration and b) corresponds to the shape of the effective area of the resonator, which is in yellow. The rest of the metallization corresponds to the ground plane which is in black (where the ground symbol is drawn).

5.2.2. Temperature Dependence Equations

The electrical and physical properties of the resonators change according to the temperature variations. To deal with this issue, we are going to include the temperature input in our updated models. To improve the accuracy of the model an attempt to extract the temperature dependence of dielectric permittivity ε_{33} is made. Afterwards, our model is modified to take into account the temperature dependence of the thickness (d), Area (S), dielectric permittivity (ε), and piezoelectric coefficient (e). The temperature dependence of these parameters can be computed by means of the equations used in [58]. We have carried out these computations by specific

functions programming in Matlab. Then we use them as an input in our model. Our first approach of the temperature dependence model at high temperatures was made for a frequency operation of 2.4 GHz. We compare the most remarkable outputs with data measurements from our new device (F10). These variables are: *fs, fp, keff*^{2}, and *Q*. As explained above, the temperature-dependence was taken into account in our model by means of the set of equations used in the article written by Brice Ivira [58]. These equations behave as linear variation around room temperature. First of all, the thickness of the piezoelectric material is expressed in equation (5.1).

$$d_{(T)} = d_{(T0)}[1+\alpha(T-T_0)] \tag{5.1}$$

Where $d_{(T0)}$ is the AlN thickness at room temperature, T is the temperature variation, T_0 is the temperature at room temperature and α is the thermal expansion coefficient of the piezoelectric film. However, we have to take into account that the c-axis AlN is not an isotropic material, then equation 5.2 must reconsider the thermal expansion coefficient expression as follows.

$$d_{(T)} = d_{(T0)}[1+\alpha_{33}(T-T_0)] \tag{5.2}$$

$$S_{(T)} = S_{(T0)}[1+\alpha_{11}(T-T_0)][1+\alpha_{22}(T-T_0)] \tag{5.3}$$

$$e_{33(T)} = e_{33(T0)}[1+Te_{33}(T-T_0)] \tag{5.4}$$

$$\varepsilon_{33(T)} = \varepsilon_{33(T0)}[1+T\varepsilon_{33}(T-T_0)] \tag{5.5}$$

$$C0_{(T)} = \varepsilon_{33(T)} S_{(T)} / d_{(T)} \tag{5.6}$$

Where α_{33} is the thermal expansion coefficient in the propagation direction (thickness direction).

On the other hand, we also have to consider the active area of the resonator since this parameter also affects the series resonance frequency. In addition, the effective area is a temperature dependence parameter. The equation that governs its behavior is written down in expression 5.3. This value is useful since we are able to compute the static capacitance C_0 as equation (5.6) does. Temperature coefficient of piezoelectric coefficient (Te_{33}) and dielectric permittivity ($T\varepsilon_{33}$) are written in equations (5.4) and (5.5), respectively. The value of these coefficients were taken from [58] including the value for thermal expansion coefficient. All were extracted from measurements. Furthermore, these values can operate at our range of temperature (22°C to 422°C). On the other hand, the series resistance also changes with the increment of temperature, which means losses due to ohmic effects increment as the temperatures increases. We have made an attempt to extract them using our temperature dependence model. Additionally, mechanical

and material losses are temperature dependence variables. Finally, in Table 5.5 we have summarized the final temperature dependence values used to model our resonators at high temperatures. The extracted values of series resistances (Rx_1 and Rx_2), mechanical and dielectric losses (R_1 and R_2) and (R_{O1} and R_{O2}), respectively, are shown

In order to prove the accuracy of our model, we extract the S parameters of the F10 resonator at different temperatures (22 to 422°C). The methodology used to carry out this set of measurements at high temperatures and room pressure is such the methodology described in section 4.2. However, the setup measurement is different. Next sub-section describes the setup and also the procedure to extract the data from our SMRs.

Table 5. 5. Temperature dependence values for the updated mBVD model at high temperatures (22 to 422°C).

Temperature [°C]	**Area [1^{-12} µm^2]**	**Thickness (d) [nm]**	**Permittivity ($\mathcal{E}$)**	R_{x1} [Ω]	$Rx2$ [Ω]	R_{O1} [Ω]	R_{O2} [Ω]	R_1 [Ω]	R_2 [Ω]
22	75,325	900	9.50	3.5	1.5	0.01	0.01	0.29	0.29
107	76,525	900	9,62	4.0	1.9	0.01	0.01	0.37	0.21
151	78,325	903	9.70	5.0	1.9	0.01	0.01	0.34	0.20
224	79,325	905	9.80	5.1	2.0	0.01	0.01	0.41	0.34
296	79,425	908	10.10	5.6	2.6	0.01	0.01	0.60	0.10
422	77,325	910	10.30	6.0	5.1	0.01	0.01	0.74	0.15

5.2.3. Probe Tips Station Measurements for High Temperatures

We verify our models by means of data from our new fabricated SMRs. The measurements were taken in a controlled setup environment (see Figure 5.10). The response of our SMRs in terms of frequency at different temperatures was assessed by measuring the reflection parameter. The in-situ high-temperature measurements were carried out using a modified RF probe tip. The probe tip was modified since the requirements for this measurements at such temperatures were different from cryogenic ones. We have employed the method suggested by Schwartz et al in [105]. This method was used in [64] in order to condition the probe tips for high power dissipation. The modification consists in attaching a film of copper (Cu) as a heat spreader to the RF probe tips (Figure. 5.10 a)). On the other hand, the heater is a stainless steel holder housing a double coil of Inconel sheathed heating cable (See Figure 5.10b).

A typical measurement cycle consisted in increasing the temperature up to 422°C in steps of 50°C. Afterwards, we have registered the frequency response after reaching the steady state. The whole cycle lasted typically 30 minutes. The VNA calibration was made at room temperature.

The calibration remains almost stable during the heating cycle barely affecting the measurements of the resonators. After the cooling cycle, the respond as function of frequency was almost identical to that recorded before the heating cycle. Henceforth, one calibration assures us high accuracy measurements.

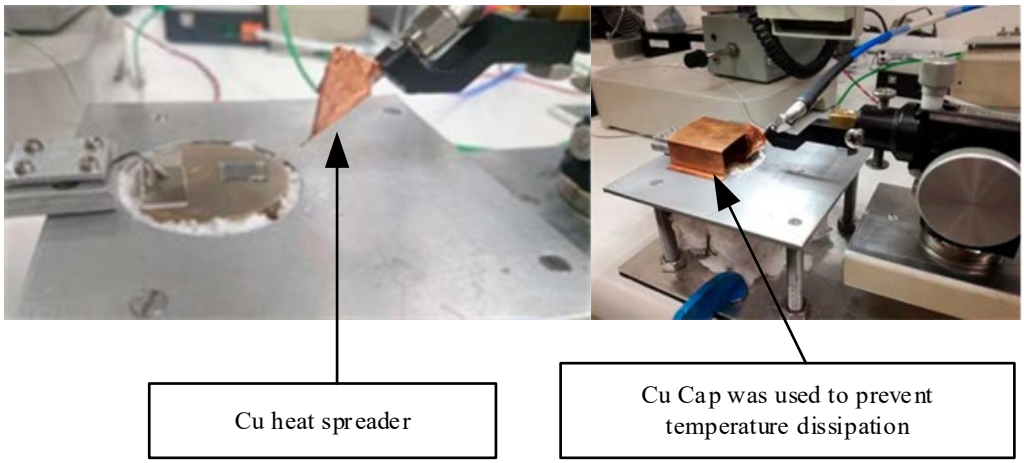

Figure 5. 10. Setup modified for high temperature measurements at room pressure. In a) is showed the RF probe tips with a heat spreader made of Cupper (Cu), then b) a Cu Cap is used to prevent temperature dissipation [64].

5.2.4. Accuracy of the Temperature Dependence Model

In this section we present the most important parameters of our updated temperature dependence model. We specifically analyzed resonator F10 for high temperatures. In the next sub-section we will additionally present results in a wider range of temperature (-160°C up to 130°C). We can observe how our temperature-dependence model predicts the performance of our devices. For instance, the quality factors obtained for 22 and 422°C are summarized next, Q_p = 903, Q_s=300 and k_{eff}^2 = 6.17% and Q_p = 381, Q_s = 101 and k_{eff}^2= 5.42%, respectively. The model was optimized using the input data from the linear equations of temperature and data measurements.

Since we want to observe the series resonance frequency, we have computed the input impedance for each temperature. In Figure 5.11 a) and b) we can observe their corresponding curves for the impedance and also its phase. The curves are plotted as a function of frequency at different temperatures (22ºC to 422°C). We can see that between the experimental data and simulations there is high agreement for all cases. In both graphs each temperature is represented by a different color (solid lines). For the simulations the corresponding curves are a black dash line. We have proved that our updated model works for high temperatures on SMRs, which reduces the computational resources and simulation without compromising the results.

5.2.4.1. Temperature Coefficient of Frequency

The temperature coefficient of frequency (TCF) refers to the change in resonance frequency due to temperature variations. In SMRs the TCF is a measure of the sensitivity for their frequency dependence as a function of temperature and is usually expressed in parts per million per Celsius degrees (ppm/°C). This quantity can also be presented in Kelvin. This quantity indicates the frequency shift that occurs for every degree Celsius. The TCF can be positive or negative. It can depend on many factors such as the type of piezoelectric material and its temperature characteristics. For instance, a positive TCF means that the resonant frequency increases as temperature rises, while a negative TCF indicates that the frequency decreases when the temperature increases. In gravimetric sensing at harsh environments, it is important to consider this quantity to ensure the stability and the accuracy of frequency-dependence as a function of the temperature.

The TCF for both resonance frequencies can be computed by means of equations (5.7) and (5.8), for the resonant and anti-resonant frequencies, respectively.

$$TFC_s = \left(\frac{1}{f_{s(T0)}}\right)\left(\frac{df_s}{dt}\right) \tag{5.7}$$

$$TFC_p = \left(\frac{1}{f_{p(T0)}}\right)\left(\frac{df_p}{dt}\right) \tag{5.8}$$

Where $f_{s(T0)}$ is the series resonance frequency at room temperature (22°C). From measurements df_s/dt is the fitted slope of the series resonance frequency as a function of the temperature. Likewise, the same relation is used for the TCF for the parallel resonance frequency. Since we have defined this quantity, we can compute it for the series resonance frequency since we are interested in it. The TCF for the series resonance frequency is -30 ppm/°C (see Table 5.7). In order to understand this coefficient, Figure 5.12 shows the tendencies as a function of the temperature for both resonance frequencies. Both TCF decrease with temperature, meaning a negative value. Their tendencies obey a lineal behavior. The TCF for the parallel resonance frequency f_p appears to change less than f_s. This can be explained by the use of SiO_2 layers on the acoustic reflector. This material has a positive temperature coefficient of frequency and acts as a temperature compensation material.

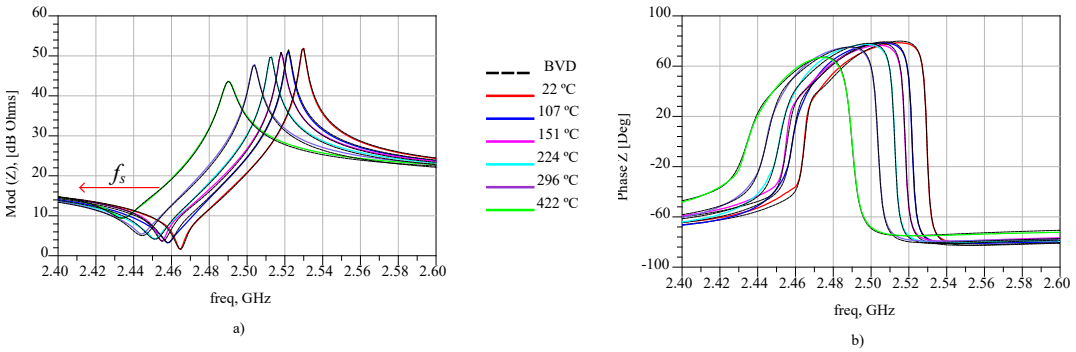

Figure 5. 11.) Represents the input impedance modulus in [dBΩ], and b) is the phase of the impedance at different temperature (22°C up to 422°C). The black dash curves represent the updated temperature-dependence model, while the solid lines represent the measurements for each temperature.

5.2.4.2. Effective Piezoelectric Coupling Coefficient and Quality Factor as a Function of Temperature

The effective piezoelectric coupling factor (K_{eff}^2) was defined in section 2.3.4 and it measures how electrical energy is transformed into the mechanical one and vice versa. The values obtained for this resonator as a function of the temperature slightly decreases when temperature increases (see Figure 5.12, second row). The values obtained are around 6%. However, this value slightly decreases as temperature increases, which is in good accordance with data from measurements. On the other hand, the quality factor is an important parameter and it has to be taken into account for our SMRs performance. Q also tells us that damping mechanism occurs in the resonator structure. In the case of high temperatures those mechanisms could increase. For our resonators, those effects are clearly noticeable for the parallel quality factor (Q_p) (see Figures 5.13 and 5.14). We can extract the quality factor for both resonances of our SMRs at room and high temperatures. The equation that we have used can compute both quantities since with this equation we can calculate it for the whole frequency range [85]. In Figure 5.13, the red and green solid lines correspond to the measurements at 22°C and 422°C temperatures, respectively. The black dash curve corresponds to our temperature-dependence model. Then we can see that the parallel quality factor decreases considerably and the series quality factor apparently does not change drastically when the temperature raises. Regardless, we have not found any particular trend for the quality factor variation with temperature. On the other hand, we think that spurious modes could hamper the resonances, especially for the series resonance frequency but the properties of spurious modes are very difficult to control, particularly with respect to the temperature. Henceforth, in this section we have also considered the presence of the secondary peak near the series resonance frequency, which we have called the area and probing spot effects. Hence, our model is optimized and we can notice it in the results that present excellent agreement and high accuracy.

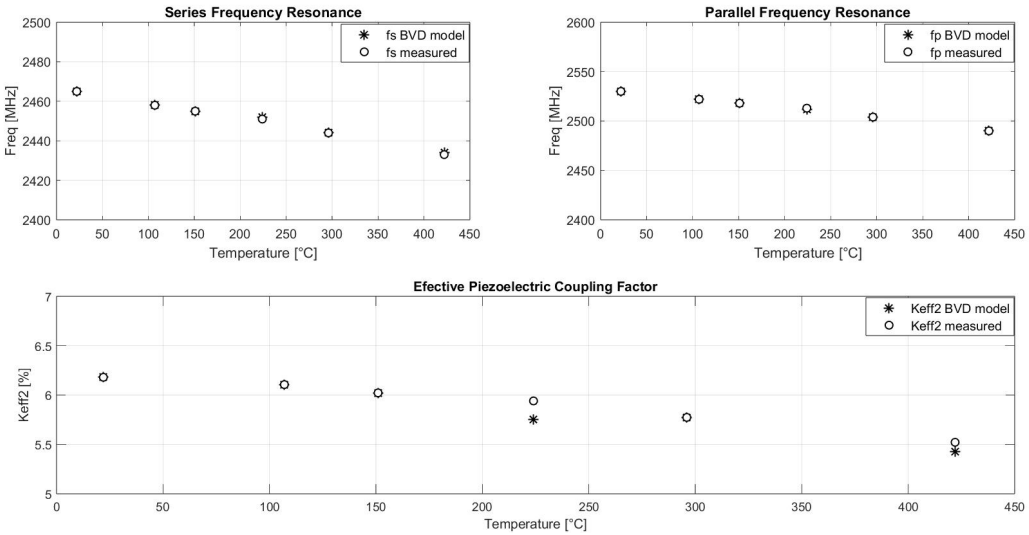

Figure 5. 12. Series and Parallel frequency resonances (fs) and (fp) and the effective electro-acoustic coupling coefficient ($Keff^2$) vs temperature respectively since 22°C up to 422°C. The asterisk markers represent the temperature-dependence mBVD model and the circles are the data measurements from our fabricated solidly mounted resonator.

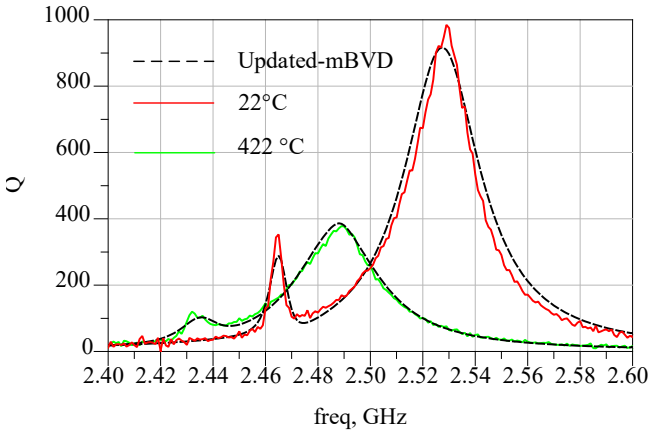

Figure 5. 13. Quality factor at 22 and 422° C. The red curve represents the room temperature case and the green one is for the 422°C case. The short black dash curve represents the data from updated mBVD model.

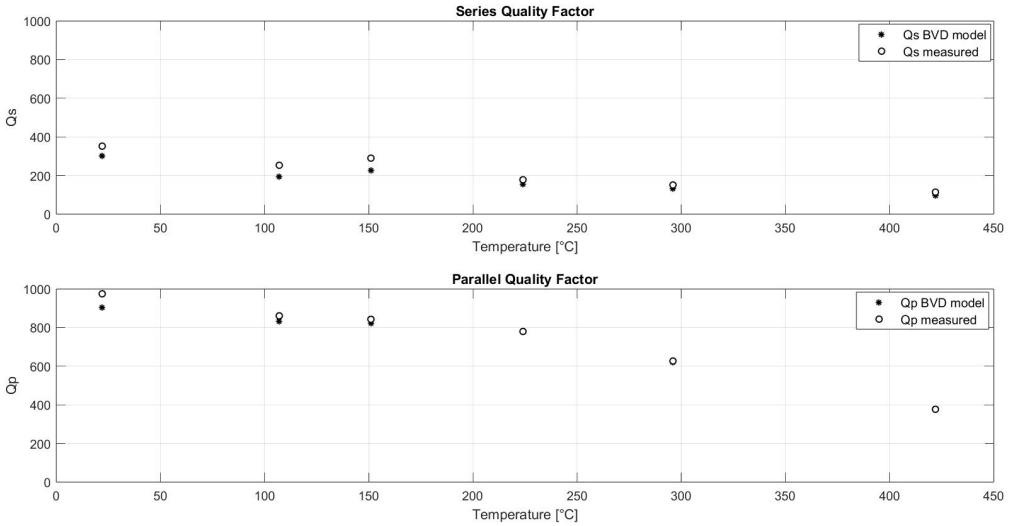

Figure 5. 14. Series and Parallel quality factors from 22°C up to 422 °C. The asterisk markers represent the high-temperature mBVD model values and circles represent Qs and Qp extracted from the measurements respectively.

5.3. Low Temperature Analysis

An important aim of this thesis was the analysis at cryogenic temperatures of SMRs. Only few researchers have carried out this analysis at temperatures lower than -170°C [58]. This can be due to the lack of applications at such temperatures. On the other hand, the modelling at these temperatures has been normally carried out by means of FEM simulations. Again, this method consumes many computational resources and a huge amount of time by each simulation attempt. We have modified our simple model to include low temperatures effects. This analysis was carried out from -120 up to 130 °C. Our results are reliable enough for our purposes and present good agreement with the experimental data. The measurements were carried out in our semiautomatic probe station measurements following the methodology proposed in section 4.2. The resonators proposed in this section are slightly different from those used in the high temperature analysis. The difference mainly consists in the thickness and material of the top electrode, which is made of 200 nm of Mo. Furthermore, the passivation layer is not presented in these resonators since the risk of oxidation is not present. Apart from that, the configuration materials remain similar to the F10 resonator presented for high temperatures. The size of the active is the same, 74,322 μm^2. In Figure 5.15 we can see the configuration stack of this resonators.

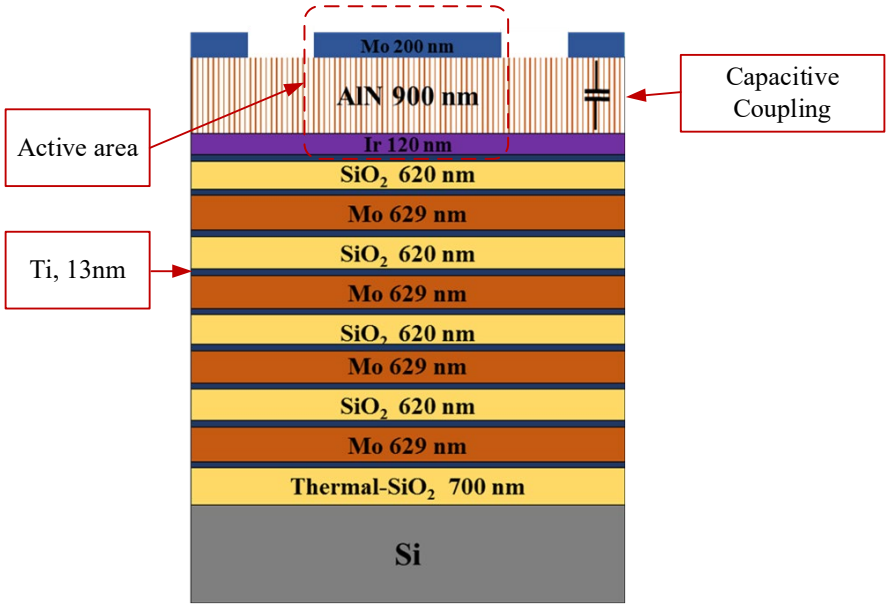

Figure 5. 15. Fabricated-SMR with capacitive coupling between top and bottom electrodes. There is the stack composition of the resonator in the bulk configuration. The active area is 74,322 μm^2.

5.3.1. Modelling at Very Low Temperatures (-120°C to 130°C)

For these simulations at very low temperatures, we have also employed the linear equations of temperature, which have consistently produced excellent results. We conducted our simulations within the temperature range of -120°C to 130°C. In addition, we measured and characterized our fabricated devices starting from -170°C, since our system is capable of taking such measurements. However, we have not included simulations below -120°C due to measurements below this temperature exhibit a nonlinear behavior which is not contemplated in our updated models. For example, the series resonance and parallel resonance frequencies present a nonlinear behavior and their TCF is positive. This behavior was noticed between (-170°C to -140°C). The reasons that could explain such behavior are the nonlinear variations of the intrinsic material properties such as the piezoelectric coefficient (e), stiffness coefficient (c) and dielectric permittivity (ε).. Regardless, at these temperatures there are interesting applications such as satellite and space telecommunications, they are not part of our range of applications. Table 5.6 summarizes the final temperature-dependence values used to model our resonators from -120°C up to 130°C. We included the extracted values of series resistances (Rx_1 and Rx_2), mechanical and dielectric losses (R_1 and R_2) and (R_{O1} and R_{O2}), respectively.

Table 5. 6. Temperature dependence values for the updated mBVD model at very low temperatures (-120 to 130°C).

Temp [°C]	**Area [1^{-12} µm^2]**	**Thickness (*d*) [nm]**	**Permittivity (ε)**	***R*$_{x1}$ [Ω]**	***R*$_{x2}$ [Ω]**	***R*$_{O1}$ [Ω]**	***R*$_{O2}$ [Ω]**	***R*$_1$ [Ω]**	***R*$_2$ [Ω]**
-120	73,000	895	8.8	1,9	1	0.01	0.01	0.74	0.14
-90	73,200	895	9.09	3.1	0.9	0.01	0.01	0.80	0.17
-60	74,500	896	9.25	3.6	0.8	0.01	0.01	0.84	0.22
-30	74,000	898	9.20	2.6	0.9	0.01	0.01	0.65	0.17
0	74,400	900	9.30	3,1	0.9	0.01	0.01	0.70	0.23
30	74,100	905	9.39	3.7	1.1	0.01	0.01	0.73	0.20
60	74,300	906	9,40	4	1.0	0.01	0.01	0.79	0.19
90	74,400	907	9.44	4	1.1	0.01	0.01	0.74	0.19
120	75,000	908	9.53	3.3	1.2	0.01	0.01	0.67	0.12

5.3.2. Measurements at Very Low Temperatures

We have carried out a set of measurements of different devices at cryogenic temperatures. We are going to present the results for one resonator that corresponds to the F10 configuration (see Figure 5.15). We have described the complete methodology to measure our devices in our semiautomatic probe station measurements at such temperatures in section 4.2. In the next sub-section we are going to summarize the procedure used to carry out such measurements.

5.3.2.1. Methodology

First we have calibrated the vector network analyzer at room temperature using the methodology described in section (4.2.4). Then, we started to decrease the temperature in steps of 10°C. We carried out the measurements at each temperature (i.e., 10, 0, -10, etc.). The measurement was taken when the temperature was almost constant. In order to ensure a reliable measure, we have waited at least 10 minutes for the stabilization of the temperature at each level (see Figure 4.11). Once we have reached the lowest temperature (-170°C) and taken the corresponding measurement, we started to increase the temperature and took some measurements at similar temperatures. These measurements were taken in order to compare data at freezing and healing cycles (see Figure 5.16) and discard differences since resonators were subjected to compressing and decompressing cycles that could affect their performance. Also in Figure 5.16, we can notice that the electrical response remains stable for two cases of temperature -120°C and 0°C, for a) and b), respectively.

5.3.3. Results of Modelling and Extracted Data

In the next set of figures (Figure 5.17 to Figure 5.21) we present the results obtained from this study carried out at very low temperatures by means of our updated model. The simulations are presented together with data measurements in order to observe how accurate our model is. These results are represented in terms of the temperature. In addition, we present results for both analysis (low and high temperatures) since our proposed resonators are fabricated with different stack configuration (see Figures. 5.9 and 5.15). The purpose of this comparison is to know if the tendency of the principal outputs such as series resonance frequencies are similar. Otherwise, our simulations and experiments had to be reconsidered.

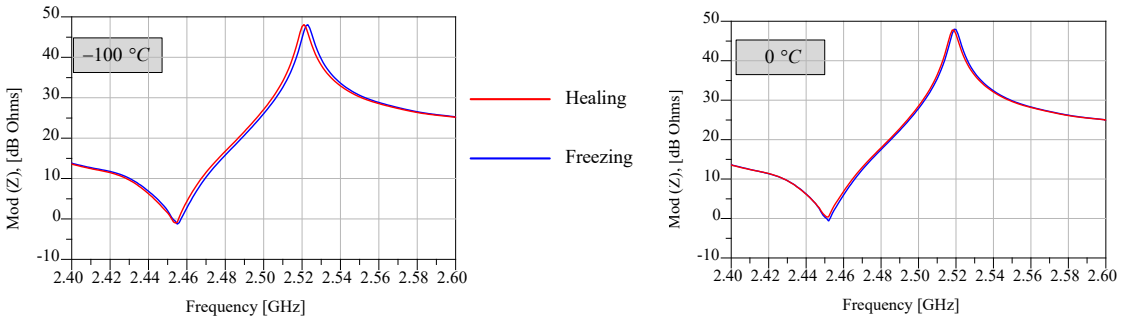

Figure 5. 16. Input impedance of two different temperatures, a) and b) that correspond to -120°C and 0°C, respectively. The red solid lines correspond to the heling cycle and the blue ones corresponds to the freezing cycles.

5.3.3.1. Series and Parallel Resonance frequencies

In Figure 5.17 a) and b) we can see both resonance frequencies as a function of temperature, where a) corresponds to *fs* and b) corresponds to *fp*. The behavior appears to be linear approximately from -120°C up to 130°C. We have made a polynomial fitting to verify this behavior. In both graphs the solid blue line corresponds to this fitting. We can notice that the parallel resonance frequency changes less than the series resonance one. This can be due to the SiO_2 layers in the acoustic reflector that act as a temperature compensator of the TCF.

On the other hand, the extracted data for very low temperatures presents a nonlinear behavior from approximately -170°C up to -120°C. This behavior can be seen in the graphs inside the red solid line ellipses. We have shown these results since they are very interesting issues to study in future works for applications at these cryogenic temperatures. Henceforth, we have decided modelling from -120°C up to 120°C.

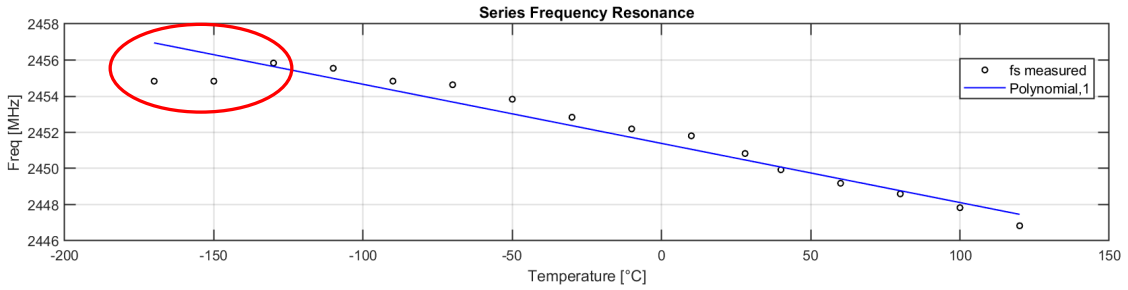

a)

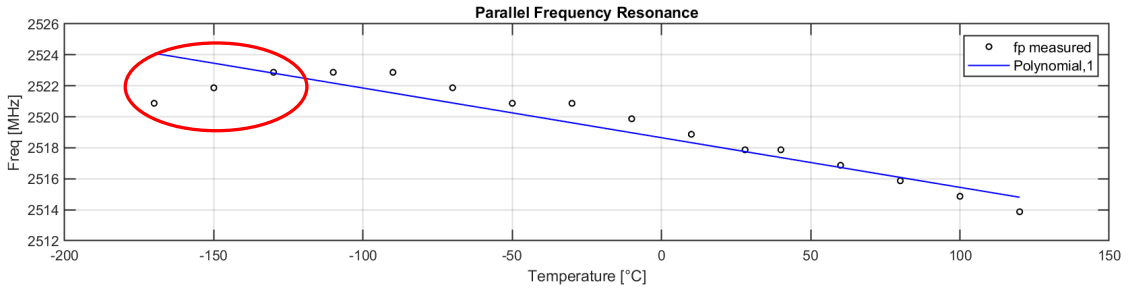

b)

Figure 5. 17. Extracted data measurements and their corresponding fitting curve for both Series and Parallel resonance frequencies, a) and b), respectively. Both frequencies are represented respect to temperature. Measurements are carry out since -170°C up to 130°C. Black circles correspond to data measured, the blue solid line corresponds to a 1-degree polynomial fitting. The data inside the red solid line ellipses is for measurements from -170°C to -130°C.

5.3.3.2. k_{eff}^2 and Quality Factor at Low Temperatures

We have not noticed a special behavior in the effective piezoelectric coupling coefficient since it remains almost constant at 6.0 % for all the temperature range. Fig. 5.18 shows k_{eff}^2 as a function of the temperature for simulated and experimental data. Since this coupling value remains almost constant the quality factor should not vary much either, which is confirm from our results (see Fig. 5.19). Otherwise, at greater values of temperature (greater than 200°C) the quality factor tends to decrease as shown in Figure 5.14. This can be explained since Ohmic, dielectric and acoustic losses increase as temperature does. For instance, the series resistance and dielectric permittivity increase as temperature does, affecting the quality factor, especially its value at the series resonance frequency. This value is important in gravimetric sensing applications since small shifts can induce to misleading quantity measured.

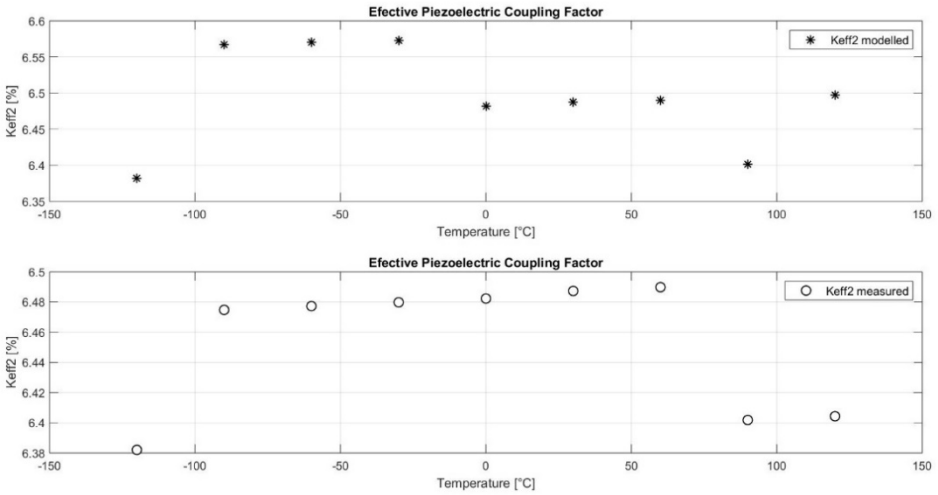

Figure 5. 18. Effective electroacoustic coupling coefficient (Keff2) with respect to the temperature since -120°C up to 130°C. The asterisk markers represent the temperature-dependence mBVD model and the circles are the extracted values from our fabricated solidly mounted resonator.

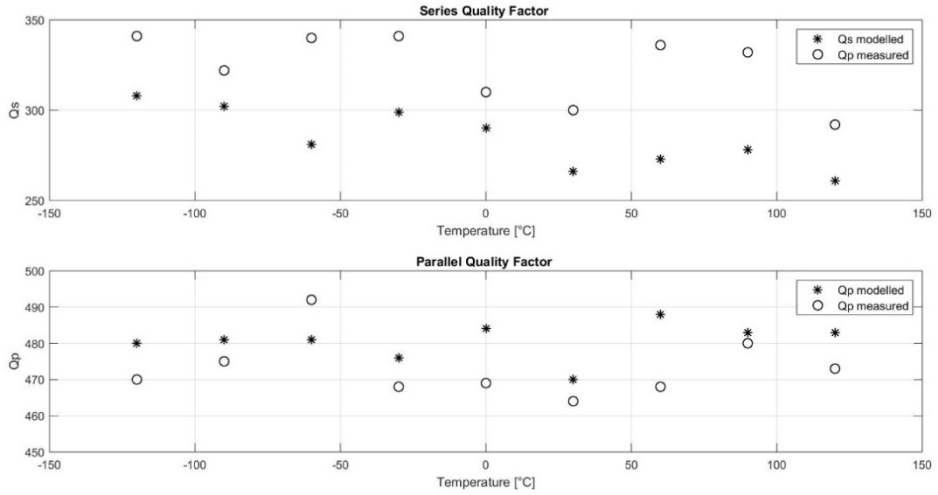

Figure 5. 19. Series and Parallel quality factors, respectively. The data plotted is from -120°C up to 120 °C. The asterisk markers represent the low temperature dependence mBVD model values while the circles represent the extracted from the measurements.

5.3.3.3. Series and Parallel Resonance Frequencies, Modelling and Extracted Data in a Complete Wide Band of Temperature

In this section we present the results for both resonance frequencies (f_s and f_p) for the two analysis in temperature (high and low ones, respectively). The resonators utilized for each analysis are different between each other in their stack configuration, but their active area is equal. In addition, we present results for simulations and extracted data. Figure 5.20 a) and b) show the series and parallel resonances, respectively. The analysis for very low temperatures was carried out from -120°C up to 120°C. On the other hand, the analysis for high temperatures was made from 22°C up to 422°C.

If we check Figure 5.20 a) carefully, which corresponds to the series resonance frequency (*fs*), we can observe that there is data for modelling and measurements in the same graph. For the low temperatures case, the red asterisks correspond to the modelling and the pink solid line squares correspond to the extracted data. Then in the same graph the solid lines with the same color of each marker represent a polynomial fitting (which presents a linear tendency). The red axes are the scale for low temperatures. In addition, in this graph, we can see the corresponding curves for the high temperature analysis. The blue asterisks correspond to modelling and green solid line diamonds correspond to measurements. The solid lines with the same color of each marker represent the polynomial fitting, for modelling and extracted data. The black axes are the scale for high temperature analysis. Finally, the linear fitting of measurements at low and high temperatures, pink and green solid lines, respectively.

Figure 5.20 b) follows the same scheme of a). However, the graph represents the parallel resonance (*fp*). If we analyze the data in the in-set we can notice that the slope of each curve does not change at the same rate, which was expected since resonators and characterization techniques were different (see sections 4.2 and 5.2.3). However, both slopes are negative, which means both resonators have a negative TCF value. We summarize the TCF values for each analysis in temperature in Table 5.7.

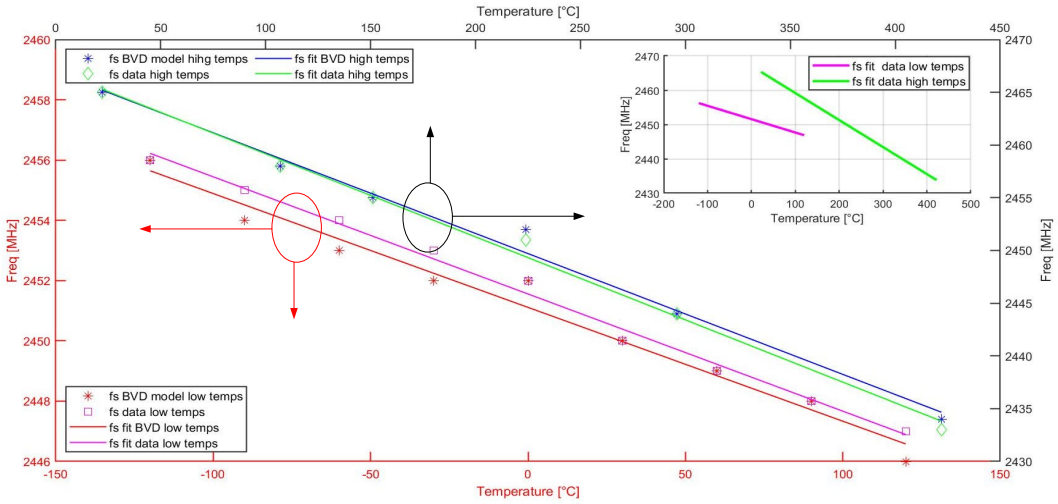

a)

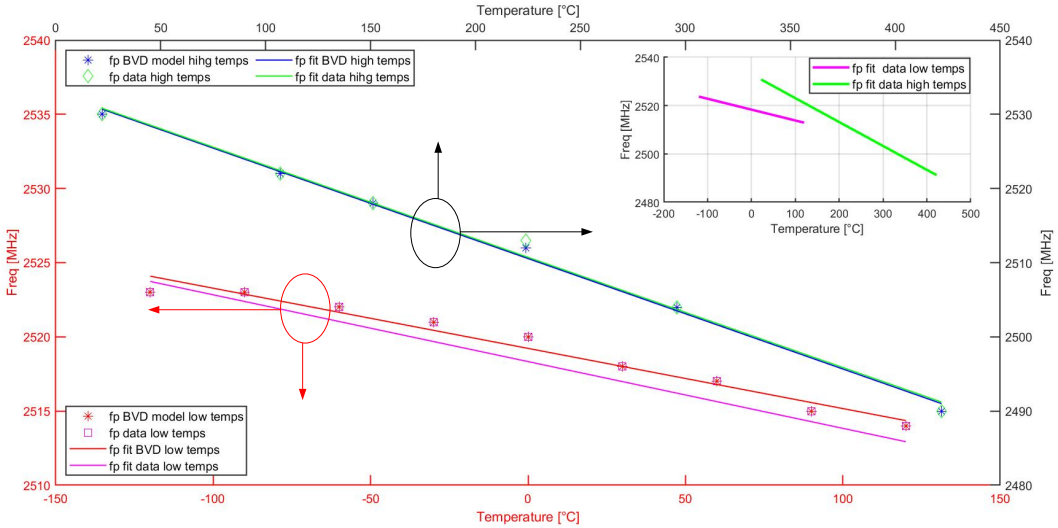

b)

Figure 5. 20. Series and parallel resonance frequencies with respect to temperature. a), corresponds to fs and b) is for fp. The graphs content both analysis in temperature, low and high one, since -120 to 120°C and 22 to 422°C, respectively. Asterisk markers correspond to the mBVD model at low and high temperatures. Then, solid line square and green solid line diamonds are for extracted data at low and high temperatures, respectively. Solid lines, correspond to the polynomial fitting for modelling and measurements. The insets correspond to the measurements fitting, where the pink solid line is for low temperatures while green solid line if for high ones.

We can notice in Figure 5.20 that both resonances for each resonator (low and high temperature analysis) have the same behavior or tendency, negative slope, hence negative TCF. However, the value for each case is different (see Table 5.7). The difference can be due to the configuration of each resonator. In addition, we can see that for high temperatures TCF changes faster than low temperatures.

Table 5. 7. TCF for low and high temperatures, from -120 to 120°C and 22 to 422°C, respectively. There are results for modelling and extracted data from measurements.

TCF [ppm/°C]							
Low-temperatures [-120°C up to 120°C]				**High-temperatures [22°C up to 422°C]**			
mBVD		**DATA**		**mBVD**		**DATA**	
fs	***fp***	***fs***	***fp***	***fs***	***fp***	***fs***	***fp***
-15.54	-17.02	-15.54	-17.02	-31.44	-39.52	-32.45	-39.52

5.3.3.4. Electric Response at Very Low and High Temperatures (-120 to 422°C)

Finally, In Figure 5.21 a), b) and c), we show the input impedance (*Z*), phase of the impedance and the quality factor, respectively. The results are for both resonators, that is the low and high temperature analysis. We have plotted the electrical response for both lowest and highest temperature analysis in order to observe how the series resonance frequency and quality factor were affected. We can see that both values are the most affected at high temperatures. For instance, the series resonance frequency at -120°C is 2,456 GHz and for the highest temperature is 2,434 GHz. They present a difference of 22MHz. In addition, the series quality factor presents a difference of 211. These results are important since we are focused on applications at these temperatures. Henceforth, we have to take into account in future works of these phenomena in the modelling process. In the graphs the solid lines represent data measurements for our two SMRs. The blue one corresponds to the lowest temperature meanwhile the green one is for the highest temperature. The short dash black curve represent the temperature-mBVD modelling.

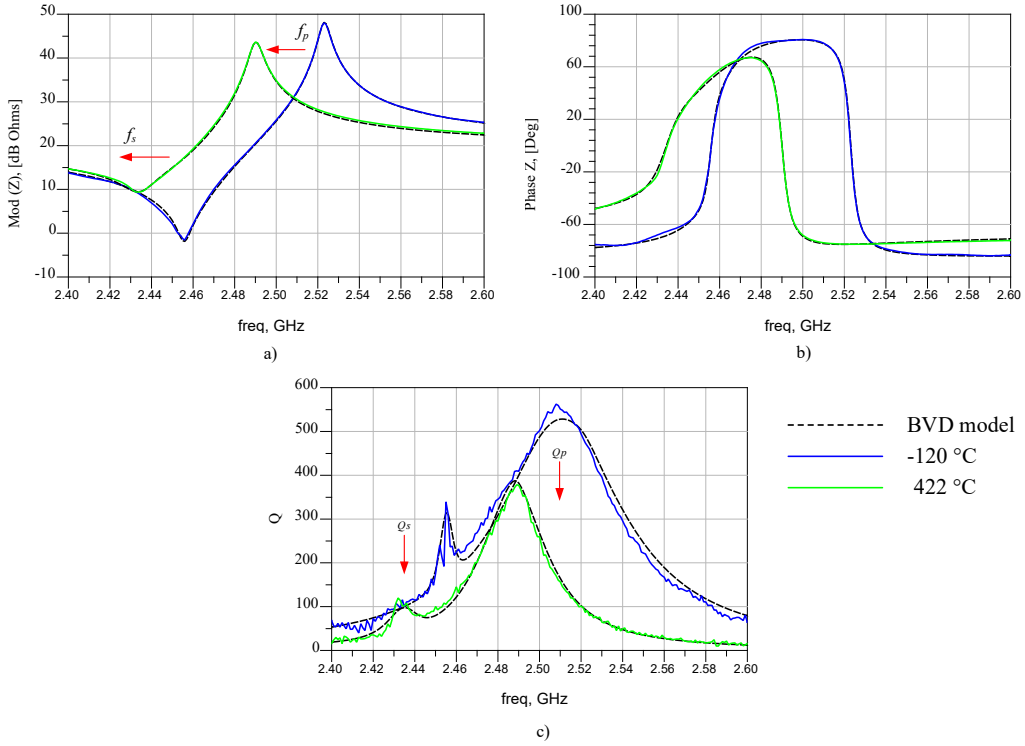

Figure 5. 21. Modelling and measurements for two resonator at two temperatures (-120°C and 422°C). a) corresponds to the input impedance in dBΩ; b) is the input impedance phase and c) corresponds to the Quality factor. Blue curves represent data for -120°C and the green one is for 422°C. The short black dash curve represents the data from updated mBVD model.

5.4. Summary and conclusions

In this chapter, we have presented the comparison between simulations and extracted data for many SMRs based on AlN. These resonators principally operate at 2.5GHz. We have performed two main analysis to our resonators. These scenarios are: the geometry and temperature dependence. The simulations were carried out using our updated version models based on the one-dimensional analysis and electric equivalent circuits.

The first analysis was consisted in the modelling of many resonators at room temperature. The study was performed in order to see how the resonator's geometry and topology affect the performance of the SMRs. Particularly, we have analyzed the size of the active area and also the probing spot. We have probed that both experiments contribute to generate a new resonance that placed so close to the main one. This new resonance clearly affects the series resonance frequency and also the quality factor. Since both parameters are very important outputs in the designing of gravimetric sensors, we have updated our models accordingly in order considerate both effects.

In the second and third parts of the chapter, we have analyzed the temperature dependence of our SMRs by modeling the temperature dependence of the main output parameters that measure their performance. Such parameters are: the $keff^2$, quality factor, both resonance frequencies and also we have included the TCF. In order to carry out our simulations, we have used the updated models and temperature dependence equations seen in section 5.2.2. The complete the analysis we covered a temperature range from -120°C to 422°C. We have validated our models using the extracted data from fabricated SMRs. Final results for TCF, effective electroacoustic coupling coefficient, and quality factor at low temperatures were provided, and a comparison with the high-temperature analysis was included to obtain a wideband response with respect to temperature. Finally, we have proved that our models presents high accuracy and the obtained results are reliable. Our models can be used in order to design SMRs at such temperatures.

Chapter 6

Conclusions and Future Work

As a general conclusion of this research work, we can remark that we have succeeded with the main objective and its different particular objectives. We have successfully updated the one-dimensional and electrical models, and proved both with experimental measurements from fabricated SMRs.

6.1. Conclusions

The principal contribution of this research work consists of updating the two most commonly used models for designing electroacoustic devices, Mason and BVD models. We have modified both models to include various dependencies such as geometry (active area), topology (probing spot), and temperature. The geometrical and topology dependencies are important since we have proved that both affect the performance of the resonator and they contribute to generate a new resonance (new peak). This peak affects the series resonance frequency (*fs*) and quality factor (*Q*). These parameters are important outputs that we have to monitor since they affect directly the response of the resonators, which can distort the data reading in sensing applications. Henceforth, the first update in our models was to include the geometry and topology dependencies to model this resonance. The modification of the models consisted of adding a new branch connected in parallel to the main resonance; this resonance is coupled capacitively. This new resonator allowed us to model this new peak accurately. In addition, we have learned that the size of the active area in our configuration (SMRs) has a limit. In other words, the larger areas highly contribute to generate this peak. Further, the place of the probing spot also contributes to the generation of this new peak. Henceforth, we must consider a relation between the size of the active area and the probing spot when we design new devices in order to avoid disturbances in the response of our SMRs. To improve the accuracy of the models, we have made simulations by means of mBVD model and then use them as inputs in the Mason's model. This tool also takes into account the physical properties of the whole stack of the resonator, which results in high accuracy models.

In addition to the first modification, we have presented results of a second modification in the models, which consists of adding the temperature variations as a new input. This new

modification relays on receiving as an input the temperature dependence values computed by our programmed tool. The main temperature dependence values are: thickness (d), active area (A) and permittivity (ε). By means of these updated versions, we have modelled several resonators at very low and high temperatures (-120° to 422°C). Two resonators with different configurations were modelled in a different band of temperatures. First, we have presented our modelling for high temperatures, which was carried out from room temperature up to 422°C. The modelling was validated with experimental measurements. We have proved that our models present high accuracy at such temperatures. Secondly, we have presented data for very low temperatures, from -120°C up to 120°C, again with excellent agreement with experimental data.

The most important performance parameters used to evaluate the quality and effectiveness of SMRs were presented in this work in order to understand how they affect the response of the resonators, hence how they could affect the response of gravimetric sensors at extreme temperatures. For instance, the series resonance frequency tell us how the temperature affects it, so we can compute the temperature coefficient of frequency (TCF), which is another FOM. For our resonators, the tendency of the TCF is negative. Both values are key parameters in the designing of gravimetric sensors since they are directly related with sensitivity. On the other hand, we have modelled the quality factor (Q) and the effective piezoelectric coupling coefficient (k_{eff}^2).These are apparently not so affected at very low temperatures, in contrast to their values above 200°C. This can be explained by Ohmic, dielectric and mechanical losses due to increments in temperature. Finally, we have carried out measurements below -120°C and noticed that performance appears to be nonlinear. However, in this thesis we have not considered these values in our simulations since applications at these temperatures are not part of this investigation. Summarizing, we are able to design SMRs by means of our modified models for applications in harsh environments.

The second contribution of this work was the establishment (setup) of the semiautomatic probe tips measurements (cryogenic station). This system was updated in order to characterize our SMRs at cryogenic temperatures (-170°C to 200°C). We have modified and updated this system to extract the Scattering parameters in a semi-automatic way. This task was carried out to reduce the time and effort of characterization process. Part of this update was made during this thesis, however, the signal theory and communications research group has been working for the past years on the system. The last contribution was the establishment of a methodology to carry out measurements in the semiautomatic probes measurements. This was necessary since the operation of the whole system by itself is a complicated task. Furthermore, since we wanted repeatability in our measurements, this methodology protocol was strictly necessary.

6.2. Future Work

The achievements of this thesis are the starting point for the design and manufacture of a new generation of SMRs taking into account the geometry, topology and temperature inputs. Further, an automatic methodology to characterize resonators at very low temperatures are still needed. Therefore, the proposed future developments are:

1. Since we have identified that the size of the active area of the resonators directly affects the series resonance frequency, we propose the modelling, fabrication and characterization of such resonators with the adequate area. In addition, as the pad of characterization has an influence on this resonance frequency, a good experiment will be to fabricate resonators with shorter pads without compromising the impedance.

2. We propose the development of an automatic methodology process to take measurements in our probe tips measurements. This work is necessary since each attempt to measure a device takes a significant amount of time. Additionally, each measurement that has a human intervention has more probability of errors, which is reflected in the results. This can be reached by means of developing an adequate piece of software that interconnects the whole modules in one graphical interface.

3. Investigate deeply the behavior of our SMRs at very low temperatures, since the special applications are growing very rapidly. For instance, in the last years, there have been more and more space missions of exploration. Additionally, models at such temperatures are needed, specially the basic one dimensional ones.

4. Finally, we propose to fabricate more gravimetric sensors for harsh environments using our developed technology.

Appendix A

List of Contributions

The development of this Ph.D. thesis has contributed to the design, modelling, fabrication and characterization of SMRs in extreme environments. Furthermore, this thesis was part of the next research projects: “Materiales para resonadores electro-acústicos y sensores para futuras aplicaciones sub-6GHz 5G - EAD5G (TEC2017-84817-C2-1-R)” and “Sensores gravimétricos de gases basados en resonadores electro-acústicos de película delgada de AlN para aplicaciones en temperaturas extremas (PID-2020-118410RB-C22)”.

A.1. Research Contributions

The novels of this Ph.D. thesis have been published in some research contributions. The total number of publications is 1 journal paper and 3 conference papers.

Journal Papers

E. Lugo-Hernández et al., “Analysis of spurious peaks at series resonance in solidly mounted resonators by combined BVD-Mason modelling,” Ultrasonics, vol. 131, p. 106958, May 2023, doi: 10.1016/j.ultras.2023.106958.

Conference Papers

E. Lugo-Hernandez, C. Collado, J. Mateu, J. M. Carmona-Cejas, T. Mirea, and J. Olivares, “Updated BVD Modeling of AlN-based Solidly Mounted Resonators Working at Cryogenic and High Temperatures : From −160 °C up to 130 °C,” in *2022 Joint Conference of the European Frequency and Time Forum and IEEE International Frequency Control Symposium (EFTF/IFCS)*, Apr. 2022, pp. 1–2, doi: 10.1109/EFTF/IFCS54560.2022.9850489.

E. Lugo-Hernandez et al., “High temperatures BVD model for AlN-based solidly mounted resonators,” in 2021 IEEE International Ultrasonics Symposium (IUS), Sep. 2021, pp. 1–3, doi: 10.1109/IUS52206.2021.9593400

E. Lugo-Hernandez et al., “Modified Mason’s and BVD Models For Analysis Of Spurious Modes Due To Ohmic Losses in BAW Resonators,” in 2021 Joint Conference of the European

Frequency and Time Forum and IEEE International Frequency Control Symposium (EFTF/IFCS), Jul. 2021, pp. 1–3, doi: 10.1109/EFTF/IFCS52194.2021.9604279.

A.2. Academic Contributions

During this Ph.D. I have made a research visit in Mexico of five moths (february first to june 30th, 2022) under the "*Erasmus + Eduacation para estudios superiores entre países del programa. Accion Clave KA107*" program. The results of this visit are: the codirection of 1 bachelor's degree final work and a webinar imparted at the Instituto Politécnico Nacional.

Bachelor's Degree Final Work

A. Ramirez and M. Flores, "*Modelado comparativo en altas frecuencias usando diferentes programas de diseño asistido por computadora*" Advisors: Luis Manuel Rodriguez Méndez, E. Lugo-Hernández, July 2022.

Seminar

E. Lugo-Hernández, "*Resonadores electro-acústicos de película delgada para comunicaciones inalámbricas móviles*", Mexico city, Instituto Politécnico Nacional, June 30th, 2022.

Bibliography

[1] J. Tsutsumi, M. Seth, A. S. Morris III, R. B. Staszewski, and G. Hueber, "Cost-Efficient, High-Volume Transmission: Advanced Transmission Design and Architecture of Next Generation RF Modems and Front-Ends," *IEEE Microw. Mag.*, vol. 16, no. 7, pp. 26–45, Aug. 2015, doi: 10.1109/MMM.2015.2431235.

[2] P. Warder and A. Link, "Golden Age for Filter Design: Innovative and Proven Approaches for Acoustic Filter, Duplexer, and Multiplexer Design," *IEEE Microw. Mag.*, vol. 16, no. 7, pp. 60–72, Aug. 2015, doi: 10.1109/MMM.2015.2431236.

[3] A. Volatier, B. Dubus, and D. Ekeom, "P1J-7 Solidly Mounted Resonator (SMR) FEM-BEM Simulation," in *2006 IEEE Ultrasonics Symposium*, 2006, pp. 1474–1477, doi: 10.1109/ULTSYM.2006.371.

[4] T. Bauer, C. Eggs, K. Wagner, and P. Hagn, "A Bright Outlook for Acoustic Filtering: A New Generation of Very Low-Profile SAW, TC SAW, and BAW Devices for Module Integration," *IEEE Microw. Mag.*, vol. 16, no. 7, pp. 73–81, Aug. 2015, doi: 10.1109/MMM.2015.2429512.

[5] F. Bi and B. Barber, "Bulk acoustic wave RF technology," *IEEE Microw. Mag.*, vol. 9, no. 5, pp. 65–80, Oct. 2008, doi: 10.1109/MMM.2008.927633.

[6] K. M. Lakin, G. R. Kline, and K. T. McCarron, "Thin film bulk acoustic wave filters for GPS," in *IEEE 1992 Ultrasonics Symposium Proceedings*, 1992, pp. 471–476, doi: 10.1109/ULTSYM.1992.275963.

[7] H. Campanella Pineda, "Thin- film bulk acoustic wave resonators (FBAR), fabrication, heterogeneous integration with CMOS technologies and sensors applications," Université de Montpellier II (UM2) and Universitat Autònoma de Barcelona (UAB), 2007.

[8] A. Mujahid, A. Afzal, and F. L. Dickert, "An Overview of High Frequency Acoustic Sensors—QCMs, SAWs and FBARs—Chemical and Biochemical Applications," *Sensors*, vol. 19, no. 20, p. 4395, Oct. 2019, doi: 10.3390/s19204395.

[9] T. Mirea, "Thin film electroacoustic resonators for physical and chemical sensing," Universidad Politécnica de Madrid, 2017.

[10] F. H. Villa Lopez, G. Rughoobur, S. Thomas, A. Flewitt, M. Cole, and J. W. Gardner, "Design and Modelling of Solidly-Mounted Resonators for Low-Cost Particle Sensing," *Meas. Sci. Technol.*, vol. 27, Dec. 2015, doi: 10.1088/0957-0233/27/2/025101.

[11] M. de M. Ramos, "High sensitivity biosensors based on shear mode AlN resonators for in liquid operation," Universidad Politecnica de Madrid, 2015.

[12] S. Rey-Mermet, R. Lanz, and P. Muralt, "Bulk acoustic wave resonator operating at 8GHz for gravimetric sensing of organic films," *Sensors Actuators B Chem.*, vol. 114, no. 2, pp. 681–686, Apr. 2006, doi: 10.1016/j.snb.2005.04.047.

[13] M. Nirschl, D. Sickert, O. Karaca, M. Schreiter, and J. Voros, "Frequency Response of Thin-Film Bulk Acoustic Resonators to the Deposition of Tungsten, Platinum, Aluminium Oxide and Carbon Nanotube Thin-Films," *Micro Nanosyst.*, vol. 4, no. 2, pp. 111–117, May 2012, doi: 10.2174/1876402911204020111.

[14] K. M. Lakin, "Review of the thin film resonator technology," in *Proceedings - 2003 IEEE Radio and Wireless Conference, RAWCON 2003*, 2003, pp. 333–336, doi: 10.1109/RAWCON.2003.1227960.

[15] M. Hara, T. Yokoyama, M. Ueda, and Y. Satoh, "12E-2 X-Band Filters Utilizing AlN Thin Film Bulk Acoustic Resonators," in *2007 IEEE Ultrasonics Symposium Proceedings*, Oct. 2007, pp. 1152–1155, doi: 10.1109/ULTSYM.2007.291.

[16] S.-H. Lee, K. H. Yoon, and J.-K. Lee, "Influence of electrode configurations on the quality factor and piezoelectric coupling constant of solidly mounted bulk acoustic wave resonators," *J. Appl. Phys.*, vol. 92, no. 7, pp. 4062–4069, Oct. 2002, doi: 10.1063/1.1505977.

[17] N. Nguyen, A. Johannessen, S. Rooth, and U. Hanke, "The impact of area on BAW resonator performance and an approach to device miniaturization," *Ultrasonics*, vol. 94, pp. 92–101, Apr. 2019, doi: 10.1016/j.ultras.2018.11.014.

[18] R. Thalhammer, G. Fattinger, M. Handtmann, and S. Marksteiner, "Ohmic effects in BAW-resonators," *IEEE MTT-S Int. Microw. Symp. Dig.*, pp. 390–393, 2006, doi: 10.1109/MWSYM.2006.249552.

[19] W. P. Mason, *Electromechanical transducers and wave filters*. Princeton NJ, 1948.

[20] S. Butterworth, "On Electrically-maintained Vibrations," *Proc. Phys. Soc. London*, vol. 27, no. 1, pp. 410–424, Dec. 1914, doi: 10.1088/1478-7814/27/1/330.

[21] K. S. Van Dyke, "The Piezo-Electric Resonator and Its Equivalent Network," *Proc. IRE*,

vol. 16, no. 6, pp. 742–764, Jun. 1928, doi: 10.1109/JRPROC.1928.221466.

[22] P. Songsukthawan and C. Jettanasen, “Generation and storage of electrical energy from piezoelectric materials,” in *2017 IEEE 3rd International Future Energy Electronics Conference and ECCE Asia (IFEEC 2017 - ECCE Asia)*, Jun. 2017, pp. 2256–2259, doi: 10.1109/IFEEC.2017.7992403.

[23] H. Ken-ya, *RF Bulk Acoustic Wave Filters for Communications*. Artech House, 2009.

[24] R. Weigel *et al.*, “Microwave acoustic materials, devices, and applications,” *IEEE Trans. Microw. Theory Tech.*, vol. 50, no. 3, pp. 738–749, Mar. 2002, doi: 10.1109/22.989958.

[25] Z. Nazarchuk, V. Skalskyi, and O. Serhiyenko, *Acoustic Emission Methodology and Application*, 1st ed. 20. 2017.

[26] S. J. Martin, A. J. Ricco, T. M. Niemczyk, and G. C. Frye, “Characterization of SH acoustic plate mode liquid sensors,” *Sensors and Actuators*, vol. 20, no. 3, pp. 253–268, Dec. 1989, doi: 10.1016/0250-6874(89)80124-6.

[27] R. M. White, P. J. Wicher, S. W. Wenzel, and E. T. Zellers, “Plate-Mode Ultrasonic Oscillator Sensors,” *IEEE Trans. Ultrason. Ferroelectr. Freq. Control*, vol. 34, no. 2, pp. 162–171, Mar. 1987, doi: 10.1109/T-UFFC.1987.26928.

[28] C. T. Chuang and R. M. White, “Excitation and Propagation of Plate Modes in an Acoustically-Thin Membrane,” in *1982 Ultrasonics Symposium*, 1982, vol. 1, pp. 295–298, doi: 10.1109/ULTSYM.1982.197832.

[29] S. McHugh, P. J. Turner, V. Yantchev, and V. Plessky, “Lamb plate modes and surface acoustic wave resonator microwave filters,” in *2015 IEEE International Ultrasonics Symposium (IUS)*, Oct. 2015, pp. 1–4, doi: 10.1109/ULTSYM.2015.0058.

[30] D. Morgan, *Acoustic Wave Filters*, Second. y Elsevier Ltd., 2007.

[31] S. Hohmann *et al.*, “Surface Acoustic Wave (SAW) Resonators for Monitoring Conditioning Film Formation,” *Sensors*, vol. 15, no. 5, pp. 11873–11888, May 2015, doi: 10.3390/s150511873.

[32] C. K. O’Sullivan and G. G. Guilbault, “Commercial quartz crystal microbalances – theory and applications,” *Biosens. Bioelectron.*, vol. 14, no. 8–9, pp. 663–670, Dec. 1999, doi: 10.1016/S0956-5663(99)00040-8.

[33] S. K. Vashist and P. Vashist, “Recent Advances in Quartz Crystal Microbalance-Based Sensors,” *J. Sensors*, vol. 2011, pp. 1–13, 2011, doi: 10.1155/2011/571405.

[34] G. Sauerbrey, “Verwendung von Schwingquarzen zur Wägung dünner Schichten und zur Mikrowägung,” *Zeitschrift für Phys.*, vol. 155, no. 2, pp. 206–222, Apr. 1959, doi: 10.1007/BF01337937.

[35] G. S. Huang, M.-T. Wang, C.-W. Su, Y.-S. Chen, and M.-Y. Hong, “Picogram detection of metal ions by melanin-sensitized piezoelectric sensor,” *Biosens. Bioelectron.*, vol. 23, no. 3, pp. 319–325, Oct. 2007, doi: 10.1016/j.bios.2007.04.011.

[36] C. R. Kirkendall and Jae Wan Kwon, “Sub-picogram resolution mass sensing in a liquid environment using low-loss quartz crystal microbalance,” in *2010 IEEE Sensors*, Nov. 2010, pp. 1783–1786, doi: 10.1109/ICSENS.2010.5689974.

[37] K. K. Kanazawa and J. G. Gordon, “Frequency of a quartz microbalance in contact with liquid,” *Anal. Chem.*, vol. 57, no. 8, pp. 1770–1771, Jul. 1985, doi: 10.1021/ac00285a062.

[38] M. Rodahl, F. Höök, A. Krozer, P. Brzezinski, and B. Kasemo, “Quartz crystal microbalance setup for frequency and Q -factor measurements in gaseous and liquid environments,” *Rev. Sci. Instrum.*, vol. 66, no. 7, pp. 3924–3930, Jul. 1995, doi: 10.1063/1.1145396.

[39] A. Arnau, “A Review of Interface Electronic Systems for AT-cut Quartz Crystal Microbalance Applications in Liquids,” *Sensors*, vol. 8, no. 1, pp. 370–411, Jan. 2008, doi: 10.3390/s8010370.

[40] V. M. Mecea, “From Quartz Crystal Microbalance to Fundamental Principles of Mass Measurements,” *Anal. Lett.*, vol. 38, no. 5, pp. 753–767, Mar. 2005, doi: 10.1081/AL-200056171.

[41] H. He *et al.*, “Detection of trace microcystin-LR on a 20 MHz QCM sensor coated with in situ self-assembled MIPs,” *Talanta*, vol. 131, pp. 8–13, 2015, doi: 10.1016/j.talanta.2014.07.071.

[42] M. Rodahl *et al.*, “Simultaneous frequency and dissipation factor QCM measurements of biomolecular adsorption and cell adhesion,” *Faraday Discuss.*, vol. 107, pp. 229–246, 1997, doi: 10.1039/a703137h.

[43] D. A. Buttry and M. D. Ward, “Measurement of interfacial processes at electrode surfaces with the electrochemical quartz crystal microbalance,” *Chem. Rev.*, vol. 92, no. 6, pp. 1355–1379, Sep. 1992, doi: 10.1021/cr00014a006.

[44] D. Migoń, T. Wasilewski, and D. Suchy, “Application of QCM in Peptide and Protein-Based Drug Product Development,” *Molecules*, vol. 25, no. 17, p. 3950, Aug. 2020, doi:

10.3390/molecules25173950.

[45] I. A. Blech, “Electromigration in thin aluminum films on titanium nitride,” *J. Appl. Phys.*, vol. 47, no. 4, pp. 1203–1208, Apr. 1976, doi: 10.1063/1.322842.

[46] C. Ruppel, “Advances in Surface Acoustic Wave Technology, Systems and Applications,” *Int. J. High Speed Electron. Syst.*, vol. 10, no. 3, pp. iii–iv, Sep. 2000, doi: 10.1016/S0129-1564(00)00058-1.

[47] K. M. Lakin, “A review of thin-film resonator technology,” *IEEE Microw. Mag.*, vol. 4, no. 4, pp. 61–67, Dec. 2003, doi: 10.1109/MMW.2003.1266067.

[48] V. Felmetsger, “Sputter technique for deposition of AlN and ScAlN thin films in mass production,” in *2017 IEEE International Ultrasonics Symposium (IUS)*, Sep. 2017, pp. 1–1, doi: 10.1109/ULTSYM.2017.8092605.

[49] Y. Oshmyansky, J. D. Larson, R. Ruby, and S. Mishin, “Sputtering Processes for Bulk Acoustic Wave Filters,” *Semiconductor.net*, no. 805, 2002.

[50] K. M. Lakin and J. S. Wang, “Acoustic bulk wave composite resonators,” *Appl. Phys. Lett.*, vol. 38, no. 3, pp. 125–127, Feb. 1981, doi: 10.1063/1.92298.

[51] T. W. Grudkowski, J. F. Black, T. M. Reeder, D. E. Cullen, and R. A. Wagner, “Fundamental-mode VHF/UHF minature acoustic resonators and filters on silicon,” *Appl. Phys. Lett.*, vol. 37, no. 11, pp. 993–995, Dec. 1980, doi: 10.1063/1.91745.

[52] K. Nakamura, H. Sasaki, and H. Shimizu, “ZnO/SiO2-diaphragm composite resonator on a silicon wafer,” *Electron. Lett.*, vol. 17, no. 14, p. 507, 1981, doi: 10.1049/el:19810355.

[53] M. E. Marin, F. Constantinescu, O. S. Taus, and A. G. Gheorghe, “Intermodulation products in AlN power BAW duplexer filters,” in *2017 International Symposium on Signals, Circuits and Systems (ISSCS)*, Jul. 2017, vol. 6, no. July, pp. 1–4, doi: 10.1109/ISSCS.2017.8034949.

[54] G. F. Iriarte, J. G. Rodríguez, and F. Calle, “Synthesis of c-axis oriented AlN thin films on different substrates: A review,” *Mater. Res. Bull.*, vol. 45, no. 9, pp. 1039–1045, Sep. 2010, doi: 10.1016/j.materresbull.2010.05.035.

[55] M.-A. Dubois and P. Muralt, “Properties of aluminum nitride thin films for piezoelectric transducers and microwave filter applications,” *Appl. Phys. Lett.*, vol. 74, no. 20, pp. 3032–3034, May 1999, doi: 10.1063/1.124055.

[56] V. R. Pagan, “Aluminum nitride deposition / characterization & pMEMs / SAW device

simulation / fabrication," Morgantown, West Virginia, 2009.

[57] C.-M. Lin, "Temperature-Compensated and High-Q Piezoelectric Aluminum Nitride Lamb Wave Resonators for Timing and Frequency Control Applications," UC Berkeley, 2013.

[58] B. Ivira, P. Benech, R. Fillit, F. Ndagijimana, P. Ancey, and G. Parat, "Modeling for temperature compensation and temperature characterizations of BAW resonators at GHz frequencies," *IEEE Trans. Ultrason. Ferroelectr. Freq. Control*, vol. 55, no. 2, pp. 421–430, Feb. 2008, doi: 10.1109/TUFFC.2008.660.

[59] C. M. Lueng, H. L. W. Chan, C. Surya, and C. L. Choy, "Piezoelectric coefficient of aluminum nitride and gallium nitride," *J. Appl. Phys.*, vol. 88, no. 9, pp. 5360–5363, Nov. 2000, doi: 10.1063/1.1317244.

[60] G. Carlotti, F. S. Hickernell, H. M. Liaw, L. Palmieri, G. Socino, and E. Verona, "The elastic constants of sputtered aluminum nitride films," in *1995 IEEE Ultrasonics Symposium. Proceedings. An International Symposium*, 1995, vol. 1, pp. 353–356, doi: 10.1109/ULTSYM.1995.495597.

[61] S. Song *et al.*, "Film bulk acoustic formaldehyde sensor with polyethyleneimine-modified single-wall carbon nanotubes as sensitive layer," *Sensors Actuators, B Chem.*, vol. 266, pp. 204–212, 2018, doi: 10.1016/j.snb.2018.03.129.

[62] N. I. . Nor *et al.*, "Film bulk acoustic wave resonator in 10–20 GHz frequency range," in *2016 3rd International Conference on Electronic Design (ICED)*, Aug. 2016, no. August, pp. 481–485, doi: 10.1109/ICED.2016.7804692.

[63] G. Wingqvist, "AlN-based sputter-deposited shear mode thin film bulk acoustic resonator (FBAR) for biosensor applications — A review," *Surf. Coatings Technol.*, vol. 205, no. 5, pp. 1279–1286, Nov. 2010, doi: 10.1016/j.surfcoat.2010.08.109.

[64] M. Teona, J. Olivares, M. Clement, J. Sangrador, and E. Iborra, "AlN-based solidly mounted resonators on glass substrates for high temperature applications," in *2018 IEEE International Ultrasonics Symposium (IUS)*, pp. 5–8, doi: 10.1109/ULTSYM.2018.8579966.

[65] B. Ivira *et al.*, "Solidly mounted resonators aging under harsh environmental conditions," *J. Phys. Conf. Ser.*, vol. 34, pp. 668–673, Apr. 2006, doi: 10.1088/1742-6596/34/1/110.

[66] T. Mirea *et al.*, "AlN Solidly Mounted Resonators for High Temperature Applications," in *IEEE International Ultrasonics Symposium, IUS*, 2014, pp. 1524–1527, doi:

10.1109/ULTSYM.2014.0377.

[67] T. Aubert *et al.*, “In situ high-temperature characterization of AlN-based surface acoustic wave devices,” *J. Appl. Phys.*, vol. 114, no. 1, 2013, doi: 10.1063/1.4812565.

[68] M. Pereira da Cunha *et al.*, “Recent advances in harsh environment acoustic wave sensors for contemporary applications,” in *2011 IEEE SENSORS Proceedings*, Oct. 2011, pp. 614–617, doi: 10.1109/ICSENS.2011.6126948.

[69] B. Wall, R. Gruenwald, M. Klein, and G. Bruckner, “C3.3 - A 600°C Wireless and Passive Temperature Sensor Based on Langasite SAW-Resonators,” in *Proceedings SENSOR 2015*, 2015, pp. 390–395, doi: 10.5162/sensor2015/C3.3.

[70] J. A. Thiele and M. Pereira Da Cunha, “High Temperature LGS SAW devices with Pt/WO3 and Pd Sensing Films,” in *Proceedings of the IEEE Ultrasonics Symposium*, 2003, pp. 1750–1753, doi: 10.1109/ultsym.2003.1293250.

[71] J. Streque *et al.*, “Design and Characterization of High-Q SAW Resonators Based on the AlN/Sapphire Structure Intended for High-Temperature Wireless Sensor Applications,” *IEEE Sens. J.*, vol. 20, no. 13, pp. 6985–6991, Jul. 2020, doi: 10.1109/JSEN.2020.2978179.

[72] D. W. Greve, T. L. Chin, P. Zheng, P. Ohodnicki, J. Baltrus, and I. J. Oppenheim, “Surface Acoustic Wave Devices for Harsh Environment Wireless Sensing,” *Sensors (Switzerland)*, vol. 13, no. 6, pp. 6910–6935, 2013, doi: 10.3390/s130606910.

[73] W. P. Mason and R. N. Thurston, *Physical Acoustics: Principles and Methods*, no. v. 15. Academic Press, 1981.

[74] E. Rocas, C. Collado, J. Mateu, N. Orloff, J. Booth, and R. Aigner, “Electro-thermo-mechanical model for bulk acoustic wave resonators,” *IEEE Trans. Ultrason. Ferroelectr. Freq. Control*, vol. 60, no. 11, pp. 2389–2403, Nov. 2013, doi: 10.1109/TUFFC.2013.6644742.

[75] J. F. Rosenbaum, *Bulk Acoustic Wave Theory and Devices*, Ilustrated. Boston: Artech House, 1988.

[76] D. ROYER, D. P. Morgan, and E. Dieulesaint, *Elastic Waves in Solids I: Free and Guided Propagation*. Springer Berlin Heidelberg, 2010.

[77] D. ROYER, S. N. Lyle, and E. Dieulesaint, *Elastic Waves in Solids II: Generation, Acousto-optic Interaction, Applications*. Springer Berlin Heidelberg, 1999.

[78] E. Rocas *et al.*, “Performance of BAW resonators at cryogenic temperatures,” in *2013*

IEEE International Ultrasonics Symposium (IUS), Jul. 2013, pp. 1672–1675, doi: 10.1109/ULTSYM.2013.0426.

[79] B. A. Auld, *Acoustic Fields and Waves in Solids, V.1*. John Wiley \& Sons, 1973.

[80] R. Hooke, *Lectures de Potentia Restitutiva*, 1678th ed. 1678.

[81] J. Verdú, "Bulk Acoustic Wave Resonators and their Application to Microwave Devices," Autonomous university of Barcelona, 2010.

[82] D. M. Pozar, *Microwave engineering*, 4th ed. University of Massachusetts at Amherst: Hoboken, NJ : Wiley, [2012] ©2012.

[83] W. P. Mason, *Piezoelectric Crystals and Their Application to Ultrasonics*. Van Nostrand, 1950.

[84] J. D. Larson, P. D. Bradley, S. Wartenberg, and R. C. Ruby, "Modified Butterworth-Van Dyke circuit for FBAR resonators and automated measurement system," in *2000 IEEE Ultrasonics Symposium. Proceedings. An International Symposium (Cat. No.00CH37121)*, 2000, pp. 863–868 vol.1, doi: 10.1109/ULTSYM.2000.922679.

[85] D. A. Feld, R. Parker, R. Ruby, P. Bradley, and S. Dong, "After 60 years: A new formula for computing quality factor is warranted," in *2008 IEEE Ultrasonics Symposium*, Nov. 2008, pp. 431–436, doi: 10.1109/ULTSYM.2008.0105.

[86] A. American and N. Standard, "IEEE Standard on Piezoelectricity," *IEEE Trans. Sonics Ultrason.*, vol. 31, no. 2, Mar. 1984, doi: 10.1109/T-SU.1984.31464.

[87] E. Lugo-Hernández *et al.*, "Analysis of spurious peaks at series resonance in solidly mounted resonators by combined BVD-Mason modelling," *Ultrasonics*, vol. 131, p. 106958, May 2023, doi: 10.1016/j.ultras.2023.106958.

[88] R. Thalhammer, G. Fattinger, M. Handtmann, and S. Marksteiner, "Ohmic effects in BAW-resonators," in *2006 IEEE MTT-S International Microwave Symposium Digest*, Jun. 2006, pp. 390–393, doi: 10.1109/MWSYM.2006.249552.

[89] R. Krimholtz, D. A. Leedom, and G. L. Matthaei, "New equivalent circuits for elementary piezoelectric transducers," *Electron. Lett.*, vol. 6, no. 13, p. 398, 1970, doi: 10.1049/el:19700280.

[90] A. Technologies, "Advanced Design System 2011.01-Data Display," 2011.

[91] T. D. E. L. Tfg and M. Gonz, "Trabajofinal de grado," 2018.

[92] K. J. Lesker, "Box Chambers."

https://www.lesker.com/newweb/chambers/std_boxchamber.cfm (accessed May 09, 2020).

[93] IDS, “Cameras, uEye CP.” https://en.ids-imaging.com/store/products/cameras/ids-interface-group/usb-3/ids-family/cp.html (accessed Sep. 05, 2020).

[94] “Zoom Precision Lens 12.5 X.” https://www.edmundoptics.com/imaging/imaging-lenses/zoom-lenses/12x-precision-zoom-lens/2872.

[95] I. INSTEC, “Densign concept for INS1211063,” 2013.

[96] Honywell, “Thin Film Platinum RTDs, HEL-700 Series,” *Douglas, USA*. Golden Valley, MN, USA, p. 6, 2014, [Online]. Available: sensing.honeywell.com.

[97] R. & SCHWARZ, “Programmable LCR-Bridge (HM8118). User Manual.” ROHDE & SCHWARZ, p. 75, [Online]. Available: www.rohde-schwarz.com Customer.

[98] ROHDE & SCHWARZ, “Digital Multimeter (HMC8012). User Manual.” ROHDE & SCHWARZ, p. 66, [Online]. Available: www.rohde-schwarz.com.

[99] FORM FACTOR, “Probe Selection Guide.” FORM FACTOR, Livermore, CA, USA, p. 49, 2021, [Online]. Available: https://www.formfactor.com/.

[100] Pfeiffer, *The Vacuum Technology*, vol. II. Pfeiffer Vacuum GmbH, 2013.

[101] FORMFACTOR, “Quick Reference Guide |Z| Probe.” Livermore, CA, USA, p. 2, [Online]. Available: www.formfactor.com.

[102] T. P. INC, “PELCO, High Performance Silver Paste.” PELCO, USA, p. 2, [Online]. Available: http://www.tedpella.com.

[103] T. Makkonen, A. Holappa, J. Ella, and M. M. Salomea, “Finite element simulations of thin-film composite BAW resonators,” *IEEE Trans. Ultrason. Ferroelectr. Freq. Control*, vol. 48, no. 5, pp. 1241–1258, Sep. 2001, doi: 10.1109/58.949733.

[104] H. Campanella, E. Martincic, P. Nouet, A. Uranga, and J. Esteve, “Analytical and Finite-Element Modeling of Localized-Mass Sensitivity of Thin-Film Bulk Acoustic-Wave Resonators (FBAR),” *IEEE Sens. J.*, vol. 9, no. 8, pp. 892–901, Aug. 2009, doi: 10.1109/JSEN.2009.2024858.

[105] Z. D. Schwartz, A. N. Downey, S. A. Alterovitz, and G. E. Ponchak, “High-Temperature RF Probe Station for Device Characterization Through 500 °C and 50 GHz,” *IEEE Trans. Instrum. Meas.*, vol. 54, no. 1, pp. 369–376, Feb. 2005, doi: 10.1109/TIM.2004.838137.